X-ray studies of the Moon

by

Shyama Narendranath.K.C
ISRO Satellite Centre, Bangalore

A thesis submitted in partial fulfillment for the award of degree of Doctor of Philosophy to the

Department of Physics
University of Calicut
Calicut, Kerala

May 2010

Certificate

This is to certify that the thesis titled '**X-ray studies of the Moon**' is a bonafide record of the work done by Shyama Narendranath. K. C under our joint supervision and that no part of it has been included any where previously for the award of any degree, either in this university or any other institution.

Dr. P. Sreekumar
Group Director, SAG
ISRO Satellite Centre
Bangalore

Dr. B.R.S Babu
Professor, Department of Physics
University of Calicut
Kerala

May 2010

Declaration of Authorship

I hereby declare that the thesis titled **'X-ray studies of the Moon'** is an authentic record of the research work carried out by me under the supervision of Dr. P. Sreekumar, ISRO Satellite Centre and Prof. B. R. S. Babu, Department of Physics, University of Calicut. No part of this work has formed the basis for award of any other degree or diploma in any university or institution.

Shyama Narendranath. K. C

May 2010

Thus evolved the Original Moon
in those turbulent times
Now we paint from fragments of clues
the reasons and the rhymes

Carle. M. Pieters

Abstract

X-ray remote sensing is an established technique for chemical mapping of atmosphere-less inner solar system bodies. Chandrayaan-1 X-ray Spectrometer (C1XS), on-board the first Indian lunar mission Chandrayaan-1, was flown with the objective of globally mapping the abundances of the major rock-forming elements Mg, Al, Si, Ca ,Ti and Fe with a spatial resolution of 25 km on the lunar surface. C1XS employed **'swept charge devices'**, a recently developed variant of x-ray CCDs as detectors.

In this thesis, we present the calibration of the C1XS experiment, derive the detailed instrument response, analyze lunar x-ray fluorescence data and derive elemental abundance of the major elements Mg, Al, Si, Ca and Fe from a region in the central nearside highlands of the Moon. This work is the first ever estimation of absolute x-ray line flux from the lunar surface. Ca abundance from a highland region has also been directly estimated for the first time through remote sensing.

The first chapter gives an introduction to lunar chemistry. The principles involved in the elemental analysis using the technique of x-ray fluorescence are described. This chapter also gives a brief account of x-ray remote sensing of the Moon and the results from earlier experiments. Further we briefly compare XRF with other remote sensing techniques for compositional studies and highlight the potentials of this technique.

The second chapter describes the C1XS experiment. We describe the swept charge device (SCD) used in C1XS instrument and the observation scenario in detail. This chapter is meant to serve as a background on C1XS in order to appreciate better, the work presented in the next three chapters.

We describe the detailed ground calibration of C1XS detectors in the third chapter and present results from the analysis of the calibration data. The spectral redistribution function (SRF) of a SCD is complex with a significant contribution from events split between

adjacent pixels. We model the spectral redistribution function of the SCDs. With respect to a reference detector calibrated at the electron storage ring at PTB/BESSY II, we determine the detection efficiency of the SCDs. Further, a non-Gaussian response matrix is constructed using the SRF in XSPEC (x-ray spectral analysis package)- compatible format for use during lunar x-ray spectral analysis.

In the fourth chapter, the analysis of lunar x-ray fluorescence spectra obtained during a bright flare which enabled measurements at 50 km spatial resolution, is presented. The background in the detectors is studied prior to this. It is found that the background spectrum in the detectors is very steady except during geotail passes. As the Moon passes through the particle rich region in the plasma sheet of the extended geotail, the background spectrum in the detectors is enhanced and become harder. Particles also induce characteristic x-rays from the Al filter on C1XS which could contribute to the Al fluorescence from the lunar surface.

We derive the elemental abundance for the sampled 50 x 250 km stretch on the southern nearside highlands of the Moon. Several minor elements are also detected in the spectrum which are weak and hence could not be quantified.

In the last chapter we discuss the chemistry of the region sampled by C1XS in its geological context. C1XS derived compositions are distinct from that of the returned lunar samples and the feldspathic lunar meteorites. We discuss the possible scenarios under which this could happen. Considering the need to determine global geochemistry which C1XS could not achieve, we propose a larger area x-ray fluorescence experiment for a future lunar experiment.

Acknowledgements

Five years before, I was never particularly fascinated by the Moon, I have never wondered where it came from or spent many nights just breathing in the beauty of the secrets that lie hidden deep behind its overwhelming charm..but I do now. Solely because of this wonderful experience of working for an instrument which is at the moment around the Moon on Chandrayaan-1. And I owe every bit of that to my guide P Sreekumar and a mere thank you note cannot repay his constant mentoring and encouragement. I also thank Prof. BRS Babu at the University of Calicut for providing important suggestions for my thesis.

Dr. Seetha has been a true inspiration and I thank her for her guidance during my initial days as a student. VC Babu, BN Ashoka and MR Sharma has helped me learn the basics of testing an instrument and I am immensely thankful to them for that.

I have to specially mention Vaishali for helping me out with IDL programming which made the analysis done in this work much easier. Again, PS Athiray (ISAC) has been very supportive and I have used some of his results in this work. I also thank Radhakrishna, Girish, Sankar and Debbijoy, for useful discussions and guidance.

Thanks to my colleagues Sreejith, Ravi, Manju, Ramadevi, Uma Unnikrishnan, Lalita S, Lalita Abraham, Anurag, Smrithi, Monoj and the entire team of people at the Space Astronomy Group, ISRO Satellite Centre for the lively environment. A special thanks to Padmavathy for her support and patient listening at times of despair.

I owe a great deal to Chris Howe (RAL) , the Chief Engineer who made C1XS possible. He has immensely helped me in understanding C1XS instrument, its operations and trained me in routine management while in orbit. I have to also thank him and his wife Julie for making my stay in UK memorable and for all the exotic dishes they prepared. I also thank Barry Kellett (RAL) for useful discussions and analysis help, M. Wallner (RAL) for training me to work with 'nuts and bolts' at RESIK, Brian Maddison (RAL) for financial support while at RAL as well as his cheerful company, Brian Stewart for C1XS quick look software and Barry Kent (RAL). Overall my experience at the Rutherford Appleton Laboratory, UK has been very rewarding and for this I have to thank Christian Erd at ESA who more than once organised financial support for my travels and his guidance during C1XS calibration.

I would also like to specially mention K. Thyagarajan (ISRO) whose efforts were vital for facilitating my UK visits for C1XS calibration. I am very thankful to Jyoti Soman, Sura, Dinakar, Bhaskar, Anshuman, Bharati, Sreekantha and many other colleagues in ISAC from whom I have learned many aspects of spacecraft integration, checkout and operations.

I am very thankful to Alok Srivastava and also to Neeraj Satya, Thermal Group, ISAC for enlightening me on the thermal design aspects. Alok has also been a great support during many difficult times.

I thank DA Daniel (ISAC) for the excellent application he developed for displaying C1XS results on base maps and Uma devi (ISAC) for relevant information on the mission. I also thank Gomathi. S (ISAC) for support during C1XS operations.

Again I am very thankful to Katie Joy at LPI for introducing me to the beautiful world of geology. She has always been very helpful in finding useful literature. I thank Jason Gow and David at Brunel. Jason's notes on SCDs, helped me understand C1XS detectors.

I also thank I. Crawford (Birbeck School of Earth Sciences, UK), O. Gasnault (CSER), S. Maurice (CSER), L. Nittler (CWI) for discussions.

I have to specially mention Keith Arnaud at GSFC for taking time to often answer queries on XSPEC, of a student he has never met. Likewise, I thank Kazunoiri Ogawa at ISAS, JAXA for making me aware of many Japanese references relevant to my work and information on Selene-XRS. I thank PE Clarke (NASA) who took the trouble to scan the typewritten copy of her thesis done in 1979 and sent it to me.

I gratefully remember the discussions with Prof. P. C. Agrawal (TIFR), Prof. Upendra Desai (GSFC), Parthasarathy (NGRI), Prof. Goswami (PRL), Prof. Murthy (PRL), V. Kashyap, K. Tolbert (GSFC). Though not explicitly mentioned, there are numerous people from whom I have learned valuable lessons in the last many years.

Though not involved with my thesis, I would like to gratefully remember Prof. T. N. Vasudevan and . Prof. Vishnu Mayya Bannur and all my teachers at the University of Calicut Physics department because of whom I grew an interest in physics. Special mention again to BRS Babu for his encouragement from my MSc days. He has also gone out of the way to help me even with administrative formalities associated with this thesis.

And finally let me thank my own family: my husband for his encouragement to take this up, my father for sacrificing his career for mine, my daughter whose smiles and woes helped me through most difficult times and above all, my mother without whom I wouldn't have seen the world in this light.....

Contents

List of Figures

List of Tables

Abbreviations

ADC	**A**nalogue to **D**igital **C**onverter
CCD	**C**harge **C**oupled **D**evice
C1XS	**C**handrayaan-1 **X**-ray **S**pectrometer
CXB	**C**osmic **X**-ray **B**ackground
ESA	**E**uropean **S**pace **A**gency
FAS	**F**erroan **A**northositic **S**uite
FHT	**F**eldspathic **H**ighland **T**errane
FOV	**F**ield **O**f **V**iew
FWHM	**F**ull **W**idth at **H**alf **M**aximum
GEANT	**G**eometry and **T**racking
ISRO	**I**ndian **S**pace **R**esearch **O**rganisation
KREEP	**K**Pottasium **REE**Rare Earth Elements **P**hosphorous
LMO	**L**unar **M**agma **O**cean
LP	**L**unar **P**rospector
LRO	**L**unar **R**econnaissance **O**rbiter
PIXE	**P**article **I**nduced **X**-ray **F**luorescence
PKT	**P**rocellarum **K**reep **T**errane
SCD	**S**wept **C**harge **D**evice
SRF	**S**pectral **R**edistribution **F**unction
SPA	**S**outh **P**ole **A**itken
XRF	**X** **R**ay **F**luorescence

For all those who dedicated their heart and soul to the success of India's first lunar mission Chandrayaan-1. . .

Chapter 1

Introduction

Moon being the brightest object in the night sky, has been of great interest to many generations. The motion of the Sun and the Moon have been studied from vedic times and the earliest Indian calendar was based on the motion of these celestial bodies (compiled in *vedanga jyotisha* in 1400 BC). Aryabhata in 500 AD calculated the length of a lunar day with a very high precision. Drawings of the features on the lunar surface, date back to the times of Aristotle (384-322 B.C). The invention of the telescope brought about a great advancement in recording detailed features on the lunar surface. Beginning with Galileo, there have been several astronomers who have painfully hand drawn many fine details of the near side of the Moon using a telescope. The first lunar flyby mission by the Soviet Union , Luna 2 in 1959 opened up a new era of exploration from space. Several lunar missions flew from 1959 to 1975 which immensely enhanced our understanding of the Moon. The spacecraft Galileo (in 1990 and 1992 obtained multi spectral images of the lunar surface [Belton et al, 1992] while it encountered the Moon for gravity assist *en route* to Jupiter), Clementine (1994) [Nozette et al, 1994] and Lunar Prospector (1998) [Binder, 1998] with its suite of more advanced instruments provided new insights into the study of the Moon. Recently there has been a revival in lunar science exploration beginning with SMART-1 (2003) [Foing et al, 2001] and taken on by Kaguya (Selene-1, 2007) [Mizutani et al, 2004], Chang'e-1 (2007) [Huixian et al, 2005], Chandrayaan-1 (2008) [Bhandari et al, 2004] and Lunar Reconnaissance Orbiter (LRO) [Keller et al, 2009] were launched with an impressive set of instruments covering a broad spectrum of lunar science interests.

A great leap in lunar science occurred with the manned Apollo expeditions and the robotic Luna missions which together brought back lunar samples from nine locations.

Moon, which was earlier thought to be an undifferentiated primitive object, turned out to be a differentiated body with a crust, mantle and perhaps a small core. The first meteorite to be recognized (based on oxygen isotope ratios) as of lunar origin was Alha 81005 [Marvin, 1983] in 1982 and resulted from the experience gained by lunar sample analysis. Since then there have been more than 60 lunar meteorites collected which adds to the lunar global data base. In spite of real samples, remote sensing experiments to the Moon to understand composition are still important. The original lunar crust formed during differentiation is believed to have had a nearly homogeneous composition laterally. Mare basalts are later intrusions to this crust. Over billions of years, the lunar crust has been re-worked by meteoroid impacts and this has built up a thick layer of unconsolidated rock and soil which we call the 'lunar regolith'. Local variations in the regolith in small scales can arise from materials of extra-lunar origin, rocks excavated from a depth due to impacts, impact generated materials like breccias, agglutinates etc. Global remote sensing measurements are essential to understand compositionally distinct geological units relevant to the broader aspects of the evolution of the Moon.

The Chandrayaan-1 X-ray Spectrometer (C1XS) was flown with the objective of globally mapping the distribution of the major rock-forming elements on the Moon through x-ray remote sensing. This thesis deals with the characterization and calibration of C1XS and reports the first results from the experiment. This chapter is an introduction to lunar chemistry relevant to subsequent discussions. We also describe the method of x-ray remote sensing which forms the basis for C1XS and compare it with other methods of remote sensing for compositional studies.

1.1 The Moon

1.1.1 Origin

The origin of the Moon cannot be just considered as a natural consequence of Earth's formation as for the satellites of the outer planets. When compared to other such systems in the Solar System, the Earth-Moon system is special in many ways. Among the inner rocky planets (Mercury, Venus, Earth and Mars), only Earth has a satellite (Phobos and Deimos which orbit Mars are captured asteroids). The size and angular momentum involved in the Earth-Moon system is significantly larger than other such systems in the Solar System. For example the mass of the Moon is 0.0123 the mass of Earth while

Ganymede is only 0.00008 times that of Jupiter. Similarly the ratio of the radius of the Moon to that of Earth is 0.2728 while that for the Ganymede-Jupiter system is 0.0368, an order of magnitude difference. Angular momentum of the Earth-Moon system is unusually large (3.5×10^{41} g cm^{-2}s^{-1}) by Solar System standards for the corresponding total mass in the system. This points to the fact that the origin of Earth's moon might require an explanation different from the origin of other such systems.

There are four main hypothesis for the origin of the Moon [Wood, 1986]:

1. **Co-accretion:** This hypothesis suggests that the Moon was formed from the disk of orbiting gas and dust around the newly formed Earth, like the satellites of the outer Solar System bodies.

2. **Capture:** Moon was formed elsewhere in the Solar System and was captured when it fell under the gravitational influence of the Earth.

3. **Fission:** Moon is currently receding away from Earth at the rate of 33 mm/ year [Wood, 1986]. This means that the Moon was much closer to Earth (a minimum of $2.9R_E$ for lunar density material [Canup, 2004]) when it formed. If so, in order to conserve angular momentum of the system, Earth would have to be spinning faster. According to the fission hypothesis a young homogeneous Earth was rotating fast (with a period of $\sim$2.6 hours [Binder, 1986]) and as it differentiated, spun faster and expelled a chunk of matter due to rotational instability. This piece of matter consequently could have evolved into the Moon.

4. **Impact hypothesis:** A large object the size of Mars impacted the Earth and expelled a large amount of matter from the crust. This material possibly vaporized, condensed together with the impactor material and formed the Moon.

The impact hypothesis formulated from the ideas of Hartman and Davis [Hartmann and Davis, 1975], was further developed by Cameron and Ward [Cameron and Ward, 1976]. Subsequently there has been continuing efforts which resulted in several detailed models for the impact hypothesis. However, the basic idea is that an impactor of mass $\sim$0.1 Earth mass collided with Earth and ejected enough material which then settled in a stable orbit and subsequently accreted to form the Moon. The two major guiding factors for this model is the angular momentum of the Earth-Moon system (sum of Earth's rotational angular momentum and Moon's spin angular momentum) which can be calculated as 3.5 x 10^{41} g-cm^2/s and the fact that the bulk iron (total iron in the

crust, mantle and core) content of the Moon (13% [Taylor, 1986]) seems to be much lesser than that of Earth (32 % [Taylor, 1986]). The giant impact hypothesis involves material to enter the orbit around the Earth through a variety of mechansims such as impact jets, vapor clouds, gravitational interactions among the debris etc because of which the parameter space to simulate formation of the Moon and the dynamics (see [Canup, 2004] for a review) is quite large. The impact generated kinetic energy can lead to depletion of volatile elements on the Moon.

The Moon that accreted from the impact induced accretion disk around the Earth is believed to have undergone global melting (due to the energy of accretion). This event is referred to as the Lunar Magma Ocean (LMO) phase. Models suggest that the extent of melting would have been anywhere from a depth of 200 km to a completely molten Moon. The lunar crust crystallized from the magma ocean with the Al-rich low density minerals being lighter, forming a global top layer over the underlying more mafic (higher Mg and Fe) materials. The composition of the different layers of the Moon are thus important markers of the thermal history and critical to understand the thermal evolution of the Moon.

1.1.2 Lunar composition

Composition can be expressed in terms of the bulk concentration of elements, the minerals formed from the elements or the rocks which form as the minerals aggregate. A knowledge of all three are required to understand the origin and evolution of the body. Crystalline solids formed as a result of geological processes are called **minerals**. Elements are the building blocks of minerals and mineral aggregates in turn form rocks. The elements that comprise a mineral can be classified into

Major elements which control the basic atomic structure and gross properties. O, Na, Mg, Al, Si, Ca, Ti and Fe are the major elements in the terrestrial planets.

Minor elements which occur in less than 1% in weight in the sample and affect certain physical properties such as color. eg:- sulphur gives a yellow color to the parent rock. S, Cl, Cr, and Mn are some of the minor elements in the lunar rocks.

Trace elements occur in less than 0.1% in weight. But they represent intrusions into the crystal structure during late stages of crystallization and hence provide insight into the environment in which the crystal formed. eg:- rare earth elements

TABLE 1.1: Major lunar mineral compositions

Major minerals	**Formula**
Plagioclase	$(Ca,Na,K)Al_2Si_2O_8$
anorthite	$CaAl_2Si_2O_8$
albite	$NaAlSi_3O_8$
Pyroxene	
orthopyroxene	$(Mg,Fe)_2Si_2O_6$
clinopyroxene	$(Ca,Mg,Fe)_2Si_2O_6$
Olivine	$(Mg,Fe)_2SiO_4$
fayalite	Fe_2SiO_4
forsterite	Mg_2SiO_4
Ilmenite	$FeTiO_3$

TABLE 1.2: Pristine igneous lunar rocks

Pristine lunar rocks	**Mineral comp**	**Mg#**	**Remarks**
Ferroan Anorthositic Suite (FAS)	$>An_{94}$ +pyroxene +olivine	0.4-0.7	Low trace element content,age: 4.44- 4.54 Ga
Mg-suite	An_{84}-An_{98} +pyroxene +olivine	0.6-0.95	Higher trace element content,age: $>$ 4.5- 4.1 Ga
Alkali suite	An_{63}-An_{94} + clinopyroxene	0.4-0.6	High trace element content,age:4.3- 3.8 Ga
KREEP basalts	Pyroxene +plagioclase	~ 0.5	Higher trace element content,age: 3.82- 3.86 Ga

All the 90 naturally occurring elements can be combined in different ways to form minerals. But the common minerals would be made of the most abundant elements. The minerals which comprise the common lunar rocks are given in Table 1.1. A rock is composed of an assemblage of minerals which can be mechanically separated from it. Rocks form as a part of the primary crust and later get fractured by impacts or stress and get transformed by the environment.

The Moon is a differentiated planetary body (ie having distinct layers of different compositions, indicative of global melting and stratification) with a crust, mantle and a core, each having distinct compositions. Based on the analysis of rocks in the returned lunar samples and lunar meteorites, we believe that the average lunar crust is primarily composed of plagioclase. The original unaltered crustal rocks formed from intrinsic magmatic processes of the Moon (called pristine) are classified into four suites (based on composition) and are listed in Table 1.2.

Ferroan Anorthositic Suite (FAS) rocks comprises of the ferroan anorthosites with $> 90\%$ plagioclase. The high content of a single mineral suggests that they formed by seperation of just formed crystals from a melt. Recent results ([Ohtake et al, 2009], [Pieters et al, 2009]) from Kaguya and Chandrayaan-1 reveal pristine unshocked anorthositic rocks almost entirely composed of plagioclase ($>$ An_{98} where the anorthite (An) content is defined as $\frac{Ca}{Ca+Na+K}$ where the elemental abundance is expressed in wt%) in many areas of the Moon, providing support to the LMO hypothesis. Mg-suite rocks have a higher Mg number (defined as $\frac{Mg}{Mg+Fe}$ and denoted as Mg#) and a wider range of anorthite content (An_{98} to An_{84}) than FAS. They appear to have crystallized from magmas rich in incompatible elements (elements which do not fit into the crystal structure of the major minerals are left behind as the magma cools and minerals crystallize. eg: rare earth elements) and are primitive as rocks in the FAS. Their global distribution is not well known (which can be derived from global maps of Mg# and An content), which would provide insight into their origin and is one of the important open issues regarding crustal composition. Alkali suites are less abundant but are strikingly different because of their higher alkali content (higher sodic plagioclase leading to An content as less as An_{70}) with Na_2O averaging at $\sim$ 1.6 wt percentage. Their distribution and nature of occurrence (whether as large outcrops or separate intrusions) on the lunar surface is also not known. Based on global Fe and Th measurements and comparing these to correlation in lunar samples, the area called Procellarum KREEP Terrane (PKT) in the north- western hemisphere of the Moon is suggested as the possible area where these rocks are confined to.

KREEP (Potassium, rare earth elements) basalts are formed from igneous melts and are enriched in incompatible trace elements. These are again possibly confined to PKT.

Direct compositional information about the mantle can come only from material that has been brought up from the interior due to impacts or volcanism. Mare basalts which fill the large basins are believed to be partial melts of the lunar interior, that migrated up through the lunar crust and erupted on the surface in effusive volcanic styles (small pyroclastic fire fountains and fissure style eruptions). These erupted lavas provide the primary source of information about the compositional nature of the lunar interior. They are more mafic (higher Mg and Fe) than the highland rocks with pyroxene and olivine dominating over plagioclase. A wide variety in composition exist between the mare basaltic rocks collected during the Apollo missions. Titanium is one of the major elements whose concentration vary considerably among the mare basalts and hence they

are classified according to the weight percentage of titanium in them. The lunar mantle likely has a heterogeneous composition given the wide variety in mare basalts. The thickness of the mantle is not known, but seismic measurements suggest a discontinuity in either composition or density at a depth of $\sim$ 500 km [Wieczorek et al, 2006].

The moment of inertia of the Moon (0.3931$\pm$ 0.0002 Kg m^2 [Hartmann and Davis, 1975]) is very close to that of a homogeneous sphere (0.4 Kg m^2) which suggests the absence of a dense core. However there are evidences primarily from seismic measurements [Nakamura, 2005] to believe that Moon might possess a very small ($<$ 460 km) core whose composition is not well constrained.

The lunar surface that we study today by remote sensing has encountered a huge impact flux (of bodies ranging from a few angstrom in size to several km) which has reworked the original upper crust (Figure 1.1). The whole lunar surface (except for some steep crater walls) is thus covered by a layer of broken melted debris called the lunar regolith. The bulk of the regolith consists of less than 1 cm particles [Lucey et al, 2006] and this fraction of the regolith is called lunar soil. Lunar soil consists of mineral fragments, pristine rock fragments, breccia fragments, glasses and agglutinates. Agglutinates result from melting and mixing of lunar regolith during micrometeorite impact. In the mare regions, the thickness of the regolith is believed to be 4-5 m whereas on the highlands it is 10-15 m (the highlands being older surfaces, have accumulated a thicker layer of regolith). The lunar regolith consists of materials from the upper crust sometimes preserved as such or as part of impact melt mixtures (called impact melt breccias) and material added from the impactors. Since there is minimal lateral movement on the lunar surface, the lunar composition in the regolith is believed to be fairly representative of the underlying crust. The extra-lunar material in the regolith can come from two sources: micrometeoroids and impactors. The extra-lunar component in Apollo soils at four sites have been estimated to be less than 2% [McKay et al, 1991]. Chemistry of the lunar surface measured from lunar regolith has to be corrected for this extra-lunar component. Assuming a chondritic composition for the micrometeoroids, soils get enriched in siderophile elements (elements that concentrate in an iron rich liquid) as it gets exposed to micrometeoroid flux. The amount of siderophile elements thus also indicate maturity (the accummulated effects of space weathering which mostly affects the fine portion of the regolith) and thus age of the soil. The correction is done by modelling the composition that would result from mixing of a chondritic meteorite and a lunar crustal material. Any further enhancement in the proportion of siderophile elements are then considered genuiune (and demands an explanation).

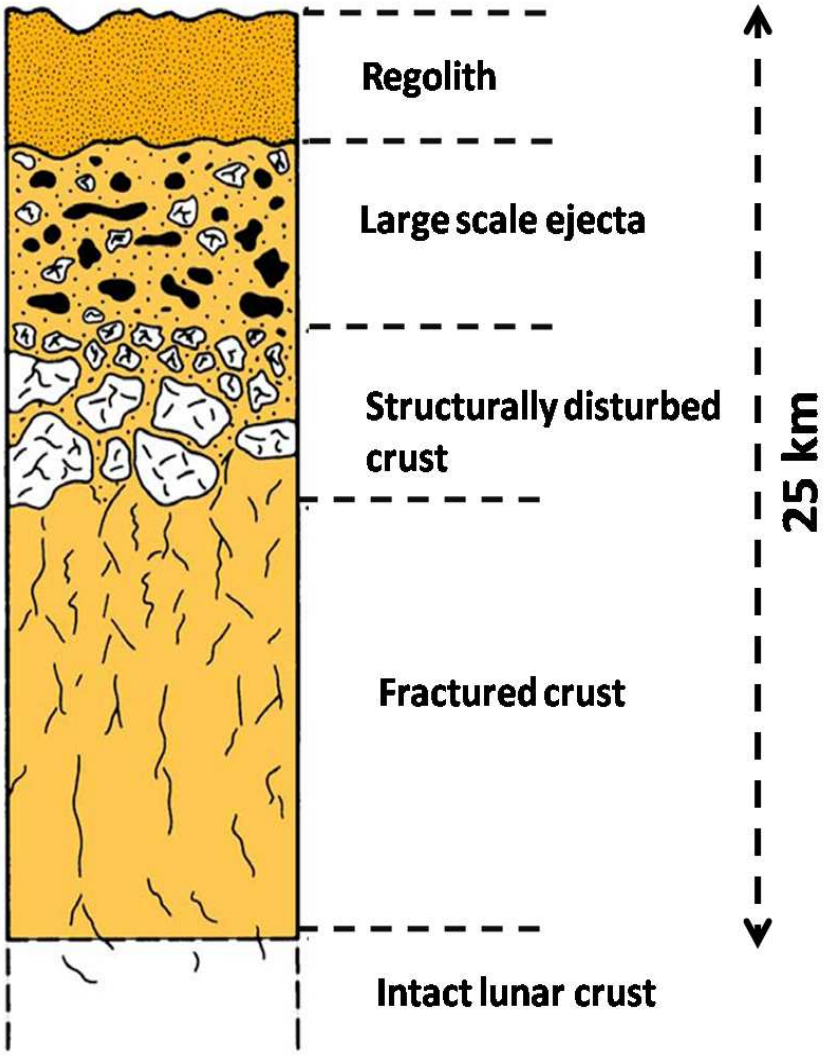

FIGURE 1.1: A schematic diagram showing the cross section of the upper layers of the crust (re-drawn from [Hiesinger and Head, 2006])

Remote sensing measurements from the Lunar Prospector mainly of thorium and iron, identified distinct geochemically different terrains which is broadly classified into three by Joliff et al [Joliff et al, 2000] as the Feldspathic Highland Terrane (FHT), Procellarum KREEP Terrane (PKT) and South Pole Aitken (SPA) region. This together with the difference in crustal thickness in the near side and far side, seems to suggest that the lunar crust possesses a fundamental asymmetry. It remains an open issue whether this asymmetry extends deeper down to the mantle and when and how this happened.

1.2 Remote sensing techniques for lunar chemistry and mineralogy

Composition of a body can be remotely determined with any of the following methods. Here we restrict ourselves to direct measurements. It is to be noted that there are other methods like seismic studies wherein modeling of the composition can be done indirectly by measuring the attenuation of the signals.

1.2.1 Spectral reflectance spectroscopy

Spectral reflectance in the near infra-red (0.7 μm - 3 μm), visible (0.4 μm- 0.7 μm) and ultraviolet (0.001 μm-0.4 μm) wavelengths are useful to determine mineralogy. Radiation measured at these wavelengths from the surface of the planetary body has two components: reflected solar radiation and a re-emitted thermal radiation. Absorption features in the reflected solar radiation is diagnostic of the mineral present. The physics of absorption of solar radiation leading to diagnostics of the mineral, is well summarized by Adler [Adler, 1986].

The most common process that leads to absorption features is the transition between split orbital energy levels of electrons in transition elements (Ni, Cr, Co, Fe etc). The *d* orbital energy state in transition elements split when the ion is located in the field of a crystal. These crystal field transitions of the ferrous iron in pyroxene produces an absorption feature at 1.0 μm which is used as a diagnostic feature. For the same ion, the exact minima of the absorption feature varies indicating compositional differences. For example, ferrous (Fe^{2+}) ion in a mixture of forsterite (Mg_2SiO_4) and fayalite (Fe_2SiO_4) which are both olivines, generates the absorption feature at 1.05 μm when fayalite composition is low and moves to 1.08 μm when fayalite dominates. Though subtle, these variations can in principle provide mineral chemistry as well.

Reflectance spectra are obtained by measuring the reflected light in different wavelength bands or in other words sampling the spectrum at specific bands. Clementine near infrared spectrometer had five bands for sampling [McEwen and Robinson, 1997] while the Chandrayaan-1 Hyper spectral imager had 64 bands [Kirankumar andd Choudhary, 2005]. The choice of spectral range and number and location of sampling bands need to be optimized to ensure that critical diagnostic features are not missed (Figure 1.2).

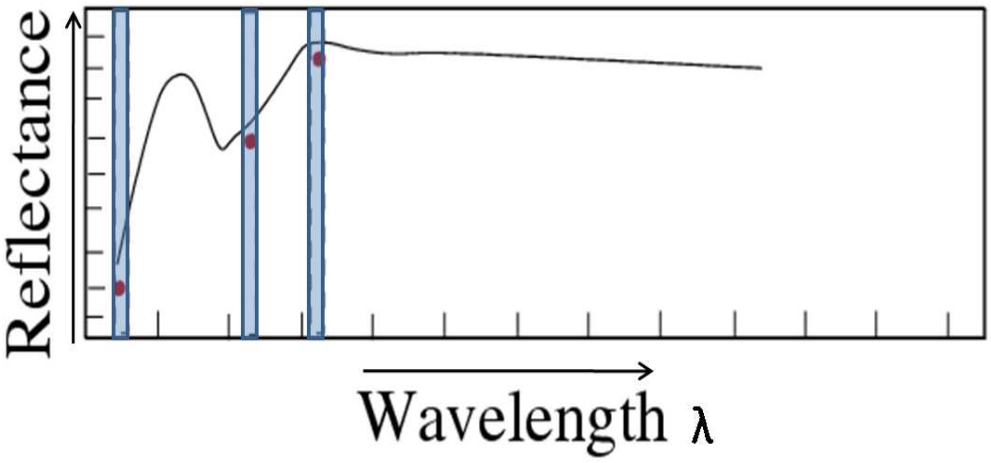

FIGURE 1.2: Schematic reflectance (arbitrary units) spectrum with an absorption feature. Colored bands are the wavelengths being sampled, the sparse sampling of which may lead to loss of critical information.

Absorption bands also arise when an electron moves from one ion to another within the crystal on absorption of a photon. These are called charge transfer absorptions and these strong absorption bands appear at ultraviolet wavelengths. For example iron oxides like hematite and limonite are readily identified on martian surface due to the intense charge transfer band in ultraviolet. In minerals like cinnabar (HgS) with a band gap equal to the photon energy, transitions from conduction to the valence band occur and result in absorption in the visible wavelength range. Minerals can also be identified by their color in visible. Some minerals have color due to absorption by defects in the crystal called color centers. The defects create discrete energy levels between which there could be electronic transitions leading to absorption of photons in the visible thus yielding colors to the crystal (eg:- yellow color in fluorite).

Transitions between different vibrational levels of any asymmetric molecule (like one with an O-H bond) also create absorption bands in the near infrared. For example liquid water has absorption features at 3.106 μm (fundamental), 6.079 μm and 2.903 μm (harmonics) forming a good diagnostic for water bearing minerals.

An emissivity maximum (reflectance minimum) between 7 and 9.5 μm called Christiansen Feature (CF) which occurs because of the change in the real part of the refractive index of the mineral is a good diagnostic for silicate minerals. The CF occurs on the short wavelength side of the fundamental absorption band and shifts to shorter wavelengths as polymerization of SiO_4 tetrahedra increases [Taylor, 1997].

In summary, reflectance spectroscopy is a very useful technique to study the mineralogy of planetary bodies remotely. The solar intensity which is the source of illumination for remotely sensing reflectance spectra, almost remains constant (< 0.1 % variation across the solar cycle). Hence the strength of absorption lines are indicative of the strength of the mineral present from which absolute mineral abundance can be derived. However there are several factors which complicate the application of reflectance spectroscopy to identify and derive abundance of minerals remotely.

- Identification of the mineral is often done based on absorption features. However, the absorption minima is sensitive to subtle changes to the crystal structure. Also there are a number of transitions (as discussed above) to which the spectra is sensitive to and hence unique identification sometimes is challenging.
- The reflectance spectra consists of a continuum with absorption features. The depth of absorption, apart from the abundance of the absorbing material, is also dependent on the grain size (the dependence is non linear).
- Mineral grains in a rock occur as mixtures and may have different optical properties. Therefore the reflectance spectra from a mineral mixture is different from that in a pure mineral. Even 1-5 % of any opaque mineral (which absorbs the radiation completely), can drastically reduce the strength of absorption features and its albedo. Such effects can also be caused by shocks.

Lunar mineralogy has been largely derived from spectral reflectance measurements in the near infrared (0.4 - 3 μm) band. The characteristic 1 μm absorption feature of Fe^{2+} in the iron bearing silicate minerals makes the identification of pyroxene and olivine unambiguous. Fe and Ti (using band ratios in UV and visible) have been globally mapped by Clementine using multi-spectral measurements. The detection of pure anorthosite rocks (unshocked) with greater than 98% plagioclase has been reported by the multiband imager on Kaguya [Ohtake et al, 2009] strengthening the case for the LMO. Moon mineralogy mapper (M3) on Chandrayaan-1 detected absorption features on the surface of the Moon in the 2.8 to 3.0 μm range which can be attributed to OH^- and/or H_2O bearing materials [Pieters et al, 2009]. This was further confirmed by reanalysis of the infra-red spectrometer data measured during a flyby of Cassini deep space mission in 1999 [Clark, 2009]. These new wealth of data from Kaguya and Chandrayaan-1 has opened several new questions on the composition of the lunar surface.

1.2.2 Gamma rays

Gamma rays are produced from the lunar surface by the following processes

- Potassium, thorium and uranium emit gamma rays as they decay due to their natural radioactivity. They are all incompatible elements and hence their presence indicates for example, regions containing late stage melt residues.
- Galactic cosmic rays cause nuclear spallation reactions which generate gamma rays either through inelastic scattering or neutron capture. Gamma ray lines are emitted from oxygen, magnesium, aluminum , silicon, calcium, titanium and iron through these reactions. Derivation of absolute abundances in this case requires knowledge of the neutron flux that caused these reactions.

The gamma ray intensity is proportional to elemental abundance. Global maps of absolute abundance of thorium, iron and titanium as well as a first order map for other major elements have been generated using the Lunar Prospector gamma ray spectrometer [Prettyman et al, 2006]. The factors which affect conversion of gamma ray line flux to elemental abundance are follows.

- Gamma ray production from the radioactive elements are not affected by any other factors and hence it is straightforward to derive elemental abundance of Th, U and K. Thorium line at 2.61 MeV is the second strongest (first being K at 1.45 MeV) as well as it is well separated from other lines. Gamma ray flux is proportional to the incident flux of particles which cause the nuclear reactions. Galactic cosmic ray spectrum is well known, but the interaction of cosmic ray protons with the nuclei on the lunar surface has to be modeled accurately to determine the number of neutrons thus generated which can cause reactions which produce gamma rays. The flux of neutrons emitted from the lunar surface is essential to model this. The Lunar Prospector carried a gamma ray spectrometer along with a neutron detector which allowed neutron corrections to be done.
- Gamma ray spectrometers often have a coarse spectral resolution and given the very closely spaced lines of the major elements, it becomes very difficult to separate them. Only thorium and iron lines are well resolved in the Lunar Prospector gamma ray spectrometer.

- In addition to these lines, there is a Compton continuum in the spectra which is quite significant and accurate modeling (of the processes as well as detector response) is essential to determine line flux.

- Gamma ray spectroscopy has been done at coarse spatial resolutions in the past (order of 150 km from a 100 km altitude orbit). Higher spatial resolutions demand heavier systems (for example, collimator which define the field of view have to be thick enough to block these high energy gamma rays) and more resources.

- Measured gamma ray flux from the lunar surface is dependent on the angle at which it is emitted from the surface.

- Solar wind implanted hydrogen in the regolith causes an increase in thermal neutron capture. This in turn increases the gamma ray flux. Therefore ideally the hydrogen content of the lunar soil is required for modeling the interactions. However the amount of hydrogen at the equator and mid latitudes is very small and it has been shown by Prettyman [Prettyman et al, 2006] that this affects the modeled flux only up to 0.6%. But at higher lalitudes the elemental abundance may be affected by the higher hydrogen content.

In spite of the above mentioned complexities, gamma ray spectroscopy is the only tool which can map the abundance of radioactive elements from orbit (the Lunar Prospector gamma ray spectrometer mapped thorium and iron at a spatial resolution of 150 km and generated global maps). Maps of the other major elements (O, Mg, Al, Si, Ca, Ti) were derived indirectly based on the known correlations or anti-correlations between them, derived from lunar sample compositions [Prettyman et al, 2006]. The Kaguya gamma ray spectrometer has generated global maps for thorium, uranium and potassium [Kobayashi, 2010] at a spatial resolution of 200 km.

1.2.3 X-ray Fluorescence

A few decades after the discovery of x-rays by Wilhelm Rontgen, it was shown by Moseley in 1913 that when pure substances are irradiated with a beam of x-rays from an x-ray tube, they produce new x-ray photons with an energy, characteristic of the substance.

An x-ray photon can interact with a bound electron in an atom in any of the following ways.

- Photoelectric interaction: If an x-ray photon strikes a bound electron with an energy greater than the binding energy of the electron, the energy of the photon can be completely transferred to the electron. The electron is then ejected from the atom with a kinetic energy, $E_{K.E}$ given by

  $$E_{K.E} = E_{photon} - E_{B.E}$$

  The atom is now in an excited state because of the vacancy left by the electron. It returns to the ground state as an electron from a higher shell fills in the vacancy. In this process, the energy difference between the two atomic shells is carried away by a photon. This process is called x-ray fluorescence (XRF). This creates a vacancy in the higher shell which is filled by an electron in a still higher shell and this is thus a cascading process. Since the energy difference between levels is unique to the atom which emits the photon, the energy of the x-ray photon identifies the atom which emitted it.

- Coherent scattering: When an x-ray photon gets scattered from the atom without transferring any amount of energy to the atom, it is called coherent scattering. The energy of the scattered x-ray photon is same as that of the incident photon while there is a change in direction.

- Incoherent scattering: When the x-ray photon gets scattered from the atom and transfers a part of its energy to the atom, it is called incoherent scattering. In this case the energy as well as direction of the incident x-ray photon changes.

All of the above processes occur when a beam of x-ray photons strike a material. The emission of XRF photons with a unique set of energies from a sample helps in determining its composition. This forms the basis for all XRF experiments. Solar x-rays form the source of excitation for x-ray fluorescence from the lunar surface. But unlike in visible and infra-red, solar x-rays are highly variable during the 11-year solar cycle. So, in addition to the actual elemental abundances, the observed x-ray line fluxes from a planetary body are also dependent on

- the incident solar spectrum : The solar x-ray emission is highly variable over periods as short as a few seconds. Hence it is important to simultaneously measure the solar spectrum down to 1 keV.

- inter-element effects : The observed x-ray fluorescent line intensity from a sample depends on the mass fraction of other elements in the sample. The effect could

be studied and an empirical relation derived to relate the line intensity and the concentration of a particular element in a given sample as has been done for alloys [Rasberry and Heinrich, 1974]. The treatment of this effect for laboratory analysis is described in Jenkins [Jenkins, 2000].

- particle size : In regions where the mean particle size is larger than the penetration depth of x-rays (which is the case of lunar regolith), particle size affects the x-ray fluorescent line intensity. Laboratory experiments have shown that the x-ray fluorescent line intensity for a given element decreases with increasing particle size [Maruyama et al, 2007].
- incidence angle : The angle made by the solar x-rays with the planetary body's surface keeps changing as the Moon moves in its orbit around the Sun.
- phase angle : The angle between the source (Sun), planetary body and the detector changes as the spacecraft moves in the lunar orbit.

The above factors are not mutually independent. The changes in line intensity arising from variations in angle of incidence and phase angle are different for terrains with different mean particle sizes. The XRF line intensity decreases with increase in grain size and the decrease is larger at larger angles of incidence. For example, in [Maruyama et al, 2007] it is shown that the XRF line intensity (relative to a flat sample) from a powdered sample of olivine basalt decreases from 85% to 75% as the particle size increases from 40 μm to 220 μm at an angle of incidence of 35° while the decrease is from 75% to 50% as the angle of incidence increases to 65°. Such effects can be analytically modelled as has been shown in [Finkelshtein et al, 2009] where grain size effects in binary mixtures are modelled and compared with experimental data.

1.3 What does elemental abundance tell us?

Early Solar System formation models suggest that a protosun with a disk of gas and dust formed from a molecular cloud due to gravitational collapse. Strong stellar winds and radiation during the T Tauri phase could have blown away much of the dust from the inner Solar System. As the matter in the disk, cooled, the first grains to condense would be that of elements with high melting points (called refractory elements), such as Al, Ca and Ti. Chemical thermodynamics would lead the condensation sequence thereon resulting in the formation of mineral phases. But the elemental budget from which

the Solar System evolved would nearly remain constant. Chemical composition of the bodies in the Solar System compared to solar coronal abundance thus provide evidences for the formation and evolution of our Solar System.

We will briefly bring out specific problems that can be tackled by determining the elemental composition of a Solar System body, taking the example of Moon.

Origin of the Moon: Moon and Earth have oxygen isotopic ratio very similar, suggesting origin from a common source. Out of the many models described earlier, impact fission hypothesis rules because of the strong geochemical evidences. Bulk moon compositions play an important role in constraining theories of lunar origin. Global mapping of major elements provide global averages for mare and highlands- the two major geological terranes on the lunar surface. The mare regions are derived from the magmas of the lunar mantle, from a depth of 200-500 km and hence representative of lunar mantle composition. From models of the thickness and density of the crust and mantle, bulk lunar composition can be calculated from the global averages. For example, a global highland average of 25% for Al_2O_3 contributes 3 % to the bulk lunar composition compared to the value of 3.6% in the case of Earth.

Lunar differentiation: Rarer pristine lunar rocks such as Mg-suite are identified on the basis of their relative proportion of Mg and Fe. This requires elemental data rather than mineralogy. The distribution of Mg-suite rocks is not known and is very important to understand the composition and evolution of the early lunar crust.

Changes in solar wind composition: The lunar surface is exposed to the interplanetary plasma, solar wind and Galactic cosmic rays because the atmospheric envelope around the Moon is very tenuous ($\sim 10^7$ particles/cm^3 [Lucey et al, 2006] while the air at sea level on Earth has $\sim 10^{19}$ particles/cm^3). The lunar surface layer has accumulated products from interaction with these components over billions of years which has great scientific value. For example, a record of solar wind implanted noble gas isotopes in the lunar surface has shown that noble gas isotopes from the Sun has not changed very much during the last 4 giga years while nitrogen (taking relative ratios of isotopes) similarly implanted has varied by 30% (the source of this variation is not known) [Lucey et al, 2006]

TABLE 1.3: A comparison of three remote sensing techniques for composition

Method	**Depth of sampling**	**Measures**	**Absolute abund**	**Spatial res. achieved**	**Source**
Reflectance in IR	A few cm	major minerals ($>$ 5% abund)	very difficult	meters	Good solar illumination
X-ray	$<$ 100 μm (Mg-Fe)	major elements ($>$ 1% abund)	yes	20-100 km	Good solar activity
γ ray	$<$ 1 m	major elements and K, Th, U	yes	80-150 km	GCR induced (always present)

1.4 Comparative summary

Spectral reflectance measures minerals whereas the other two methods measure the elements directly. Both these are necessary in order to decipher the origin and evolution of a body. Finding the exact mineral naturally tells us the exact elements present in it. For example, finding forsterite is equivalent to finding magnesium , silicon and oxygen with the proportion 2:1:4. But pure minerals are rare and rocks almost always occur as a mixture of minerals. Exact mineral identification thus is very difficult with any of the methods described alone. But each of these methods (table 1.3) have some strengths over the other and provide supporting evidences essential to derive lunar compositional distribution.

Pyroxene and olivine are readily identified from spectral reflectance measurements because of the diagnostic absorption features (at 1 μm for the iron in pyroxene) but quantitative estimates again require accurate methods of analysis. Often, mineral identification itself is based on forward folding with spectral libraries generated using laboratory spectra. But variations from laboratory conditions result in multiple solutions for identification of less abundant minerals. Elemental abundance through gamma ray measurements are more limited due to technological challenges than analysis techniques. High spectral and spatial resolution experiments in gamma rays are very difficult to realize because of the large mass involved which in turn demand cooling power for spectroscopy. Gamma ray spectra contain scattered continuum and closely spaced lines (many arising from particle interactions in the detector and spacecraft material) which then demands a high sensitivity experiment to map all the major elements. However for the incompatible trace elements such as thorium and uranium this is the only way of estimating abundances.

X-ray fluorescence experiments with moderate resolution and sensitivity can be used to obtain a good estimate of elemental abundances. X-ray fluorescence line energies of the major elements are well separated and can be analyzed with a medium energy resolution detector. Conversion of x-ray line flux to absolute elemental abundances requires corrections to its dependency on solar x-ray spectra, particle size, illumination conditions and its behavior in mixtures. Though past missions have not achieved an independent derivation of elemental abundances, it is possible to do so as will be shown in chapter 4.

Very clearly, elemental mapping and mineral mapping complement each other and are absolutely necessary to understand the origin and evolution of a planetary body. All three methods discussed above are sensitive to techniques employed in deriving elemental abundance and mostly rely on normalizations with the ground truths from samples returned. It is to be noted that this may not always be totally reliable given the different compositions found in the lunar meteorites (which in principle should be representative of the lunar surface without any bias towards specific sampling regions).

X-ray fluorescence measurements offer a direct way to measure x-ray line flux from the major elements thus mapping their distribution. Unlike nuclear spallation reactions in gamma rays, the process is simpler to model as there is only the basic process of XRF which generates the lines and the source is the Sun. Simultaneous measurement of solar x-rays is absolutely essential for converting x-ray line flux to elemental abundance. Though particles do induce characteristic x-rays from atoms through a similar process, the x-ray emission from planetary surfaces are dominated by XRF induced by solar x-rays.

1.5 XRF experiments in the past

On airless planetary bodies, solar x-rays excite x-ray fluorescent photons from the upper layer of the regolith. Assuming a density of $\sim$ 1.9 g cm^{-3} for the lunar regolith [Lindsay, 1976] with composition of pure plagioclase, elemental mapping of Mg, Al and Si is from the very upper 10-15 μm of the lunar regolith. This can be measured remotely by an instrument in an orbiting spacecraft. Luna 12 [Mandel'shtam et al, 1968] spacecraft was the first to carry x-ray detectors to measure lunar surface x-rays. The data obtained were minimal, but there was confirmation that Sun produces measurable lunar x-ray fluorescence. It was the Apollo 15 and 16 x-ray spectrometers [Adler et al, 1973] which

demonstrated the usefulness of x-ray remote sensing for elemental mapping. Figure 1.3 shows all the x-ray experiments that has been flown till 2009 for elemental mapping of planetary bodies. In this section we restrict ourselves to lunar experiments which have published results.

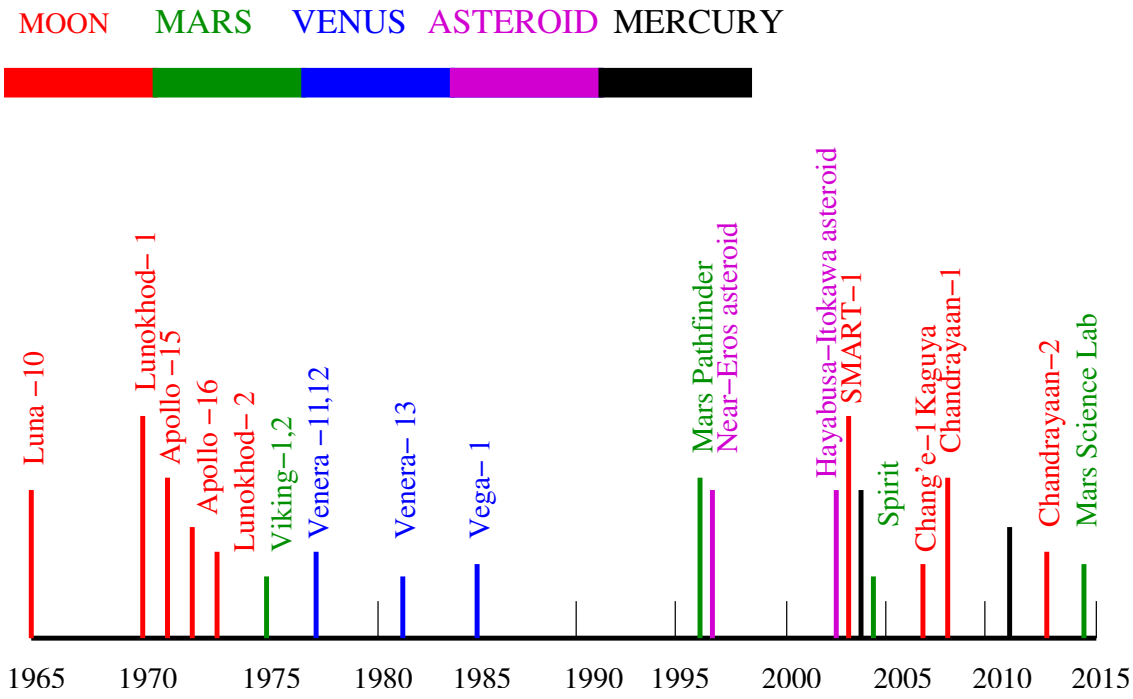

FIGURE 1.3: History of XRF experiments for Solar System bodies.

1.5.1 Apollo 15 and 16 X-ray spectrometers

X-ray fluorescence experiments were flown in the service command module of Apollo 15 and 16 lunar missions. The instrumentation consisted of three proportional counters of $\sim$ 25 cm^2 each with a 25 μm thick Be window, operating in the energy range of 0.75 to 2.75 keV. Proportional counters do not have the required energy resolution to separate the closely spaced x-ray fluorescence lines of Mg, Al and Si. In order to separately measure the three elements, Mg (5 μm) and Al (12.7 μm) filters were respectively employed in two of the proportional counters. The Mg filter mounted detector would allow only Mg to come through and Al filter mounted detector, only Al. The third detector without any filter measured x-ray photons from all three elements. Thus the differential counts in the three detectors enabled separation of x-ray photons at the three energies. The field of view of 30° Full Width at Half Maximum (FWHM) translated to a ground pixel of 100 km at an altitude of 110 km above the lunar surface.

The two experiments together yielded x-ray fluorescence from Mg, Al and Si for about 10% of the nearside equatorial lunar surface. The limited (four orbits of Apollo 15) low altitude (20 km) data enabled spatial scales of 20 x 32 km to be measured as well. The Al/Si and Mg/Si concentration ratios showed that the mare and highland regions were compositionally distinct. Al and Mg showed an inverse relationship to each other. None of the higher elements could be measured (there was a mode of operation which allowed the detector gain to change and increase the operating range to 5.5 keV). The Al/Si ratio also showed a strong correlation with optical albedo. Various studies perfomed with data from these experiments show the usefulness in geochemically characterising smaller lunar features ([Maxwell et al, 1977],[Clark and Hawke, 1977]).

1.5.2 SMART-1 D-CIXS

After Apollo, it was only in 2003 that an x-ray fluorescence experiment was flown on board a lunar mission. D-CIXS on the European lunar mission, SMART-1 had the then current innovative x-ray detectors called swept charge devices (SCDs). Though the detectors intrinsically had good spectral resolution, radiation damage during the 14 months journey of SMART-1 to Moon, combined with the highly elliptical orbit of SMART-1 resulted in limited ability to map the Moon. However, D-CIXS detected XRF from Ca (in addition to Mg, Al and Si), Ti and Fe [Grande et al, 2007], [Swinyard et al, 2009] for the first time during a period of intense solar activity.

1.5.3 Kaguya X-ray Spectrometer

A 100 cm^2 array of x-ray CCDs comprised the x-ray fluorescence experiment on the Japanese lunar mission Kaguya [Okada et al, 2008]. A calibration plate of a known sample was also carried along. Radiation damage to the x-ray CCDs resulted in very limited useful data.

1.5.4 ROSAT and CHANDRA observations

Apart from the dedicated lunar x-ray experiments in the earlier section, there were full disk observations of the Moon with astronomical x-ray observatories Rontgen Satellite (ROSAT) [Schmitt et al, 1991] and CHANDRA [Wargelin et al, 2004]. ROSAT obtained

the first soft x-ray image (0.1-2 keV) of the Moon. CHANDRA obtained an average spectrum of the sunlit side of the Moon and detected K shell XRF of O, Mg, Al and Si. Measurements with well calibrated x-ray instruments as in CHANDRA, though coarser would be useful for additional confidence on abundance derived from the XRF experiments in the lunar orbit.

1.6 Summary

XRF is a unique technique which provides a direct estimation of the major elemental abundance. Apollo 15 and 16 have been the only experiments to successfully derive abundance of Mg, Al and Si, though for only $\sim 10\%$ of the Moon. There is a need for an XRF experiment to globally map all the major elements Mg, Al, Si, Ca, Ti and Fe.

The Chandrayaan-1 X-ray Spectrometer (C1XS) was flown with this objective and during its 9 months of operation has measured lunar x-ray fluorescence from several solar flares. This thesis presents the calibration of the C1XS XRF experiment which involves detailed modeling of the spectral response of the x-ray detectors, analysis of lunar XRF data for a region on the southern nearside highlands and presents the first scientific results from C1XS. We report the first direct estimation of Ca abundance for a highland region through remote sensing. The chemistry of the region sampled is distinct and indicative of lithologies rarer in the returned lunar samples.

Chapter 2

Chandrayaan-1 X-ray spectrometer (C1XS)

In this chapter, we describe the x-ray fluorescence experiment, Chandrayaan-1 X-ray Spectrometer (C1XS), on-board the first Indian lunar mission Chandrayaan-1. The observational geometry, instrument configuration, working principle of the detectors and operational modes are described in detail in order to provide the required background for the work reported in the next three chapters.

2.1 Chandrayaan-1

Chandrayaan-1 (Figure 2.1) was India's first lunar mission and carried a broad spectrum of science experiments with specific science objectives. Chandrayaan-1 was launched by the PSLV-C11 rocket on 22nd October 2008 from Sriharikota (in the state of Andhra Pradesh, India) into a geostationary transfer orbit (GTO). The orbit was systematically enlarged and took $\sim$16 days to traverse the Earth-Moon distance and to be captured into a lunar orbit. The final orbit of Chandrayaan-1 was a polar circular with an altitude of 100 km above the lunar surface. There were 11 experiments [Goswami and Annadurai, 2009] on-board Chandrayaan-1 and they are listed in Table 2.1.

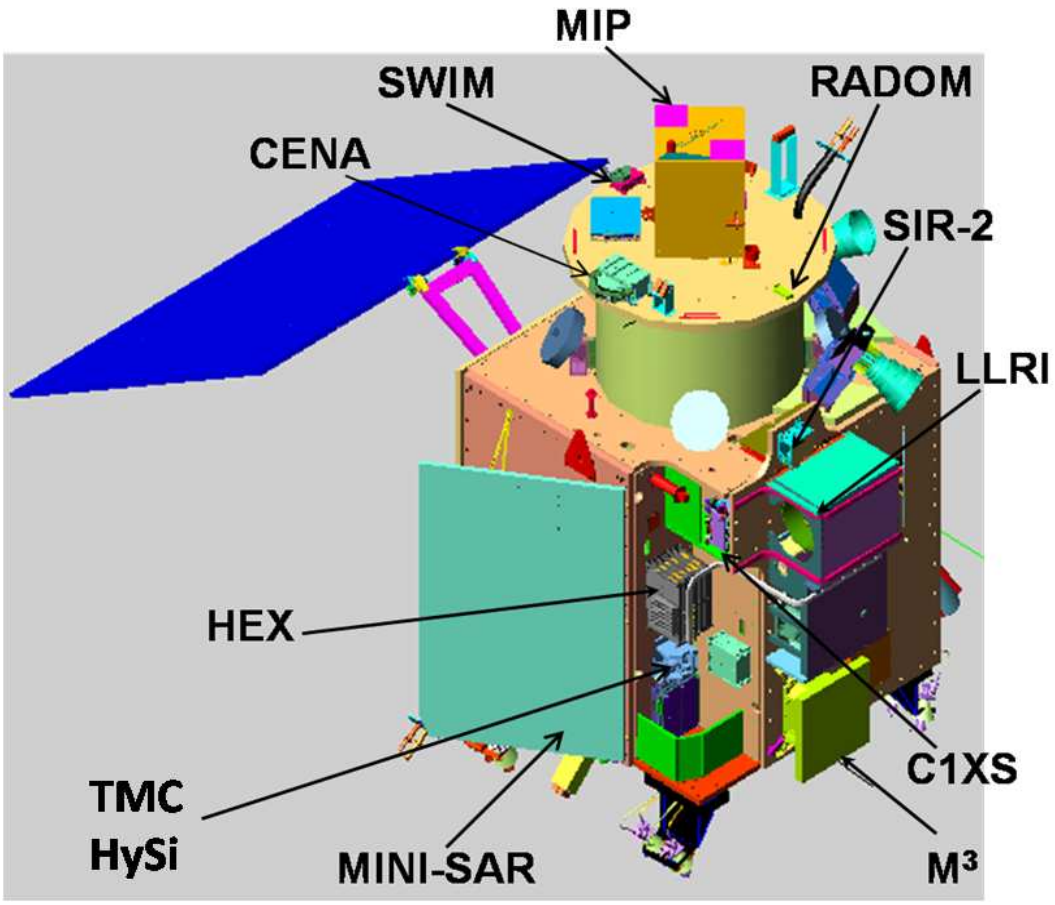

FIGURE 2.1: Chandrayaan-1 spacecraft (CAD model).

2.2 Observational geometry and constraining parameters

The 90° orbital plane of the spacecraft was inertially fixed because of the near sphericity of the Moon. The instruments cover a ground pixel defined by their field of view (FOV) at any instant of time. As the Moon rotates on its own axis, every 27.322 days, the tracks defined by the FOV, consistently shift ($\sim$ 33 km every orbit at the lunar equator), enabling global mapping. There were two phases of observations during the mission life of Chandrayaan-1. During the first phase from November 2008 - April 2009, the spacecraft was at an altitude of 100 km above the lunar surface with an orbital period of 118 minutes. During the second phase from May - August 2009, the spacecraft was moved to a 200 km altitude orbit. This increased the orbital period to $\sim$ 130 minutes. Figure 2.2 shows the measured variation in altitude for two orbits of Chandrayaan-1 during the first phase (100 km altitude). Thus, the instantaneous FOV depends on the altitude of the spacecraft at the given time.

TABLE 2.1: Chandrayaan-1 Instruments

Primary science	**Instrument**	**Energy band**	**Swath (km)**	**Spatial res (m)**
Mineralogy	Hyper Spectral Imager (HySI)	0.4-0.9 μm	20	80
	Moon Mineralogy Mapper(M^3)	0.43-3 μm	40	70
	Infra-red spectrometer(SIR-2)	0.93-2.4 μm	0.2	200
Surface chemistry	Chandrayaan-1 X-ray Spectrometer (C1XS)	1-20 keV	50	2500
	SARA Chandrayaan-1 energetic neutral analyzer	10-3300 eV		
Topography	Terrain Mapping Camera (TMC)	0.5-0.85 μm	20	5
	Lunar Laser Ranging Instrument (LLRI)	1064 nm	0.032	10
Volatile transport	High Energy X-ray Spectrometer (HEX)	30-270 keV	66	3300
Search for water	Mini-Synthetic Aperture M^3	2.38 GHz	8	150
Radiation environment	Radiation Dose Monitor (RADOM)	1-256 MeV		
	SARA- Solar Wind Monitor (SWIM)	0.02-20 MeV		
Lunar atmosphere	Moon Impact probe (MIP)			
	CHACE- Quadruple mass spectrometer	1-100 amu		

Another factor which affects observations is the solar illumination. As the Earth-Moon system moves along the orbit around the Sun at the heliocentric rate of $\sim 1^\circ$/day, the illumination on the lunar surface as seen by the experiments on Chandrayaan-1, varies. This implies that the duty cycle of instruments dependent on solar illumination or the phase of the heliocentric orbit. The temperature experienced on-board also varies during the orbital motion around the Sun. Two extreme situations (each occur twice in a year; Figure 2.3) arise which has an impact on instrument operation:

- **Noon-midnight orbit:** This occurs when the Sun-vector (line directed away from the Sun, joining Sun and orbital plane of the spacecraft) is parallel to the orbital plane of the spacecraft. The angle made by Sun's rays with the lunar surface is 90° at the lunar equator and thus there is maximum illumination. Therefore its an ideal observing condition for instruments dependent on solar illumination. But the temperatures experienced on-board are maximum.

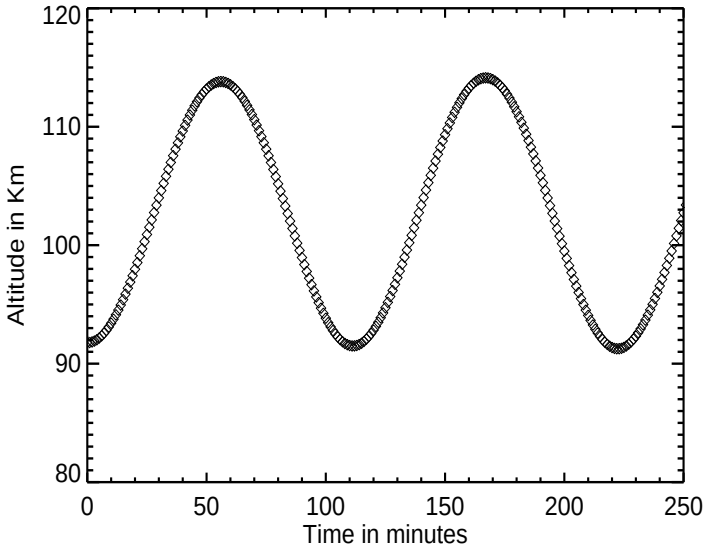

FIGURE 2.2: Chandrayaan-1 altitude variation with time (2 orbits)

- **Dawn-dusk orbit:** This occurs when the vector from the Sun is perpendicular to the orbital plane of the spacecraft. Sun's rays are at grazing incidence along the track of observation and illumination is minimum. Temperatures are also minimum because of this.

The temperature experienced on-board, also varies within an orbit as a function of latitude. The thermal radiation emitted from the Moon (the major component of which is the re-emitted solar radiation) as a function of latitude has been measured using reflectance in the long wavelength (centered at 8.5 μm) range of IR [Lawson and Jakosky, 1999]. This, along with the contribution from direct solar radiation, is used to model the temperatures at different points on the spacecraft. The power dissipated in the instrument then needs to be transferred to a heat sink so as to keep the system at favorable temperatures. The instruments go through temperature cycles as the spacecraft moves around in the lunar orbit and as Moon moves around the Sun. The thermal design of each instrument aims at providing optimal operating temperatures at all times.

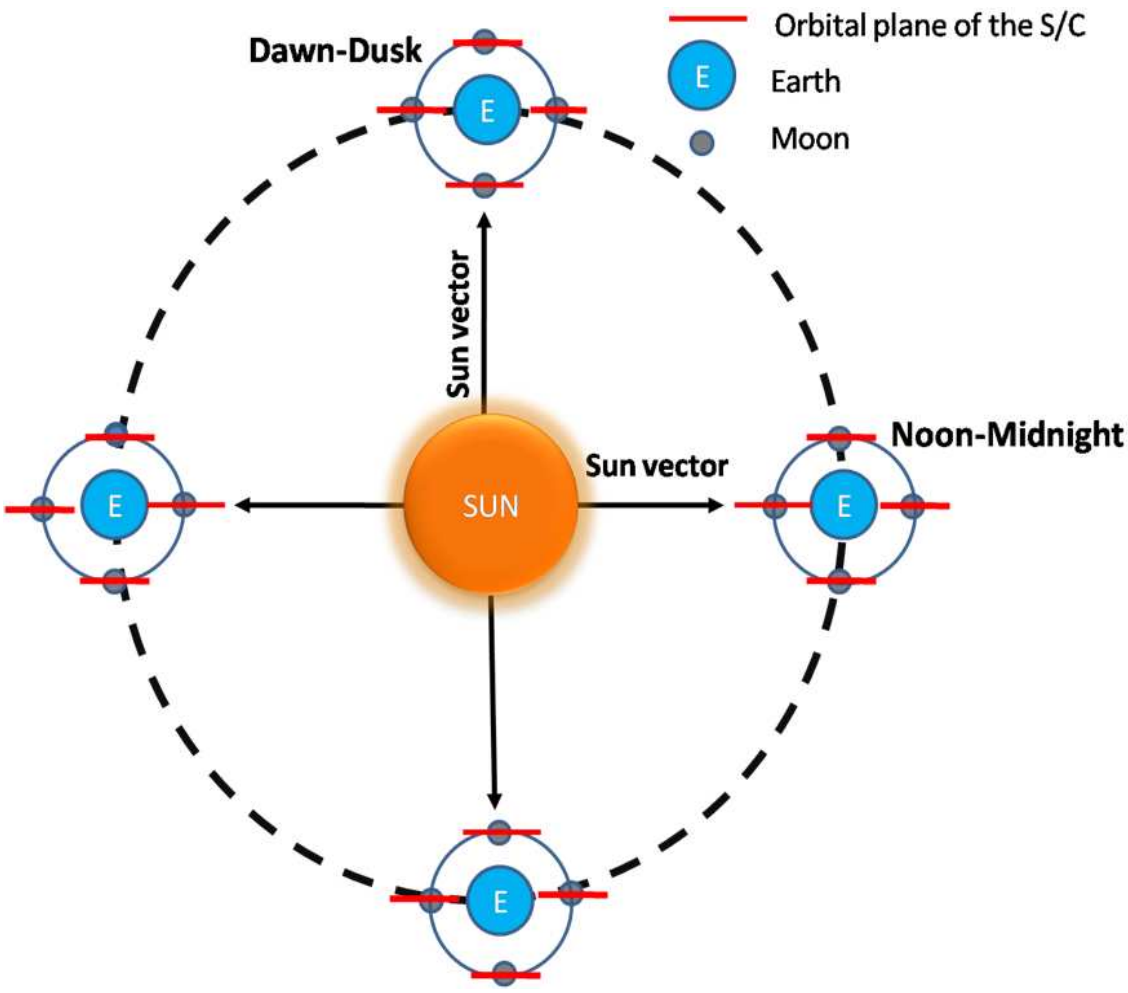

FIGURE 2.3: Noon-midnight and dawn-dusk orbits.

2.3 Chandrayaan-1 X-ray Spectrometer

Solar x-rays can excite x-ray fluorescence (XRF) from the elements in the upper layer of the regolith. The x-ray detectors on C1XS measure the energy and flux of these x-ray photons from the 100 km altitude Chandrayaan-1 orbit. C1XS experiment has the primary objective of global mapping of the major rock forming elements such as Mg, Al, Si, Ca, Ti, Fe on the lunar surface [Crawford et al, 2009]. The K_α and K_β XRF lines of these elements lie in the energy range from 1 to 10 keV. C1XS consists of 24 swept charge devices [Lowe et al, 2001] (a variant of x-ray CCDs) each having a geometric area of $\sim$ 1 cm^2. The passive collimator define the ground pixel resolution of 25 km FWHM (full pixel is 50 km x 50 km). For simultaneous measurement of the solar spectrum in the 1 - 20 keV range, an X-ray Solar Monitor (XSM) was mounted on the top deck of the

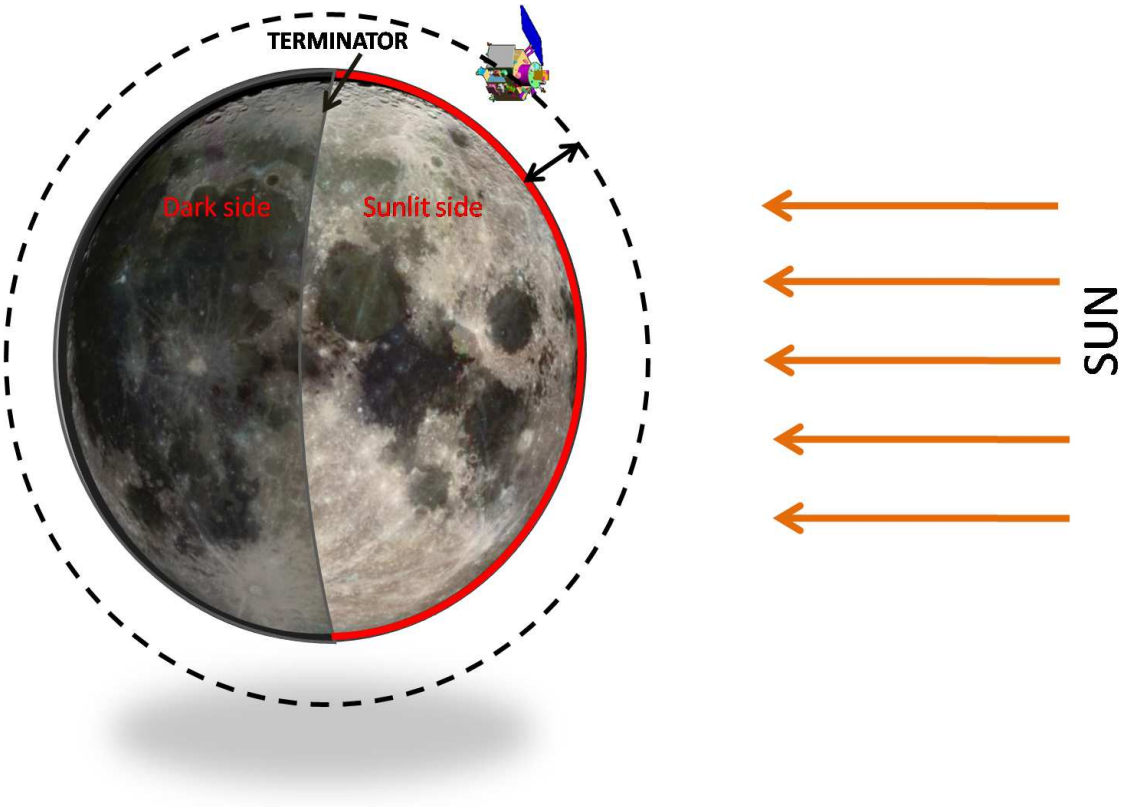

FIGURE 2.4: Observational geometry during noon-midnight phase. The red curve indicates the sunlit region where C1XS is operational.

spacecraft, which had near-continuous visibility of the Sun during the sunlit portion of the orbit.

2.3.1 C1XS instrument

The configuration of the C1XS instrument is described in detail in [Howe et al, 2009]. Briefly, C1XS had two major functional units: detectors and electronics. A schematic diagram is shown in Figure 2.5. The detectors were mounted in front of the electronics unit. The 24 detectors were mounted on ceramic ladders as 6 modules (with 4 detectors on one ladder (Figure 2.6). Each module was mounted on 3 mm copper (which acted as a heat sink to dissipate heat generated while SCDs were in operation) and 6 mm tantalum sheets. Twelve thin (3 mm) Cu straps attached to the ladders took the heat dissipated away from the unit through heat pipes, onto a radiator facing cold space, thus achieving passive cooling of the system.

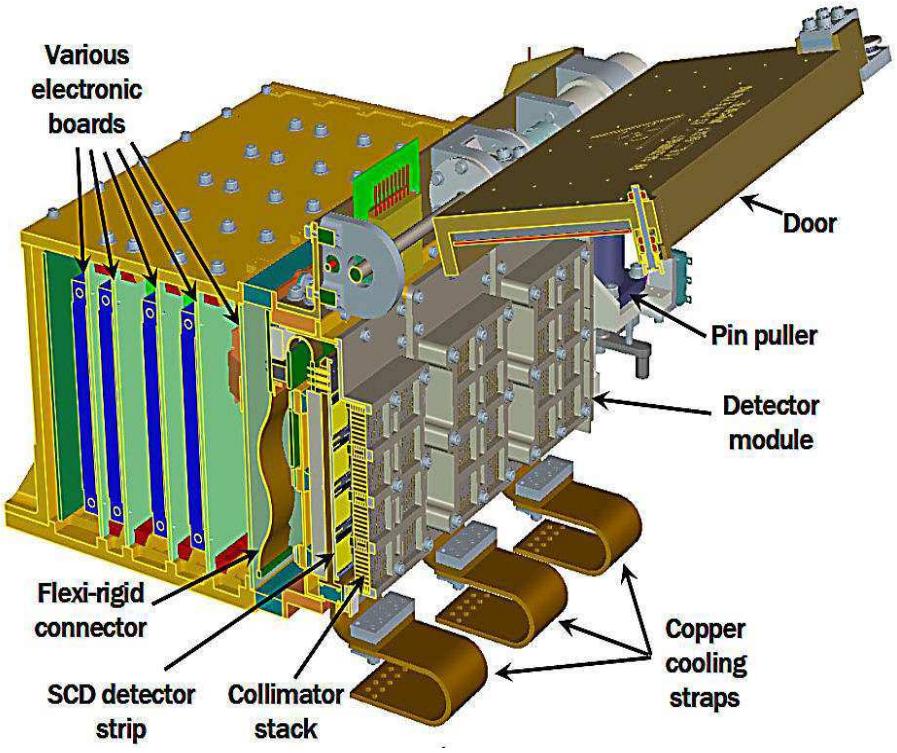

FIGURE 2.5: Schematic view of the C1XS instrument

The electronics was enclosed in an aluminum box of 4 mm thickness. The detector module was protected by an Al door of 4 mm thickness and remained shut during passage through the Earth's radiation belts. The door stops protons of energy up to 30 MeV from reaching the detectors. We carried out a study to estimate the radiation dose on the C1XS detectors during the passage through the radiation belts and further in the lunar orbit during its two year operational phase. To model the incident charged particle flux for the trajectory of Chandrayaan-1, the web interface SPENVIS (Space Environment Information System at http://spenvis.oma.be/) was used. Table 2.2 gives the charged particle flux estimated. For the purpose of radiation tests on ground (which will enable us to study the effects of radiation damage to the devices), the estimated proton flux in the 30 - 100 MeV band was converted to an equivalent flux at 45 MeV and 10 MeV (Table 2.3). Proton irradiation tests [Smith et al, 2009] on ground with this estimated proton flux showed $\sim$ 25% change in energy resolution of the C1XS detectors after passage through radiation belts (with the 4 mm Al door closed) and $\sim$ 150% increase in energy resolution by the end of the 2 year mission.

There were 24 Fe-55 radioactive sources mounted on the door (Figure 2.7) in such a

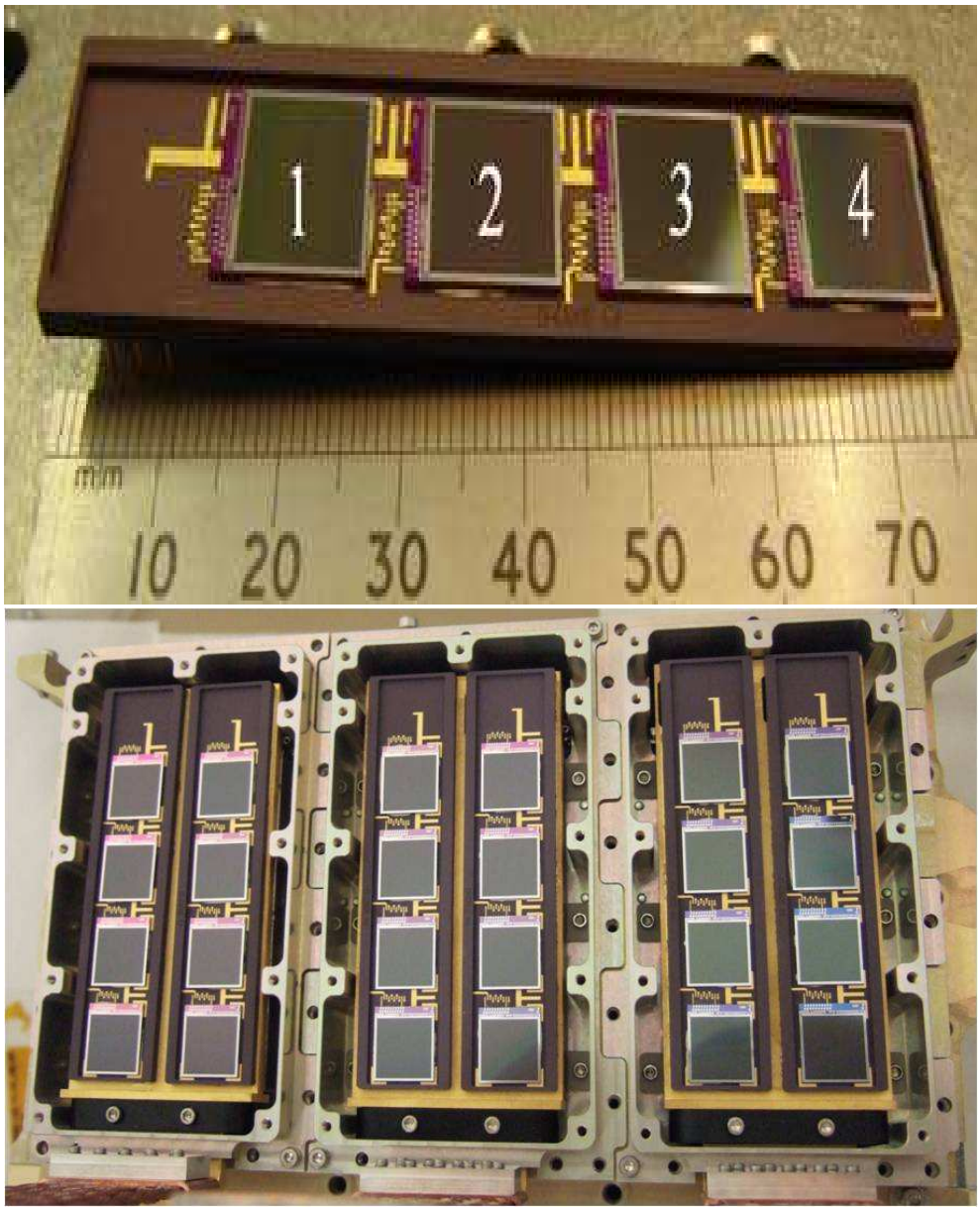

FIGURE 2.6: A single module of detectors (top panel); 24 detectors arranged as 6 modules (bottom panel)

TABLE 2.2: Estimated proton flux for Chandrayaan-1 trajectory and orbital parameters

Proton fluence protons/cm^2	**Trapped protons 0.1-400 MeV**	**Trapped protons $>$ 30 MeV**	**Solar protons 0.1-200 MeV**	**Solar protons $>$30 MeV**	**Total protons $>$30 MeV**
en-route phase (6.5 days)	5.9×10^{17}	6×10^{7}	0.005×10^{17}	negligible	6×10^{7}
lunar orb phase (2 yrs)	negligible	negligible	6.1×10^{11}	3×10^{11}	3×10^{11}

TABLE 2.3: Equivalent fluence for total mission (2 years)

Mission total protons/cm^2	**Without shielding**	**With 4mm Al shielding**
45 MeV equivalent fluence	$\sim 1\times10^{29}$	1.5×10^{10}
10 MeV equivalent fluence	$\sim 1\times10^{23}$	8.7×10^{9}

way that, when the door was closed, they illuminated each of the 24 detectors. An Fe-55 nucleus is inherently unstable (with a half life of 2.7 years) and decays into Mn-55 when its K-shell electron is absorbed by the nucleus. The Mn atom returns to the ground state as an electron from its L or M shell fills the vacancy in the K shell. In this process, a K_α or K_β photon (respectively) is emitted. The sources on the C1XS door were 60 kBq in strength and provided a count rate of $\sim$ 2 counts/s in each detector. To produce additional calibration lines, a 5 μm titanium foil was placed in front of the Fe-55 source. The calibration sources thus provided lines at four energies: 4.5 keV (Ti-K_α), 4.9 keV (Ti-K_β), 5.9 keV (Mn-K_α) and 6.5 keV Mn-K_β.

The field of view defines the ground pixel on the lunar surface and was achieved with mechanical collimator in C1XS. Collimator design involves designing the dimensions (height, shape and open area) and the material from which collimator is made. The material defines the upper energy limit of the collimator for which the FOV is defined. C1XS collimator was designed to define a 50 km x 50 km ground pixel on the lunar surface for the 1-20 keV energy range and were made of Cu coated with gold (to prevent

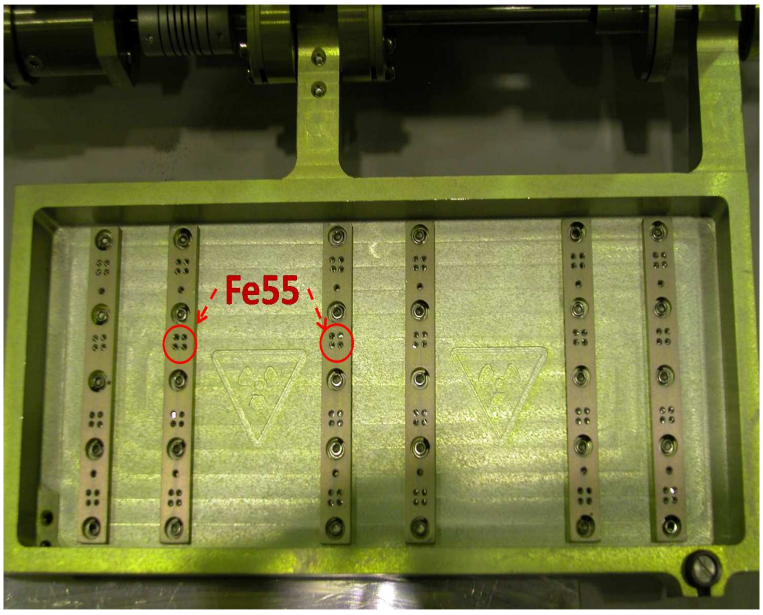

FIGURE 2.7: C1XS door in the open condition (Fe-55 sources are mounted under the strips (with four holes) shown on the door)

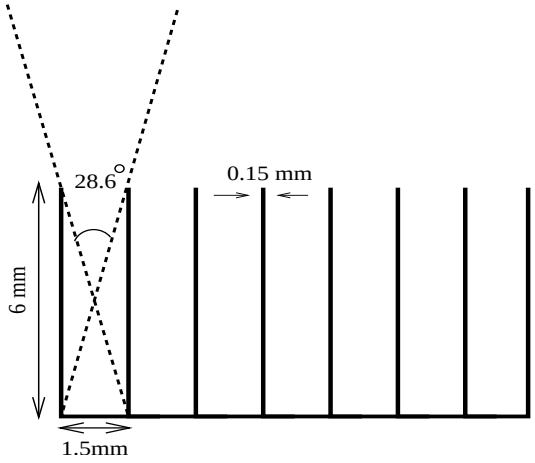

FIGURE 2.8: C1XS collimator with an opening angle of 28.6°

the Cu-K_α line excited by particles or lunar x-rays, from contaminating the measured spectrum).

The collimator (Figure 2.8) was 6 mm long and 0.15 mm thick copper (open area 83%) with a spacing of 1.5 mm between the collimator walls. 1 mm thick modules were made and 6 of them were then stacked one over the other to create the final collimator. They provided an opening angle of 28.6°. A 0.2 μm Al foil supported on 0.2 μm polyamide was mounted on the top and bottom layers of the stack to shield the detectors from visible light.

2.4 Swept Charge Devices

2.4.1 Charge generation

As x-ray photons pass through a medium, they transfer their energy to the medium through any of the following processes:

- **Photoelectric absorption:** The incident photon kicks out an electron from one of the atomic shells of the detection medium. The energy of the ejected electron is given by

$$E_e = E_{incident} - E_{B.E} \tag{2.1}$$

  where $E_{B.E}$ is the binding energy of the atomic shell from which the electron is ejected. Conservation of momentum requires that the atom recoils in the process, but this recoil energy is small and can be neglected.

- **Compton scattering:** This results in the production of a recoil electron and a scattered photon with the division of energy dependent on the scattering angle. In normal circumstances scattering can occur at all angles and hence a continuum of energies can be transferred to the electron.

- **Pair Production:** The process occurs in the intense electric field the nuclei of the absorbing material and corresponds to the creation of an electron positron pair. The incident photon should have a minimum energy of 1.02 MeV for this process to happen.

For x-rays in the energy range of C1XS, photoelectric effect is the most important process and the other two can be safely ignored. In photoelectric effect, x-rays interact at a point inside the detector with the production of many electron-hole pairs in a small spatial region. The energetic electrons accelerated by the applied electric field, produce additional e-h pairs through inelastic collisions with orbital electrons of other atoms in the medium. This leads to charge multiplication and amplification of the signal. The probability of creating secondary pairs is less for holes for a given electric field strength. Setting the E field in such way that only electrons contribute to charge multiplication, the total charge generated by inelastic collisions will be proportional to the primary generated charge ($Q_{primary}$). Since $Q_{primary} \propto E_{incident}$, the x-ray detector can measure the energy of the incident photon.

Semiconductor detectors are widely used as x-ray detectors as their small band gap (the energy level difference between conduction and valence band) is small (1.12 eV for Si at room temperature) compared to gas based detectors (requires $\sim$ 30 eV to create an e-h pair). Moreover, being denser than gas, it is possible to make small detectors retaining good signal levels. Silicon and germanium are the most common of the materials used for making semiconductor detectors.

Though the band gap in silicon is 1.12 eV, the energy required to generate an e-h pair is 3.64 eV for photon energies which are large compared to the bandgap. This is because, at higher energies, there are losses due to transfer of energy to phonons (lattice vibrations). The number of electrons generated by a photon of energy $E_{incident}$ (in units of eV) in silicon can be calculated as $\frac{E_{incident}}{3.64}$.

Photons with energy from 1.1 to 3.1 eV (11263 Å- 4000 Å) generate a single e-h pair in the silicon. This spectral range covers the visible spectrum from 4000 Åto 7000 Å. SCDs are thus sensitive to visible light and should be shielded so that optical photons do not interact in the active region of the silicon. The shielding is achieved with Al foils as mentioned in the previous section.

The Swept Charge Devices (hereafter SCDs) (CCD-54 manufactured by e2V technologies ltd) are a variant of traditional x-ray CCDs (can be considered as 1-D linear sensors). These were used since 24 SCDs translate to $\sim$ 24 cm^2 of geometric area and unlike traditional x-ray CCDs, provide high spectral resolution within benign operating temperature range of -20 to 0 deg C ($\sim$130 eV @ 5.9 keV at -20 deg).

2.4.2 SCD structure

A layer of p type (silicon doped with boron; has a large concentration of holes) silicon (called the epitaxial layer) is grown on a p+ (heavily doped) substrate (which is a dead region from which charge is not collected during operation). An n type (silicon doped with phosphorous; has a large concentration of electrons) region is created in the epitaxial region by ion implantation and this forms the buried-channels. An oxide (SiO_2) layer is generated on the epitaxial silicon and acts as an insulator. Polysilicon electrodes are created on the surface. The polysi-oxide-n type region forms a Metal-Oxide-Semiconductor (MOS) structure. A p-n junction is formed inside the SCD between the n type buried-channel and p type epitaxial layer.

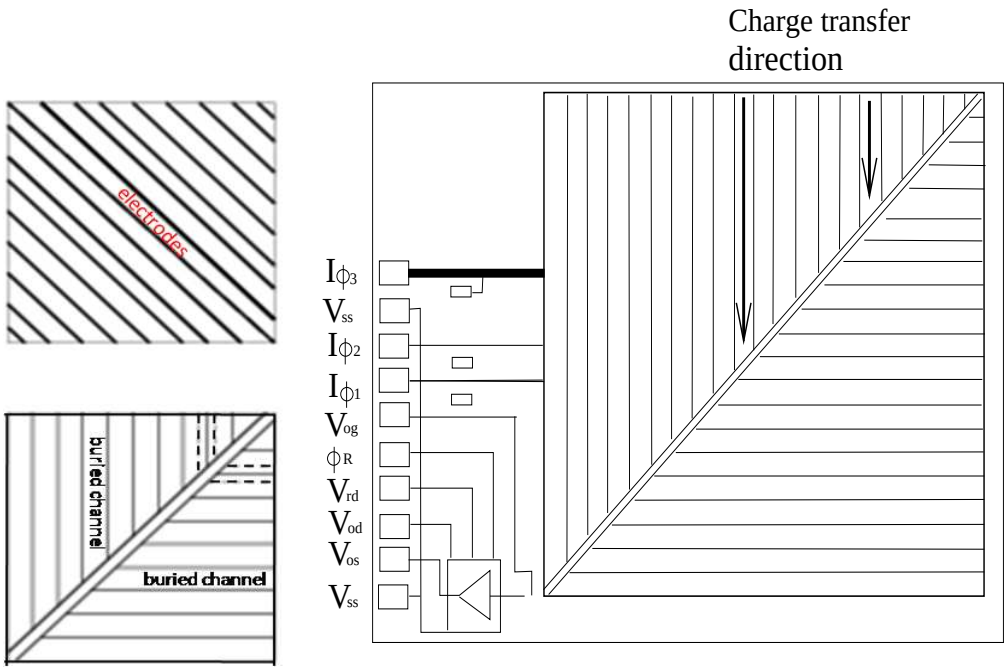

FIGURE 2.9: Upper left figure shows the electrodes arranged diagonally and the lower one shows the buried-channels arranged in herring bone structure (dotted lines indicate the isolation channels on either side of a buried-channel). Figure on the right (re-drawn from [Smith et al, 2009]) shows the SCD layout and the direction of charge transfer.

The buried-channels are arranged in a herring bone structure (see lower left corner of Figure 2.9). Electrodes are diagonally arranged over this (see upper left in Figure 2.9). Like in any x-ray CCD, the charge generated in the device is transferred from one pixel to another by applying a clock voltage to the electrodes. A three phase clocking is applied to transfer the charge collected in the buried-channels to the central diagonal and further towards the node amplifier at the lower left hand corner of the device.

The primary difference from x-ray CCDs is that SCDs are not position sensitive and hence cannot be used for x-ray imaging. While in x-ray CCDS, we can associate the charge read out to the pixel where it was generated, in SCDs, this information is lost.

2.4.3 Charge collection and transport

The n-p junction formed at the n type buried-channel and the epitaxial p type layer forms the basis of charge collection in the SCD (as well as in x-ray CCDs). Mobile holes from the p side diffuse to the n region and electrons from n region to p, thus forming a small depletion region at the n-p interface. When the n-p junction is reverse biased

(by applying a positive voltage to the n side with respect to the voltage on the p side), the depletion region is widened due to further repulsion of mobile charges from the n-p junction.

The electrode-oxide-n type region forms a n-type MOS structure. When the bias voltage V_G applied to the gate electrode is negative with respect to the channel potential (which is maximum at the boundary of the n contact to the oxide and decreases towards the p type region), electrons in the n type region are repelled away from the n-oxide contact region. A positive charge region is formed at the n type oxide boundary thus creating a depletion region. The channel potential drops as it approaches this region (Figure 2.10). As the bias voltage is increased, the depletion regions at the n-p junction and the n-oxide interface become larger. A point is reached where both depletion regions merge and the depletion region extends from the n-oxide surface deep into the p region (through the n type buried-channel). The maximum channel potential occurs where both depletion regions meet, inside the buried-channel. When a x-ray photon generates a free electron by photoelectric effect, the electron moves towards the region of highest potential and is trapped there. The charge that is generated by the x-ray photon thus gets collected in the buried-channel.

If V_J is the potential at the n-p junction, and the doping concentration in the n region (N_D in atoms/cm^3) is $>>$ that in the p region (N_A in atoms/cm^3), the depletion depth (x_p) in the p region is given by [Janesick, 2000]

$$x_p = \sqrt{\frac{2\epsilon_{Si} V_J}{qN_A}} \tag{2.2}$$

where ϵ_{Si} is the permittivity of silicon (1.04×10^{-12}) and q is the charge of the electron (1.6×10^{-19} C).

The charge collected in the buried-channel is swept across the device by applying a clocking voltage. Figure 2.11 shows schematically, the transfer of charge in a three phase clock device. ϕ_1 ϕ_2 and ϕ_3 are the voltages applied to three adjacent electrodes. These clock voltages are varied in such a way that the channel potential under the electrode to which the charge has to be transferred, is the maximum. The charge thus moves along the buried-channel.

C1XS - SCDs are clocked in a mode called 'multipinned-phase mode' (MPP) which suppresses the dark current. Dark current is the intrinsic charge that occurs in the device

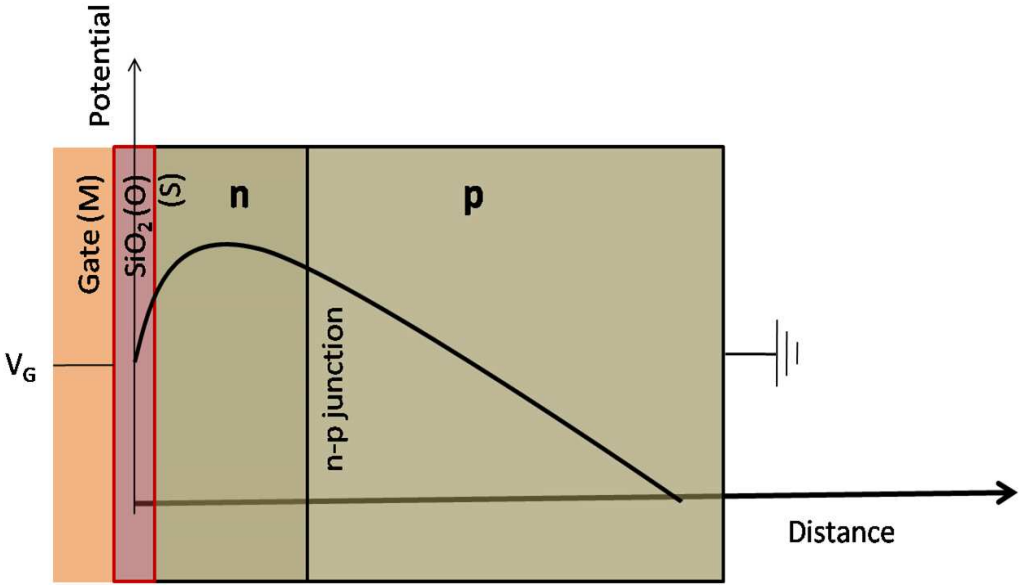

FIGURE 2.10: Potential well created inside the SCD

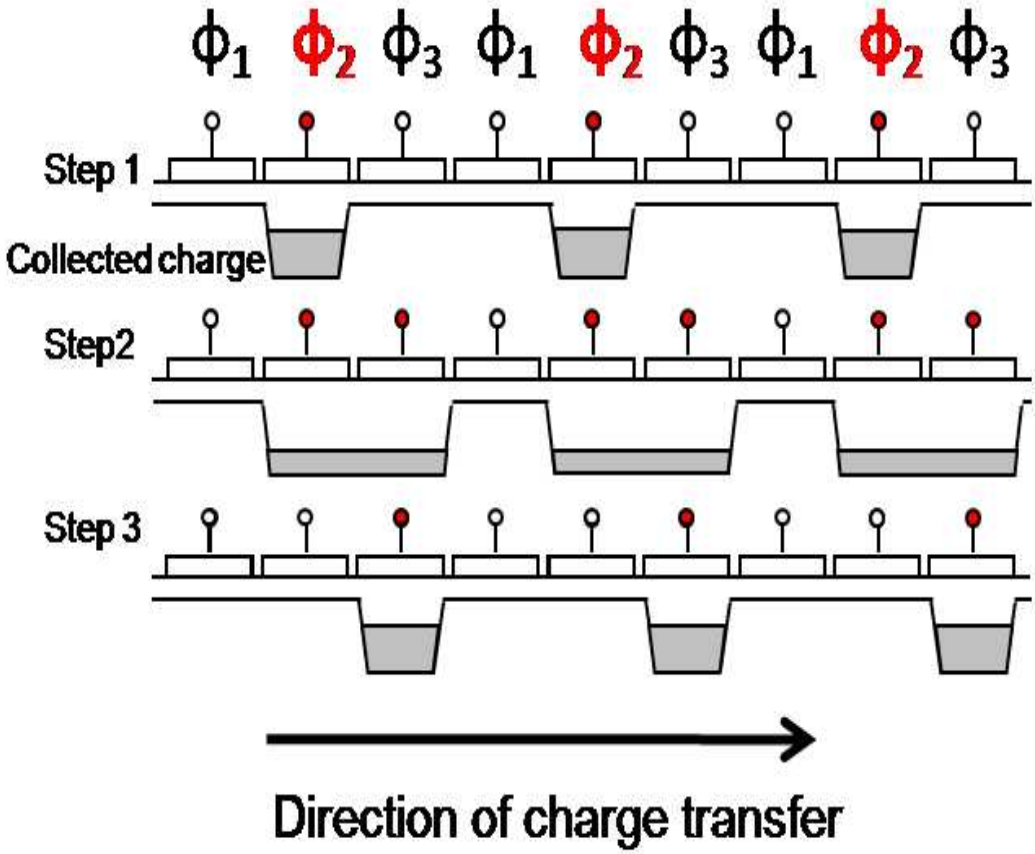

FIGURE 2.11: Charge transfer in CCDs

as a result of thermally generated electrons. The dominant source of these electrons is the gate- oxide surface interface. If the gate voltage is brought down so that the surface potential becomes equal to the potential at the substrate, holes from the channel stop region are attracted towards the gate-oxide interface. The free electrons in the gate-oxide interface (produced by dangling bonds at the interface as the lattice structure here is more irregular than in pure Si, due to the manufacturing process) combine with the holes, suppressing their contribution to the signal (ie lesser dark current added to the signal). This is called the 'pinned state' or 'inverted' state. The layer of holes at the surface is conductive and shields the potential well from being affected by changes in the gate voltage. During multipinned mode clocking, SCDs are brought to the inverted state at regular intervals at a rate faster than charge transfer, so that the surface states always remain filled. The dark current is thus reduced resulting in better performance of the detector.

2.4.4 C1XS SCDs

C1XS - SCDs (CCD-54) have 1725 diagonal electrodes (each of width 8.5 μm) made of polysilicon. Isolation channels (to isolate a buried-channel from the surrounding silicon so that charge remains contained in the buried-channel; these are called channel stops and made of a insulating material) and buried-channels (Figure 2.9) in the underlying silicon arranged in a herring bone structure, pitch of channel stops being 25 μm. Charge collected in each diagonal element has to move through the same number of clock cycles to reach the read out node at the bottom left. The length of the central diagonal is $\sim$ 1.5 cm and 575 clock triplets are required to read out the whole device area. Therefore essentially the SCD is read out like a linear pixel array.

The read out is achieved through continuous clocking at a frequency of 87.5 kHz. The pixels are taken in and out of inversion (MPP mode) at a rate faster than the life time of surface state traps. These states thus remain filled. This technique of clocking is called 'dither mode' clocking.

The charge read out is fed into a current mode pre-amplifier. The signals from SCDs flow through 3 main blocks: signal amplification, digitization and event recognition.

The output of the SCD goes to a correlated double sampling (CDS) circuit which selects the x-ray events according to the programmed criteria. The CDS effectively filters noise in the system improving the energy resolution of the detectors. To do this, the output

node is first set to a reference value. The pixel charge is then transferred to the output node. The final value of the charge assigned to this pixel is the difference between the reference value plus the transferred charge. The 24 SCD signals are converted to digital data by the analog to digital converter (ADC). There are 4096 ADC channels in C1XS and therefore the photons are binned into 4096 channels to generate a pulse height spectrum. A detailed discussion of the processing electronics can be found in [Howe et al, 2009].

2.5 C1XS event processing

There are 2 event processing modes primarily to control data volume (which depend on various factors like available memory on-board for storage, data downlink capabilities, time resolution required and event rates) for varying input event rates.

- **Time tagged mode:** Events are processed in this mode when the event rate is low. Each event is tagged with on-board time and SCD number. There are again two modes under this depending on how the events are selected (Figure 2.12).
  - Type 11 data packets: As long as the event rates are below 320 events/s (determined by the fixed data packet length of 280 bytes in C1XS), the instrument generates type 11 packets. The events from adjacent 3 pixels are stored, provided, out of a group of adjacent 3 pixels, the central pixel is above threshold 1 and pixels on either side are above threshold 2.
  - Type 10 data packets: When the event rate is between 320 events/s and 800 events/s, type 10 data packets are generated. In this mode, a group of 3 adjacent pixels, the event in only the central pixel is stored provided, the central value is above threshold 1 and if events before and after are below threshold 2. If the central pixel is above threshold 1 and events on either side are above 2, the event is discarded.
- **Spectral mode:** Events are collected for a specific integration time (8 s) and a packet is generated.
  - Type 12 data packets: For event rates above 800 events/s, individual event information is not retained. Spectrum is generated on-board and the 4096 channels are re-binned to 512 channels. The event selection logic is as in type 10.

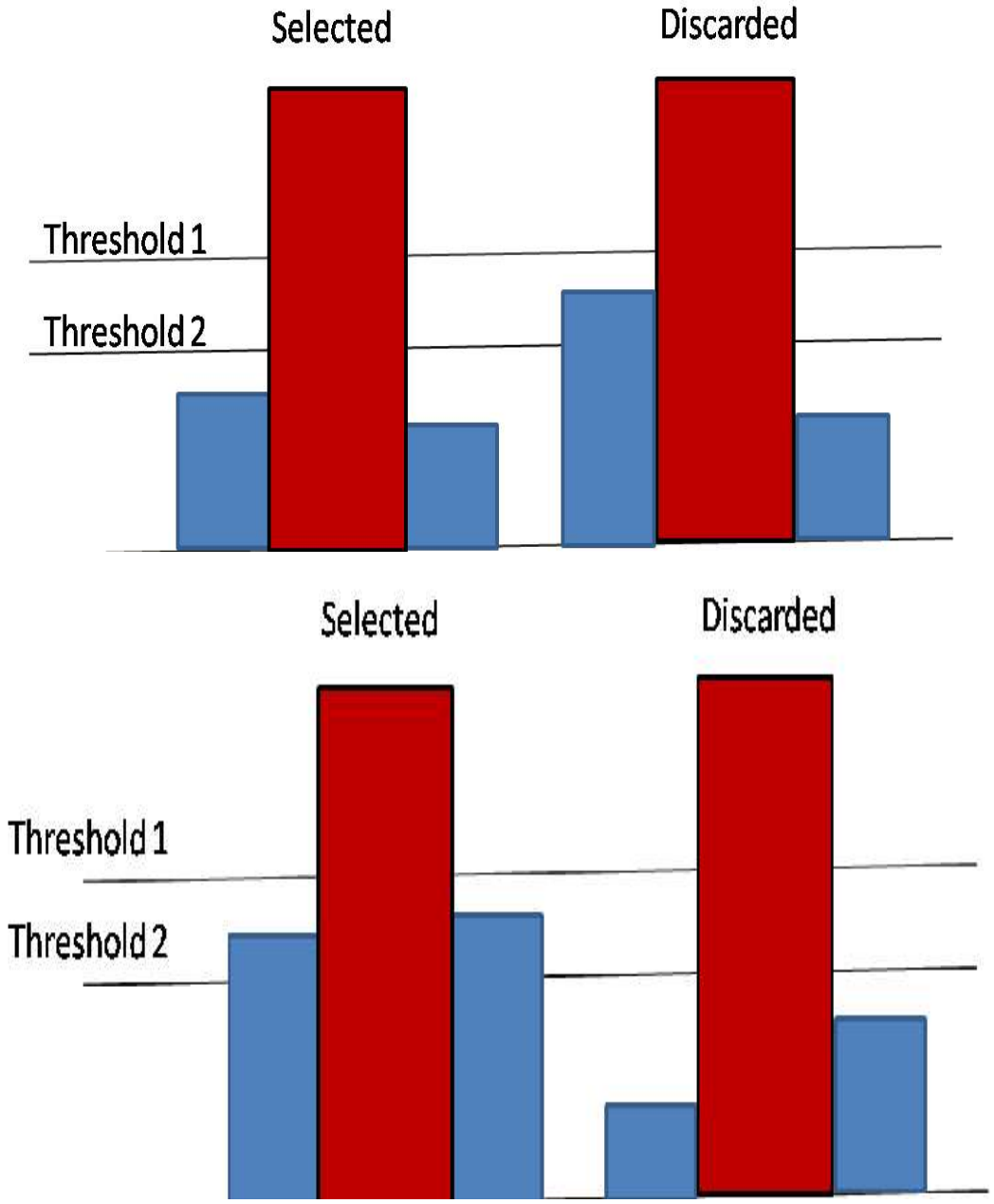

FIGURE 2.12: Event processing modes: type 10 (upper) and 11 (lower) in C1XS

TABLE 2.4: Binning scheme in Type 12 packet type

Raw bin numbers	Bin width (Type 12)	Type 12 bin numbers
0-999	4	0-249
1000-2103	8	250-387
2104-4071	16	388-510
4072-4095	24	511

The thresholds 1 and 2 are stored on-board and can be changed by telecommand if necessary. Apart from the above three there are nine more data packet types in C1XS. Type 9 packets store the noise levels or **'zero peak'** channel number. The zero peak is measured (using a reset pulse having the same frequency as the clock cycle- 87.5 kHz) by setting the event threshold to zero for a short duration (1 μs). So CDS outputs the difference in the readout reference value across the short time interval. The value of the zero peak thus measured, is stored only once in every 4 s (to restrict the data volume). The type 9 data gives the zero peak position in ADC channel number (4096 scheme) by fitting the Gaussian distribution of zero peak values in a data packet. Zero peak is a measure of the average noise in the system (dark current and electronic noise). The value of the zero peak therefore increases as temperature increases. The offset between the zero peak and the low energy threshold is fixed so that even as the noise in the system increases, the event selection still ensures efficient filtering of real x-ray events.

There are 3 functional modes for C1XS:

1. **Operating mode:** This is the nominal mode while C1XS collects lunar observational data.
2. **Resting mode:** C1XS automatically goes into this mode based on the detector temperature exceeding a set threshold. The SCDs do not receive power and hence do not collect data in this mode. But C1XS generates packets every 64 s (nominally) containing house keeping parameters. If either the temperature of the SCDs (as measured by sensors at either end of the SCD facet) rises above -5°C, or if the electronics box temperature goes above 30°C or the 3D+ chip (which includes the CDS circuit and ADC) temperature goes above 40°C, the on-board software logic puts C1XS into this mode. As the temperature decreases below another set limit, C1XS is automatically switched into the operating mode.
3. **Standby mode:** This is functionally similar to the resting mode but is achieved with a telecommand.

2.6 X-ray Solar Monitor (XSM)

In order to derive the elemental abundance from x-ray line flux, it is critical to accurately measure the incident solar spectrum. The solar spectra during flares are highly variable in time and intensity. XSM (Figure 2.13) operating in the 1.8-20 keV energy range was a

FIGURE 2.13: X-ray Solar Monitor. The aperture through which x-rays reach the detector, is marked (the closed shutter can also be seen)

Si-PIN detector to continuously monitor the solar x-ray spectrum with a time resolution of 16 s. It was developed by the University of Helsinki in Finland. It had a wide opening angle of 105° to ensure that Sun was always in the field of view. The FOV is defined by an aperture of diameter 0.01 mm^2 in front of the detector. The aperture also cut down the flux thus ensuring that the detector was not saturated during intense flares. The detector was cooled on-board to around -18°C using a peltier cooler. XSM also had a shutter on which an Fe-55 radioisotope (with a Ti foil) was attached so as to enable on-board calibration.

This instrument apart from being an essential part of C1XS experiment, provided a platform for doing independent soft x-ray studies of the Sun.

2.7 Summary

The C1XS instrument was built at the Rutherford Appleton Laboratory in UK and funded by the European Space Agency (ESA) with partial support from ISRO. The work reported in this thesis deals with the detailed ground calibration of the SCDs, modeling the instrument response and derivation of first results from on-board lunar x-ray fluorescence data using this. These are addressed in the subsequent chapters. This chapter aimed at providing essential background material on the design of C1XS, its nominal operating modes and data products, necessary to understand better, the discussion in the following chapters.

Chapter 3

Calibration of the Swept Charge Devices on C1XS

3.1 Introduction

The primary objective of C1XS, was to determine the absolute abundance of the major elements on the lunar surface. The x-ray spectrum from the lunar surface consists of line emissions embedded in a continuum. The continuum in the spectrum arises from background in the detector and the x-ray photons scattered from the lunar surface. The total counts under the x-ray lines have to be determined accurately, in order to convert them to absolute abundance of corresponding elements. The original x-ray spectrum emitted from the source is modified as a result of the interaction of x-ray photons with the detector elements to produce the distribution of x-ray counts over the energy range of the detector.

Observed x-ray count rate (cts/s)= absolute line flux (photons/cm^2/s)
* spectral response of the detector

where * represents convolution.

X-ray photons interacting in the active volume of the detector, generate a charge cloud. When completely read out, this charge cloud yields a peak in the energy spectrum which has a Gaussian distribution and is called the **photopeak**. In practice, the probability distribution from a mono-energetic beam of x-ray photons has additional components,

the knowledge of which, is essential to deconvolve the incident spectrum. The observed response of the detector to a beam of mono-energetic photons can be characterized by a function termed as the **spectral redistribution function (SRF)**. It describes how a photon of a specific energy gets re-distributed across the observed ADC channels.

The SRF is a function of energy of the incident photons, temperature and event rate. Being large area detectors, SCDs are prone to saturation effects such as pile up, when the event rates are high. Hence it was necessary to study the SRF parameters of the SCD as a function of energy, temperature and event rate. Since determination of absolute x-ray line flux is of prime importance, it was also necessary to calibrate the detectors against a known source to determine the detection efficiency. Therefore, C1XS underwent a detailed ground calibration at the RESIK x-ray beam facility [Lang et al, 1993] at the Rutherford Appleton Laboratory (RAL) in UK. The SRF of the detector was determined from measurements using a double crystal monochromator in the RESIK x-ray beam-line. A Si-PIN detector calibrated using the monochromator beam-lines at the synchrotron facility at PTB/BESSY II ([Thornagel et al, 2001], [Richter et al, 2004]) was used as a transfer standard and the detection efficiency of the SCD was determined relative to this.

In this chapter, we first describe the procedures adopted for calibration, calibration data analysis and SRF modeling. The detection efficiency of the SCD relative to the reference detector, is also determined.

3.2 Detector response

X-ray photons incident on the SCD should interact in the depletion region in the SCD and the resultant charge should get collected in the buried-channels in order to be read out and recognized as an event. The x-ray spectrum incident on the detector, undergoes modifications due to interactions in the different structures of the detector. For example, the gates on the SCD absorb low energy x-ray photons and thus all the incident x-ray photons do not reach the active region of the detector. The primary elements of an instrument response are the spectral redistribution function (SRF), detection efficiency and collimator response all being functions of the incident photon energy. The instrument response is a convolution of these three terms. The construction of the instrument response is described in detail in the sections that follow.

3.2.1 Spectral redistribution function (SRF)

The x-ray photon interacting in the depletion region of the detector yields a charge cloud which is then read out and converted to an equivalent voltage pulse. In an ideal detector, a monochromatic beam of photons would yield an equal number of voltage pulses with the same amplitude and the resulting spectrum would be represented by a delta function. But in practice, the voltage pulses are redistributed in pulse height space (and hence in energy space). A representation of the resulting distribution is called the spectral redistribution function (Figure 3.1). Conventionally, analytical physical models and Monte Carlo simulations have been employed for describing the SRF ([Bautz et al, 1999], [Scholze and Procop, 2001], [Sood et al, 2004], [Scholze and Procop, 2006]). These require a physical model of charge transport in the detector and prediction of the shape of the SRF using simulations. If a precise physical model for charge transport in the detectors can be constructed and the predictions match observations, the SRF at any energy can be constructed. But in the case of devices where a physical model cannot be easily found, we can use mathematical functions to fit the observed SRF at discrete energies and then extend it to cover the energy range of interest. In this work, we have adopted the traditionally used empirically-derived HYPERMET function [Philips and Marlow, 1976]. The components of the HYPERMET function have been associated with a physical model and is described in [Bautz et al, 1999]. We have incorporated additional mathematical functions, to model the SRF of the SCDs accurately. We have the following components in the SRF.

- **Photopeak**: The incident beam of monochromatic photons (a delta function) is spread into a Gaussian distribution P(x) of voltage pulses given by

$$P(x) = S_1 e^{\frac{-(x-x_0)^2}{2\sigma_1^2}} \tag{3.1}$$

  The centroid x_0 of the Gaussian determines the energy of the incident x-ray photon and S_1 is the normalization factor. The intrinsic shape of x-ray fluorescent lines which are what is of interest to C1XS, is a Lorentzian function. Ideally, a function which convolves a Lorentzian with a Gaussian, called the Voigt function should be used to fit the photopeak. Approximations to the Voigt function are often used because of the complexity involved. The width of the Lorentzian for the XRF lines of interest are $\sim$10 eV, which when compared to the detector energy resolution of

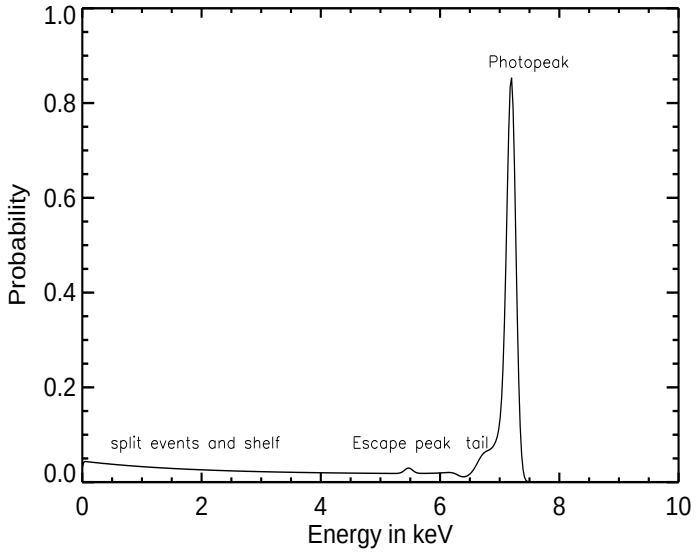

FIGURE 3.1: Redistribution of a monochromatic beam of photons

the order of 100 eV, is small. To simplify the spectral analysis, we have used the much simpler Gaussian function to model the photopeak.

The functional relation between ADC channels (x) and incident energy (E_0) is obtained by measuring x_0 at various energies E_0. Since the charge collected is proportional to the incident x-ray photon energy, the amplitude of the pulse (and hence x_0) generated should vary linearly with energy:

$$N = \frac{E_0}{\omega} \tag{3.2}$$

where N represents the number of electrons generated by an x-ray photon of energy E_0 and ω the energy required to generate one electron-hole pair. This electron charge cloud is then read out and converted to a voltage pulse by the associated electronics and further digitized by the ADC. The ratio of incident photon energy to ADC channel number is termed as the gain of the detector. Assuming E_0 =0 when channel=0, gain G

$$G = \frac{E_0}{x_0} \quad or \quad E_0 = Gx_0 \tag{3.3}$$

In practice, deviations from linearity of up to 1% in gain have been observed near the absorption edge [Owens et al, 1996] of the detector material, because of the deviations in the value of ω.

The spread σ_1 arise from two sources:

- Fano broadening(σ_F): The incident x-ray photon interacts with the material of the detector (Si in our case) and generate e-h pairs. A part of the energy of the x-ray photons also goes into phonons (lattice vibrations) and finally into thermal energy. This fraction depends mainly on the detector material (except at energies near the band gap). If E is the energy of the incident x-ray photon, the number of electrons generated will fluctuate about a mean value N.

$$< \Delta N >^2 = F.N \tag{3.4}$$

  where F is the Fano factor and has a value between 0 and 1. If all the energy of the incident x-ray photon is used for e-h pair generation, then F=0. The statistical variation of the number of e-h pairs thus depend on F and ω. Both F and ω are shown to have dependence on E and temperature, particularly at energies of a few 100 eV [Owens et al, 1996]. At low energies, incident photon energy loss by electron-phonon interaction and plasmon (collective electron oscillations) excitations, which depend on E and temperature are important and hence the dependence. We will ignore this effect in our analysis of 1-10 keV data and take the room temperature value of 3.64 eV [Owens et al, 1996] for ω in silicon for our calculations.
- Processing noise (σ_P): The charge collected is transferred from pixel to pixel, read out and further processed by the different components of the associated electronics. Electrons can be added or removed from the charge packet during the transfer process. This component called 'read out noise' increases with clocking frequency as well as temperature. The associated electronics will also contribute electrons, further broadening the distribution and is also temperature dependent. We use a common term 'processing noise' for all these components.

Classically, all components are assumed to be normally distributed and independent and thus the terms add in quadrature.

$$\begin{aligned} \sigma^2 &= {\sigma_F}^2 + {\sigma_P}^2 \\ &= \omega\sqrt{r(T)^2 + \frac{F.E}{\omega}} \end{aligned} \tag{3.5}$$

where r (T) represents the processing noise in units of number of electrons. The energy resolution of the detector in terms of full width at half maximum (FWHM) can be written as

$$FWHM(E,T) = 2.35 \times \omega\sqrt{(r(T)^2 + \frac{F.E}{\omega})} \tag{3.6}$$

where T is the operating temperature.

- **Low energy tail**: The charge generated has to be collected completely, in order to optimize sensitivity and to maintain the linearity between ADC channels and energy. This is not always achieved and the incomplete charge collection results in a tailing feature at the lower energy side of the photopeak. The x-ray photon incident on the detector generates a charge cloud of radius R at a depth d in the active volume of the detector. If the charge cloud is formed at the interface of the dead layer and the active region, some of the charge is lost and the resulting channel number registered would correspond to a lower energy than that expected of the true incident photon. The fraction of charge lost, can vary between 0 and 1. The tailing, therefore is a continuous distribution starting from x_0 to a channel x_i (where $x_i < x_0$). Further, since d and R are a function of E, the low energy tailing will also be a function of E. The tailing will decrease with E as higher energy photons would interact at a greater d.

  The shape of this low energy tail is typically an exponential. Convolving the exponential with a Gaussian (since each photon that is part of the low energy tail distribution, suffers a Gaussian spread for the same reasons as that for the incident photon.), we get the following expression [Philips and Marlow, 1976]

$$LE\ tail \quad = \quad 0.5 S_2 e^{\frac{(E-E_0)}{\beta_1}} \times erfc\,(\frac{E-E_0}{\sqrt{2}\sigma_1} + \frac{\sqrt{2}\sigma_1}{2\beta_1}) \tag{3.7}$$

- **Low energy shelf**: The gate structures, oxide coatings and filters above the active region of the detector form a *'dead'* layer. X-ray photons have a definite probability of interaction in the dead layer generating photo or Auger electrons. Charge generated as a result of interactions in the dead layer is mostly not read out and hence lost. However, those electrons with sufficient energy, drift toward the buried-channel and get *'detected'*. This results in a shelf feature which extends from the photopeak to low energies. This distribution can be modeled as a step function [Philips and Marlow, 1976]

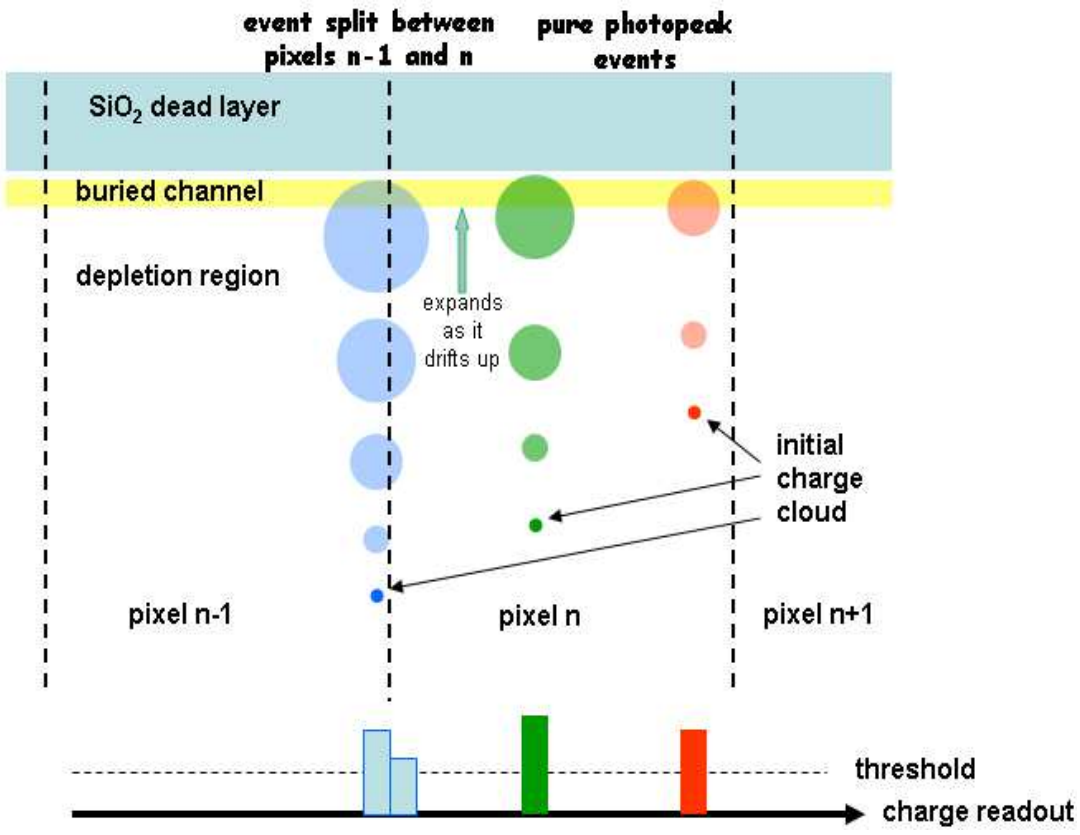

FIGURE 3.2: Schematic diagram of charge clouds getting split between pixels

$$LE\ shelf \quad = \quad 0.5 S_3 erfc\left(\frac{x - x_0}{\sqrt{2}\sigma_1}\right) \tag{3.8}$$

- **Split events**: The charge cloud generated in the depletion region is under the influence of an electric field and hence moves in the direction of this field. The radius of the cloud increases as it drifts towards the buried-channel. If the charge cloud spreads to the adjacent pixel, before getting collected by the buried-channel, the charge is split. The resulting pulse read out will indicate multiple 'bit' pixels, all with lower amplitudes and will be registered as photon events of lower energy. The number of such *split events* increases with increase in energy of the photon (Figure 3.2). Higher energy photons interact at a greater depth in the detector and hence will suffer a greater spread as they drift toward the buried-channel where they get collected. This component is not a part of the HYPERMET function. We have modeled this as a purely mathematical function which fits the observed data and this will be discussed further in a later section.

- **Escape peak**: Incident x-ray photons have a finite probability to excite x-ray fluorescence from silicon, the base material of the sensor. This x-ray fluorescence photon propagates as a different charge cloud, and largely deposits its entire energy in the detector. However, if the XRF photons escape the detector volume without further interaction, the resulting total charge generated will be equivalent to a reduced energy equal to the difference between incident photon energy and fluorescent photon energy (1.75 keV in silicon). This is an independent photon as seen by the detector and has a pulse height spread characterized by a Gaussian. Since the incident photon generated this charge, the escape peak is considered as part of SRF. This is modeled as a Gaussian function.
- **Fluorescent peak**: Interaction of x-ray photons in the dead layer can also produce XRF photons which might drift into the potential well of the buried-channel. This results in a Gaussian distribution in the spectrum at 1.75 keV in silicon.

The spectral redistribution function as a function of energy E, is a sum of all the above features and can be expressed as :

$$\begin{aligned}\text{SRF (E, C, T)} = {} & \text{photo peak} + \text{low energy tail} + \text{low energy shelf} + \text{split events} \\ & + \text{escape peak}\end{aligned}$$

3.2.2 Detection efficiency

Structures in the device where the charge is not collected from, such as the gates and oxide layers, can be termed as *dead*. X-ray photons may get absorbed in these layers before they reach the depletion region. As a result, lesser number of photons reach the depletion region wherein they are detected. X-ray photons that interact at a depth greater than the depletion edge of the detector volume, also generate a charge cloud in the field free region of the substrate. This charge cloud then drifts randomly. When the charge cloud gets into the depletion region (where there is an electric field), they are collected in the buried-channel. This results in loss of charge not accounted for, in the SRF. Again, as the charge is read out across the device, there can be losses due to recombination which also contributes to the total charge loss.

The loss of photons in the dead layer can be calculated from their interaction cross sections. The cross section of the swept charge device is shown in Figure 3.3. The gates

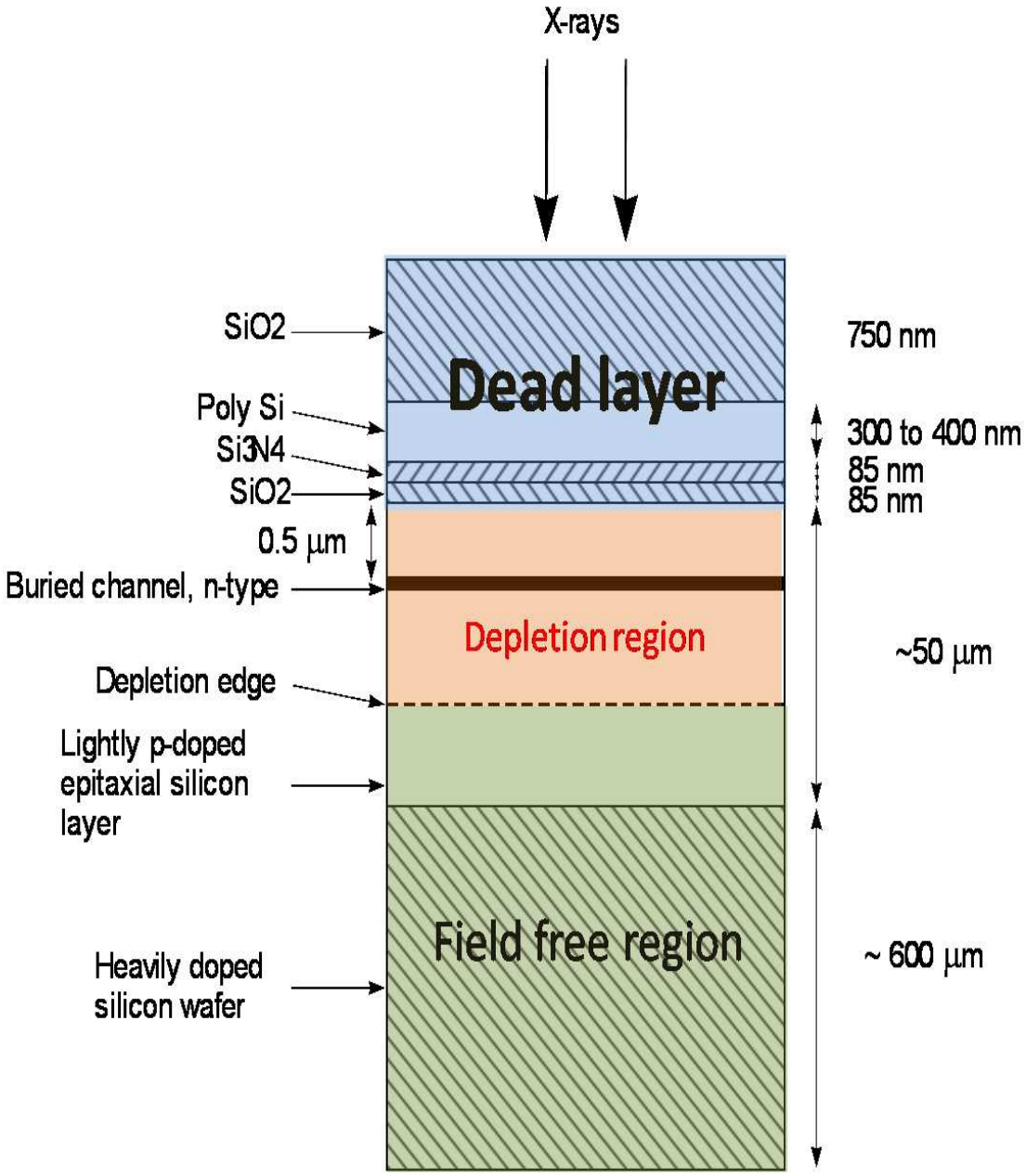

FIGURE 3.3: Structure of CCD 54

and oxide layers contribute less than 2 μm to the dead layer. The efficiency of the SCD can be expressed as

$$\epsilon_{SCD}(E) = e^{-\mu(E)d} \times (1 - e^{-\mu(E)a}) \times r \tag{3.9}$$

where *'r'* accounts for losses due to recombination and read out, *'d'* is the thickness of the dead layer and *'a'* that of the depletion region.

3.2.3 Collimator response

The effective area of the instrument as a function of the angle of incidence of the x-ray photon is given by :

$$\frac{A^{'}(E,\theta_i)}{A(E,\theta_i)} = 1 - \frac{tan\theta_i}{tan\theta_{max}} \tag{3.10}$$

θ_{max} defines the field of view of the instrument. The full width at half maximum (FWHM) is defined as the angle where the effective area is half the maximum and can be shown to be equal to $\frac{\theta_{max}}{2}$. C1XS has an opening angle of 14.3° (FWHM) which translates to a FWHM ground pixel of 25 km x 25 km from an altitude of 100 km above the lunar surface. The collimator response is a function of energy as well, for angles of incidence θ_i slightly greater than θ_{max}. This is because of the transmission of high energy photons through the finite thickness of the collimator walls as illustrated in Figure 3.4. For the 1-10 keV range of C1XS, the collimator response defines a 25 km FWHM pixel on the lunar surface.

3.2.4 Response matrix

A two dimensional matrix where each element R_{ij} gives the probability that a photon of energy j gets registered in channel i is called the response matrix and is a convenient way of representing the instrument response.

The response of the detector can be defined as

$$M(I) = \int R(I,E)A(E)S(E) \tag{3.11}$$

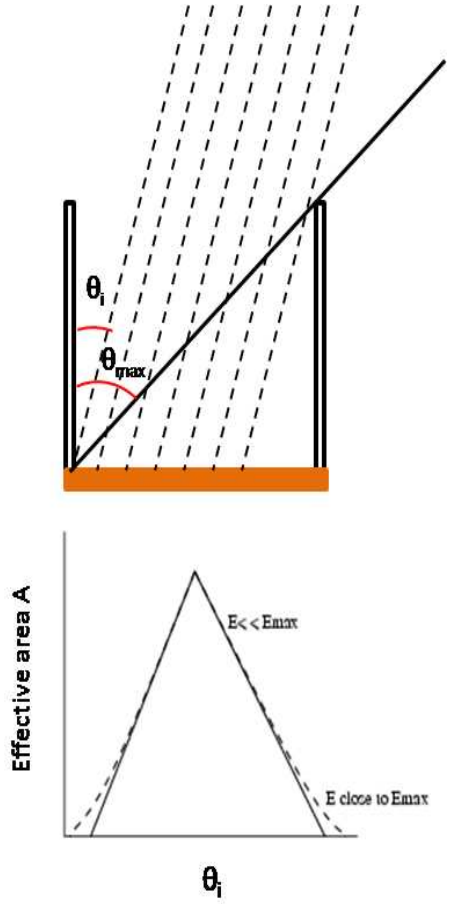

FIGURE 3.4: Collimator response: Dotted line in the figure below indicate that the transmission does not fall abruptly to zero for higher energies

where R (I,E) gives the probability that a photon of energy E is registered as a signal M (I) in channel I. This is essentially the energy dependent SRF. A(E) is the effective area and S(E) the incident spectrum. In discrete form,

$$M_i = \sum_j R_{ij}(I,E)A_j(E)S_j(E) \tag{3.12}$$

Ideally, we should be able to calculate the source spectrum from this equation by inverting the matrix R_{ij}. But solutions are then very sensitive to M (I) and often this method results in amplification of the noise. Hence a forward fitting approach is used for spectral analysis where a model spectrum is generated with an initial guess, convolved with the instrument response and is compared to the observed data. The best model that fits the data can then be found using any of the statistical tests for fitting.

XSPEC [Arnaud, 1996] developed by HEASARC is such an x-ray spectral analysis package where we load the instrument response matrix and effective area in the form of matrices in a specified format. The response matrix generated in this work follows the OGIP format [George et al, 1998] for compatibility with spectral analysis in XSPEC.

3.3 Calibration measurements

3.3.1 The RESIK x-ray beam facility

The RESIK x-ray beam facility (hereafter referred to as RESIK) at the Rutherford Appleton laboratory, UK, uses an x-ray generator with replaceable targets to generate specific x-ray fluorescence lines together with a continuum bremsstrahlung spectrum. This facility provides an x-ray beam-line ($\sim$ 3.7 m) in vacuum, with multistage collimation to produce a nearly parallel beam. The size of the slits can be varied, thus varying the size of the x-ray beam entering the vacuum chamber. There is a cryosystem for cooling the detectors to derive detector performance parameters over a range of temperatures. Two translation stages with movement in two orthogonal directions and a rotation stage are built into the vacuum chamber where the detector is placed. The stages are controlled remotely through a graphical interface from a computer.

A tungsten filament in the x-ray tube serves as the cathode which when heated, generates electrons which are accelerated toward the anode because of the applied high voltage. When these electrons strike the anode, characteristic x-rays are generated together with a thick-target bremsstrahlung continuum. The electrons striking the anode can accelerate to a maximum energy equal to e $\times$ applied high voltage (applying a high voltage of 15 kV would accelerate the electrons to a maximum energy of 15 keV). The characteristic lines from the target can be excited only if the kinetic energy of the electrons is higher than the binding energy of the anode material.

Prior to flight calibration, it was necessary to arrive at the anodes to be used in the x-ray tube. RESIK measurements revealed concerns about using anodes with powder-filled holes . Table 3.1 gives the list of chosen anodes and characteristic x-ray lines they generate.

RESIK also provides the capability to select narrow energy range beams using a double crystal, suitably oriented using translation and rotational stages. The available double

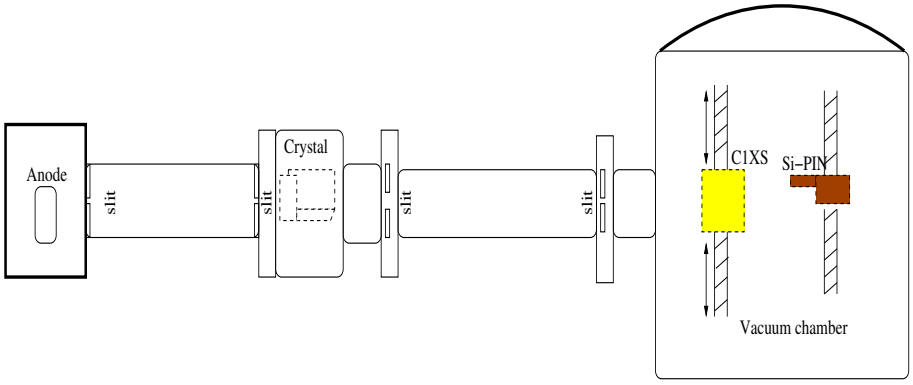

FIGURE 3.5: Schematic diagram of the C1XS ground calibration set up

TABLE 3.1: Line energies used for calibration at RESIK

Anode	**Cu**	**Al**	**Mg-Cu**	**Mo**	**Ti**	**Cr**	**Co**
Energy (keV)	0.93, 8.05, 8.90	1.48	0.93, 1.25, 8.05, 8.90	2.29	4.51	5.41	6.93

crystal (quartz) could only operate above 2 keV and hence monochromatic spectrum could be obtained only above this energy.

3.3.2 Characterization of the x-ray beam

The x-ray beam incident on the SCDs is the primary source of calibration of the detectors. Hence it was necessary to fully characterize the x-ray beam and arrive at the optimum high voltage and current that should be applied. Characteristic x-rays are emitted from the anode only if high voltage is enough to produce electrons with an energy higher than the ionization potential of the target atoms. Increasing the current, increases the number of electrons and thus the beam intensity. Two beam configurations were adopted for the calibration (Figure 3.6) .

- Wide beam ($\sim$ 2 cm x 4 cm) : A wide beam which would fully illuminate the SCDs
- Narrow beam ($\sim$ 0.1cm x 0.2 cm): A narrow beam fully contained within the Si-PIN reference detector and SCDs

Calibration requirements demanded the x-ray beam incident on the detector to be stable in time. Also the beam intensity had to be spatially uniform across the width of the

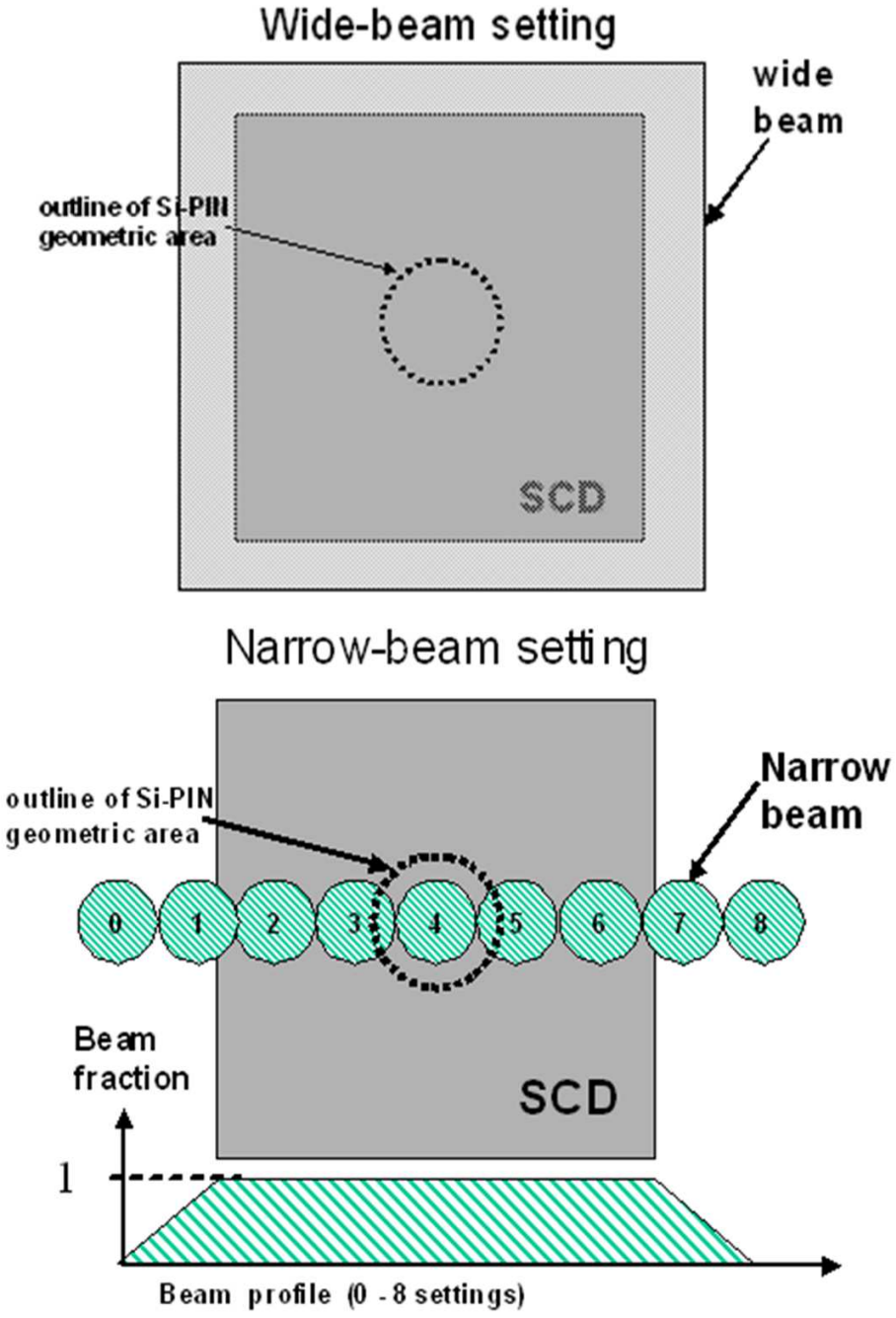

FIGURE 3.6: Beam configurations for calibration.

beam. It was also essential to tune the high voltage and current settings of the x-ray generator to avoid pile up and at the same time have a count rate high enough to produce statistically significant spectral line flux. Very low current settings often lead to temporal fluctuations in the beam intensity in x-ray generators. Hence a set of measurements were done to study the temporal and spatial uniformity of the x-ray beam with a given target for an optimal beam setting.

The beam was found to be spatially uniform within 2% for a 2 cm x 2 cm area of the incident beam. For a duration of 1 hour, the beam was stable in time within 1.2%. The lowest stable current setting for the beam was 0.5 mA which still showed pile up effects in the wide beam configuration. Hence aluminum filters were used to cut down the beam intensity for the wide beam configuration.

3.3.3 Measurements

Prior to the calibration measurements at RESIK, a Si-PIN detector was calibrated at the electron storage ring at PTB/BESSY II to use it as a reference for the C1XS SCDs. The C1XS SCDs then went through a detailed calibration at RESIK with the following objectives.

- Calibration of electronic channel versus incident x-ray energy for a range of operating temperatures.
- Determination of energy resolution of SCDs as a function of incident x-ray energy as well as its dependence on temperature.
- Determination of collimator response.
- Determination of SCD spectral re-distribution function.
- Modeling the SRF as a function of energy and temperature.
- Experimental determination of low energy threshold.
- Determination of detector background for various temperature settings.
- Determination of detection efficiency of the detectors relative to a calibrated reference detector.
- Determination of absolute detection efficiency of SCD.

TABLE 3.2: Summary of the calibration measurements

Anode	**Energy (keV)**	**Al filter**	**Crystal**	**Data type**	**Temperature (°C)**
Mo	2.29	No filter	Yes	12	-27,-22.5,-15,-7.5,0.0
Ti	4.51	20 μm	Yes	12	-30, -22.5, -15, -7.5
Cr	5.41	No filter	Yes	12	-30, -22.5, -15, -7.5
Co	6.93	20 μm	Yes	12	-30, -22.5, -15, -7.5
Cu	8.05	No filter	Yes	12	-30, -22.5, -15, -7.5
Al	1.49	No filter	Beam passing through the crystal leaves	12	-30, -27.5,-25,.-10
Cu	8.05	No filter	Yes	10,11,12	-10
Cu	8.05	No filter	Beam passing through the crystal leaves	10,11,12	-20
Mo	7-10	200 μm	No	12	-20 (SCD centered)
Cu	7-10	200 μm	No	12	-20 (SCD centered)
Mg-Cu	1-10	No filter	No	12	-20
Al	1.49	No filter	No	12	-20(SCD centered)

- Determination of pileup effects in SCD.
- Determination of the complete detector response for various operating temperatures.

To determine the SRF of the SCDs, measurements were done with a double crystal (quartz) in the beam-line. The crystal was efficient only above 2 keV and hence the SRF could be determined only above 2 keV. The measurements were done at various operating temperatures ranging from -30°C to 0°C. A corresponding measurement was done with the reference detector for every SCD measurement. A summary of the measurements done is given in table 3.2. The beam current was kept at 5 mA and high voltage at 15 kV for all crystal measurements. The event rate was maintained below the level where pile up effects become observable.

C1XS had two types of event selection as described in chapter 2, resulting in three types of data packets. Most of the measurements were done in a mode where events below threshold on either side of the main event are discarded (Type 10 and 12 data packets).

3.3.4 Analysis approach

The various steps in the overall approach we have adopted for calibration data analysis is shown in Figure 4.3. Spectral fits to derive the SRF used a routine 'mpfit' (http://cow.physics.wisc.edu/~craigm/idl/idl.html) which uses Levenberg Marquardt least-squares fitting method. All the necessary codes were written in IDL (Interactive Data Language).

3.4 Radiometric calibration of the Si-PIN reference detector

3.4.1 Experimental setup

A Si-PIN detector was used as a transfer standard, relative to which the SCDs were calibrated. The Si-PIN x-ray detector, supplied by AMPTEK (XR-100CR) comes with a pre-amplifier and an inbuilt peltier cooler. The hermetic TO-8 package of the detector has a light-tight, thin Beryllium window (12.5 μm) and 500 μm depth in silicon for x-ray interaction .

The x-ray beam-lines at the electron storage ring at BESSY II is an established radiometric standard for calibration of x-ray detectors. Two monochromator-equipped beamlines; SX700 (plane-grating monochromator) and FCM (four-crystal monochromator) [Thornagel et al, 2001] were used for the calibration measurements. SX700 extends from 100 eV to 1.8 keV and FCM beam-line from 1.8 keV to 10 keV. Across the energy range from 600 eV to 1.9 keV, measurements were taken every 100 eV. At higher energies (2 to 10 keV), measurements were carried out at 1 keV steps. Near the silicon absorption edge, finer measurements in steps of 1 eV were obtained.

The primary objective of the measurements was to derive the detection efficiency of the Si-PIN detector relative to the calibrated Si(Li) detector of PTB over the 1-10 keV range. Monochromatic spectra from the synchrotron beam-lines enabled modeling of SRF at energies from 0.6 keV to 10 keV. SRF is a function of energy , event rate as well as temperature. Here we have modeled the SRF at a given temperature and event rate. Since the aim was to create a transfer standard and the temperature of the Si-PIN is maintained stable at 230°K by the internal thermo electric cooler, we did not attempt to study the dependence of the SRF with temperature. Measurements were taken at

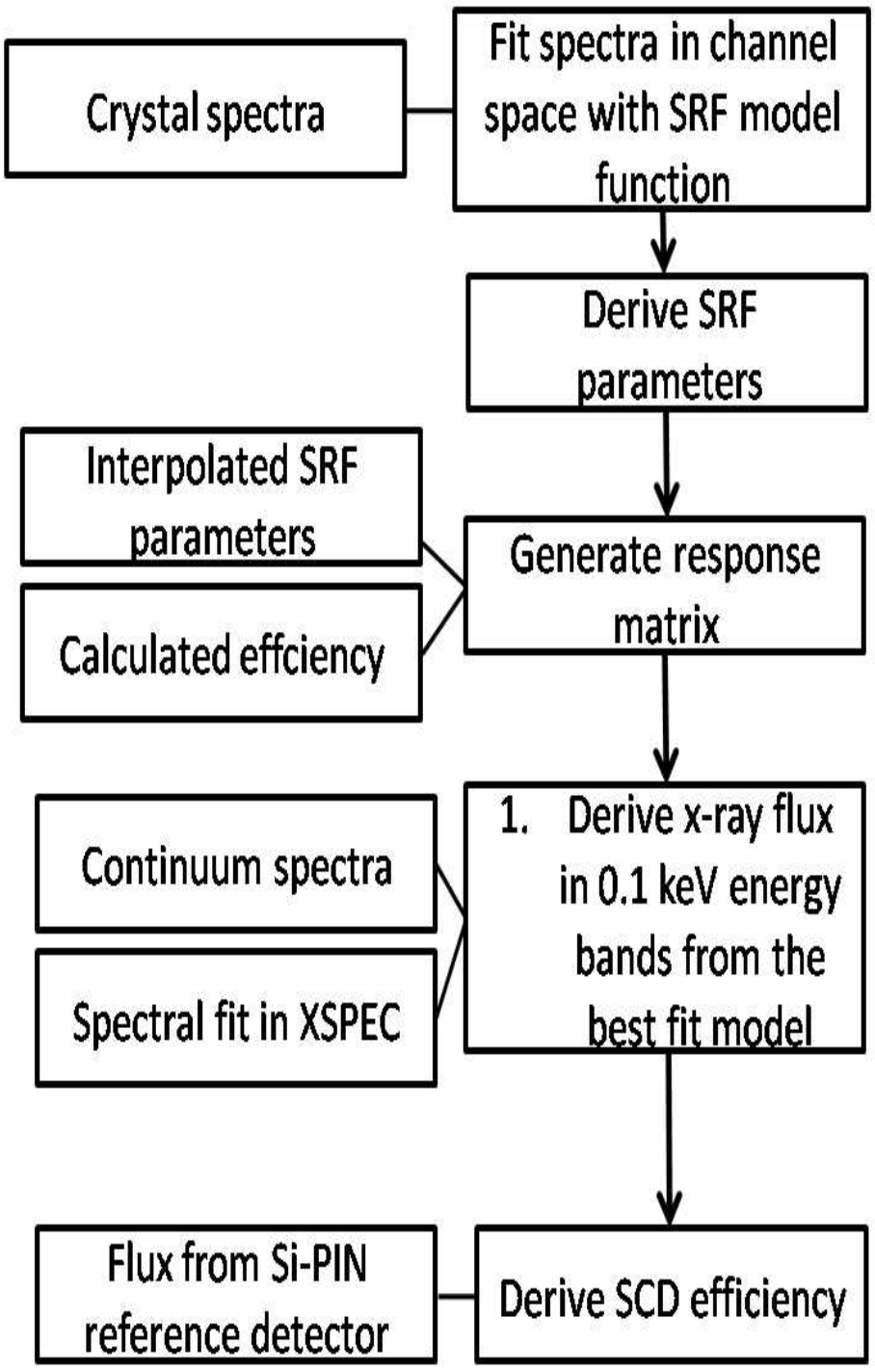

FIGURE 3.7: Steps involved in C1XS calibration data analysis

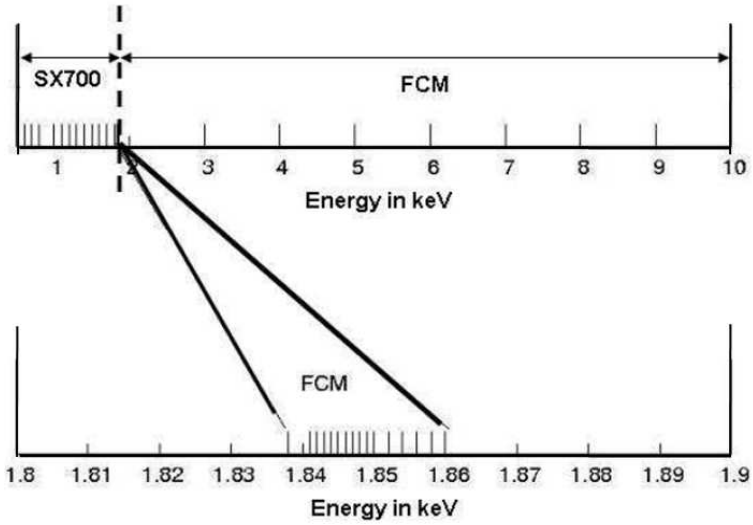

FIGURE 3.8: Drawing shows beam energies at which Si-PIN detector has been calibrated

different event rates to ensure that the beam intensity used for calibration does not produce pile up.

Both the Si-PIN and the reference Si(Li) detector sampled the same incident beam. Si(Li) detector measured the flux from the monochromatic beam before and after each Si-PIN measurement. The Si-PIN detector was moved in and out of the beam for this purpose. The beam current was monitored and showed a typical fluctuation of 1-2%. The beam-size was measured to be 1.09 mm x 0.7 mm (private communication, PTB) which is narrower than the Si-PIN geometric area. Hence the beam was fully contained within the Si-PIN detector.

3.4.2 Si-PIN spectral redistribution function

The spectra from the monochromator beam were used to model the spectral redistribution function (SRF) of the Si-PIN detector. The model was developed using IDL to implement the HYPERMET function [Philips and Marlow, 1976] with additional terms to account for features above the photopeak. Spectral fits were obtained using the routine 'mpfit' which we implemented in our IDL code.

$$\text{SRF} = \text{photo peak} + \text{low energy tail} + \text{low energy shelf} + \text{escape peak}$$

$$SRF = S_1 e^{\frac{-(E-E_0)^2}{2\sigma_0^2}} + 0.5 S_2 e^{\frac{(E-E_0)}{\beta_1}} \times erfc(\frac{E-E_0}{\sqrt{2}\sigma_0} + \frac{\sqrt{2}\sigma_0}{2\beta_1}) + 0.5 S_3 erfc(\frac{E-E_0}{\sqrt{2}\sigma_0}) + S_4 e^{\frac{-(E-E_1)^2}{2\sigma_1^2}} \quad (3.13)$$

where E_0 is the centroid channel of the Gaussian fit to the photo peak and E_1 that of the escape peak. σ_0 is the width of the Gaussian photopeak and σ_1 that of the escape peak. β_1 is the slope of the low energy tail and S_1, S_2, S_3, S_4 are the normalization factors.

In addition, we see features above the energy of the photopeak in the spectra. This has also been modeled in our analysis though not included as part of SRF (Figure 3.9).

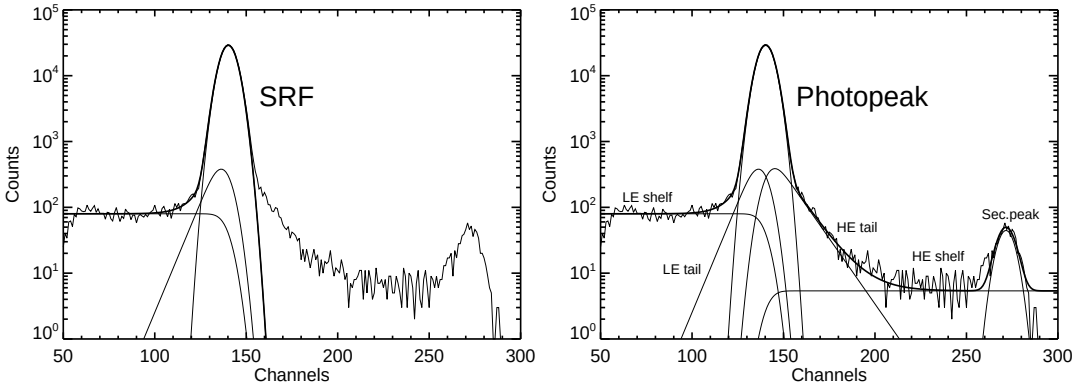

FIGURE 3.9: The total pulse height spectrum for a monochromatic beam (1.5 keV) is shown (bold) along with the individual contributing components (left) and the SRF is shown on the right. The escape peak would be visible only when the incident x-ray energy is greater than the K-shell electron binding energy in silicon (1.84 keV)

The features above the photopeak are modeled as a high energy tail, high energy shelf and a secondary peak (which together is referred to as the high energy component here). Thus the total observed spectrum is modeled as

Total pulse height spectrum = SRF + HE component
HE component= HE tail + HE shelf + Secondary peak

$$HE\ component = 0.5 S_5 e^{\frac{-(E-E_0)}{\beta_2}} \times erfc(\frac{-(E-E_0)}{\sqrt{2}\sigma_0} + \frac{\sqrt{2}\sigma_0}{2\beta_2}) + 0.5 S_6 erfc(\frac{-(E-E_0)}{\sqrt{2}\sigma_0}) + S_7 e^{(\frac{-(E-E_2)^2}{2\sigma_2^2}} \quad (3.14)$$

Here, σ_2 is the width of the Gaussian peak in the HE component.

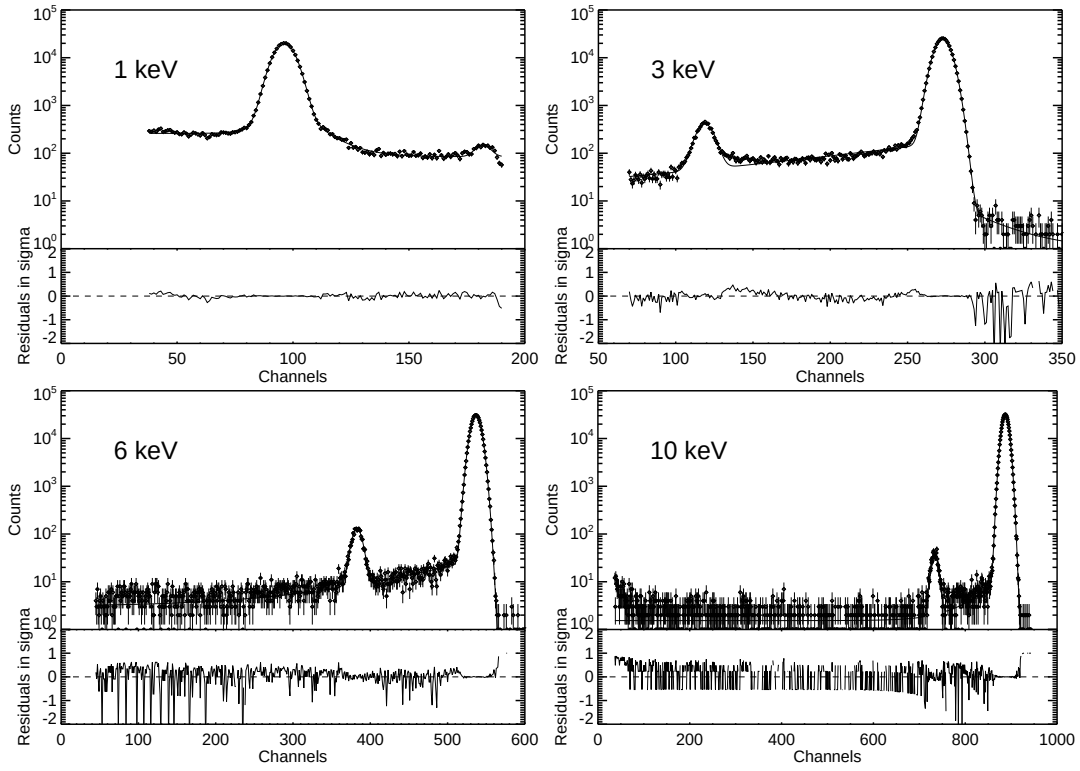

FIGURE 3.10: Si-PIN Spectral fits at 1 keV, 3 keV, 6 keV and 10 keV with residuals

The above mathematical formulation of the pulse height distribution was used to model the observed spectra and derive the SRF as a function of energy from 0.6 to 10 keV.

Figure 3.10 shows the overall fit to the observed spectra. Shown alongside are the residuals (in σ) which indicate excellent fits throughout the spectral range. The strength of the low energy tail and shelf features as a fraction of counts under the photopeak is shown in Figure 3.11 and Figure 3.12. The contribution from these features together reaches 30% at the silicon absorption edge. At higher energies, the strength of the low energy components decrease, consistent with the model where the low energy components arise from partial absorption in the upper dead layer of the detector (higher energy photons travel deeper into the detector before interaction). The high energy component cannot be a part of the SRF (as the the incident x-ray photons cannot redistribute pulses with an energy greater than their own), but are probably due to pile up and the second harmonic in the primary beam (which appears as the secondary peak).

The dependence of the FWHM of the photopeak on energy is shown in Figure 3.13. The best fit to the curve in Figure 3.13 provides r= 12.31 $\pm$ 0.67 electrons and F= 0.12 $\pm$ 0.03, consistent with similar estimates in silicon detectors [Owens et al, 1996].

The features above the photopeak consist of a high energy tail, high energy shelf and a secondary peak at twice the energy of the photopeak. The secondary peak is interpreted as the harmonic of the primary beam (mean energy $\approx$ 2 x photopeak energy).

The origin of the observed high energy component cannot be attributed only to pile up. Spectral measurements at two count rates (500 cts/s and 3000 cts/s) show that the strength of the HE component (Table 3.3), relative to the contribution from SRF, decreases at higher count rates. If the component is due to pile up, it is expected to increase at higher counting rates. Figure 3.14 shows the Si(Li) spectrum and Si-PIN spectrum at 1.5 keV. The Si-PIN has a pile up rejection circuitry where, if two events occur with a time delay greater than 400 ns, both are rejected. The low energy threshold of the fast channel is 0.4 keV. Hence pile up can occur only when a pulse belonging to the incident photon energy overlaps with a pulse less than 0.4 keV. But the high energy features extend beyond peak energy + 0.4 keV (37 channels from the photopeak).

Though, we have not been able to clearly pinpoint the origin of this high energy component, this has no impact on the determination of the SRF of the reference detector,

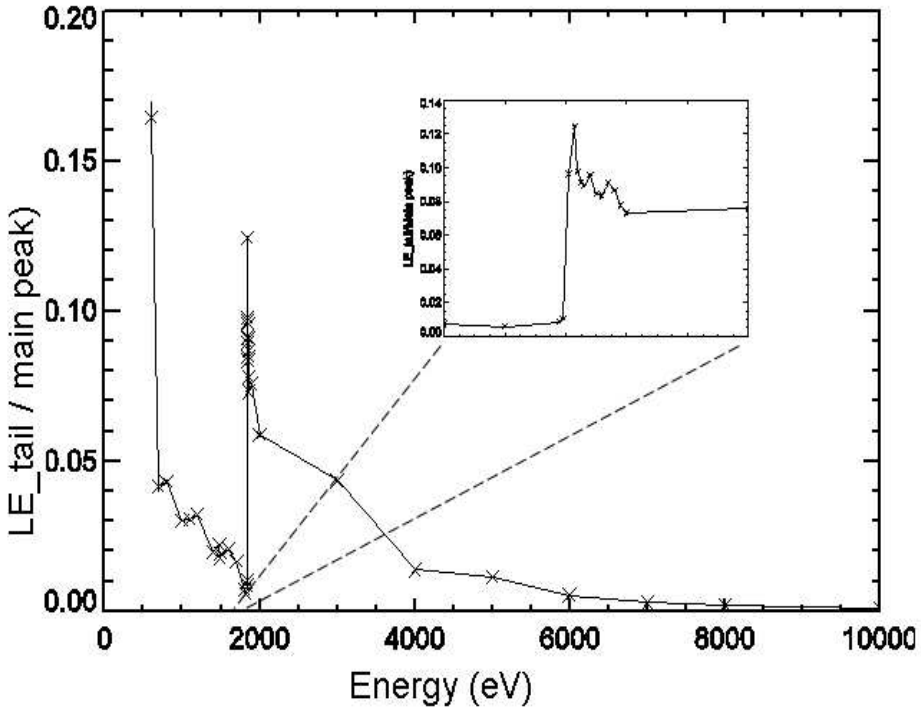

FIGURE 3.11: Fraction of events in the low energy tail component of the Si-PIN as a function of energy

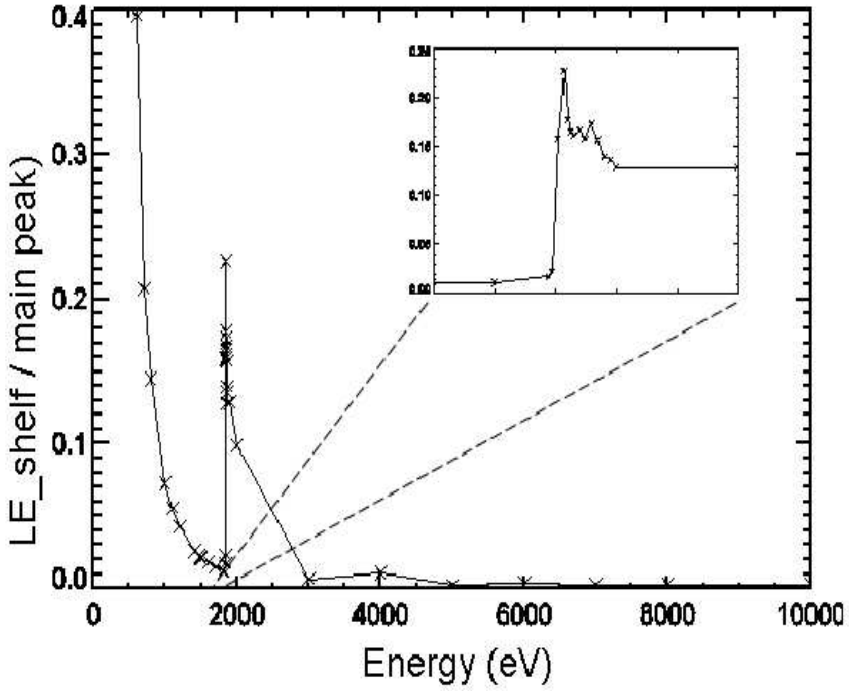

FIGURE 3.12: Fraction of events in the low energy shelf component of the Si-PIN as a function of energy

TABLE 3.3: Percentage of counts in the HE components relative to that under SRF at two different count rates

Energy in keV	**500 cts/s**	**3000 cts/s**
1	19 %	8%
1.2	24%	7.5%
1.4	17%	4%
1.6	20.5%	5.37%
1.8	4.2%	0.24%

which does not include the high energy components (redistribution of the photons as discussed in section 3.1 will not result in higher energy components).

Thus the mathematical formulations used to model the observed spectral distribution are well suited to explain all the observed features of the Si-PIN pulse height distribution.

3.4.3 Detection efficiency of the Si-PIN

The Si(Li) reference detector at PTB measures the beam-line flux before and after every Si-PIN measurement. The beam current is also monitored throughout the experiment.

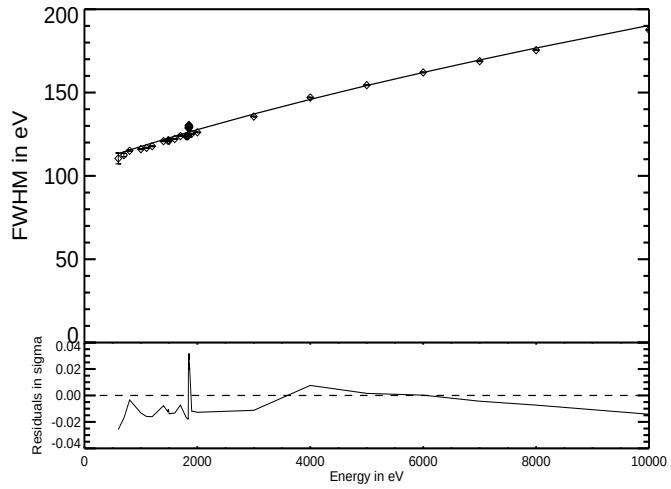

FIGURE 3.13: Si-PIN FWHM as a function of energy; (F=0.12 ±0.03 and r=12.31±0.67 e$^-$)

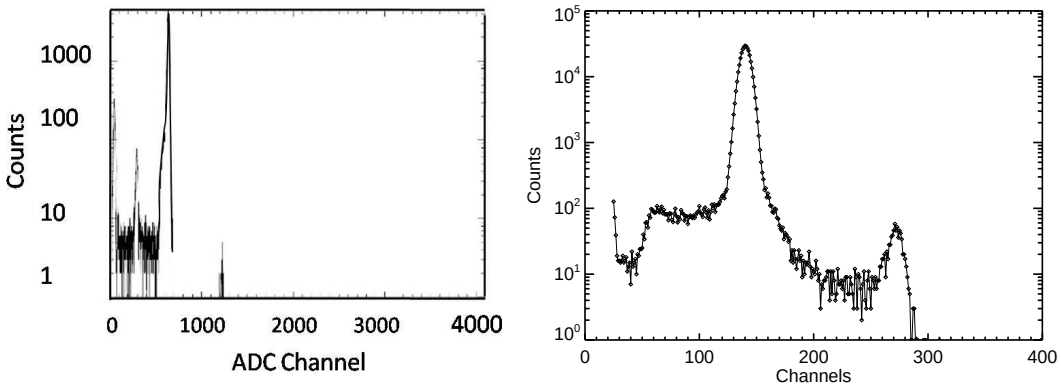

FIGURE 3.14: Si(Li) spectrum (left) and Si-PIN spectrum (right) at 1.5 keV showing the HE component (channels 200 - 250) only in the Si-PIN detector.

The detection efficiency of the Si-PIN detector at energy E is derived as

$$Q(E) = \frac{Counts_{Si-PIN}}{Counts_{Si(Li)}(cts/mA)} \times \frac{Efficiency_{Si(Li)}}{I_{beam}} \tag{3.15}$$

Where $Q(E)$ is the detection efficiency of the Si-PIN at energy E and I_{beam} is the beam current in mA at the time of Si-PIN measurement. The high energy component described earlier does not affect the determination of detection efficiency, because the counts in the photopeak derived by fitting with the SRF has been used in equation 8.

The uncertainty on the beam current [Thornagel et al, 2001] measured is taken as

$$dI_{beam} = 1\mu A + 10^{-4} I_{beam} \tag{3.16}$$

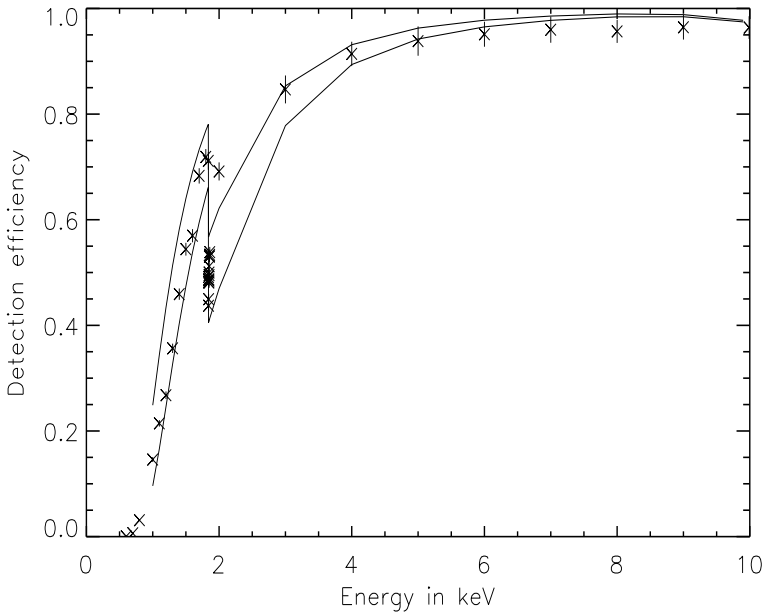

FIGURE 3.15: Detection efficiency derived w.r.t the Si(Li) detector at PTB. The lines show the derived upper and lower limits on the model.

A physical model consisting of 500 μm depletion layer of Si for x-ray absorption, SiO_2 dead layer and Be window of a certain thickness can be used to model the observed detection efficiency curve. We have computed models by varying the Be window thickness from 2 μm to 18 μm and the SiO_2 thickness from 0.5 μm to 2 μm. Deviation from the observed values has been quantified in terms of chi-square statistics. Figure 3.16 shows the contour of chi-square values. 1-σ confidence limits have been derived on the values for window thickness as 7.5-13.3 μm and 0.9-1.4 μm for the dead layer from this contour of chi square values. An earlier measurement of a similar Si-PIN detector gives a value of 4.2-6.5 μm [Turany et al, 1999] for the dead layer in comparison to the upper limit of 1.4 μm that we have estimated. The depletion depth thickness cannot be verified experimentally because of the limited energy range of this calibration exercise.

3.5 SCD calibration

3.5.1 SCD spectral redistribution function

The monochromatic spectra from measurements using the crystal in the RESIK beamline were fitted with a model consisting of 6 components.

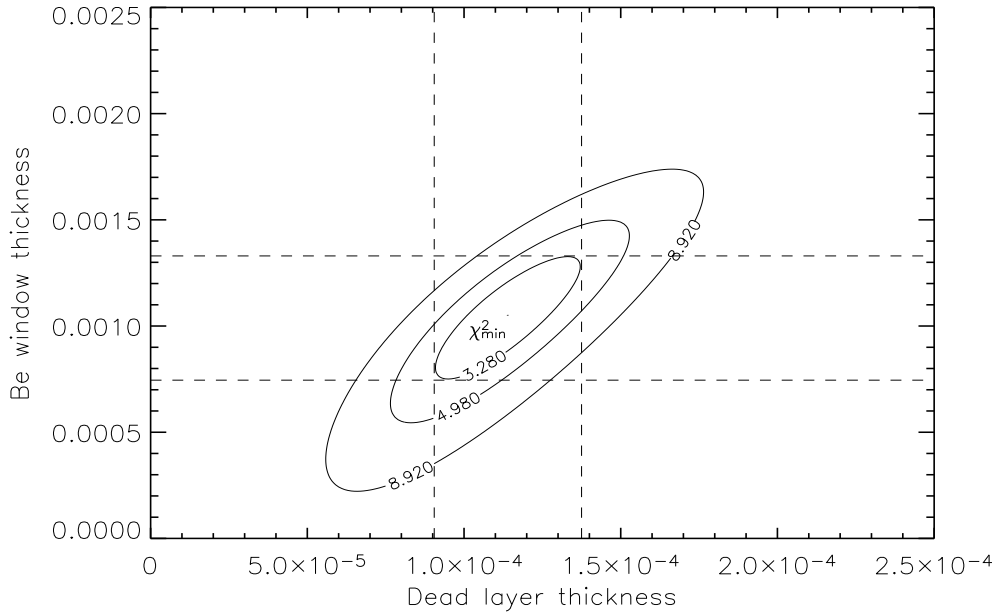

FIGURE 3.16: Confidence regions in χ^2space: 1σ (3.28), 2σ (4.98), 3σ (8.92) contours are shown. The thicknesses are expressed in cm

$$\begin{aligned}\text{SRF} = {} & \text{photo peak} + \text{low energy tail} + \text{low energy shelf} + \text{split events} \\ & + \text{escape peak} + \text{low peak}\end{aligned}$$

The split event component was mathematically modeled as an exponential convolved with a Gaussian function. A Gaussian peak just below the photopeak and a cut off of the low energy shelf component $\sim$ 0.8 keV below the photopeak, was added to accurately model the SRF. The channel at which the low energy shelf component is cut off, was left as a free parameter. Figure 3.18 shows that the cutoff channel is nearly a constant at all energies. The cut off at 0.8 keV is caused by the event selection algorithm implemented in C1XS. The individual components in the model are shown in Figure 3.19 and spectral fits in Figure 3.17. There are altogether 18 parameters and all the best fit models have a reduced chisquare between 0.8 and 1.5.

The fraction of events outside the photopeak increases with energy as shown in Figure 3.20. The SCD low energy components do not follow the energy dependence that the reference detectors had. The reference detector shows a typical dependence seen in silicon detectors where contribution to the low energy tail and shelf is maximum just above the silicon absorption edge and thereafter decreases. In SCDs, the primary component of the off-peak events is split events and they drive the energy dependence. At higher energies, the x-ray photons have to drift longer in the electric field which makes the charge cloud bigger increasing its probability to spread across pixels.

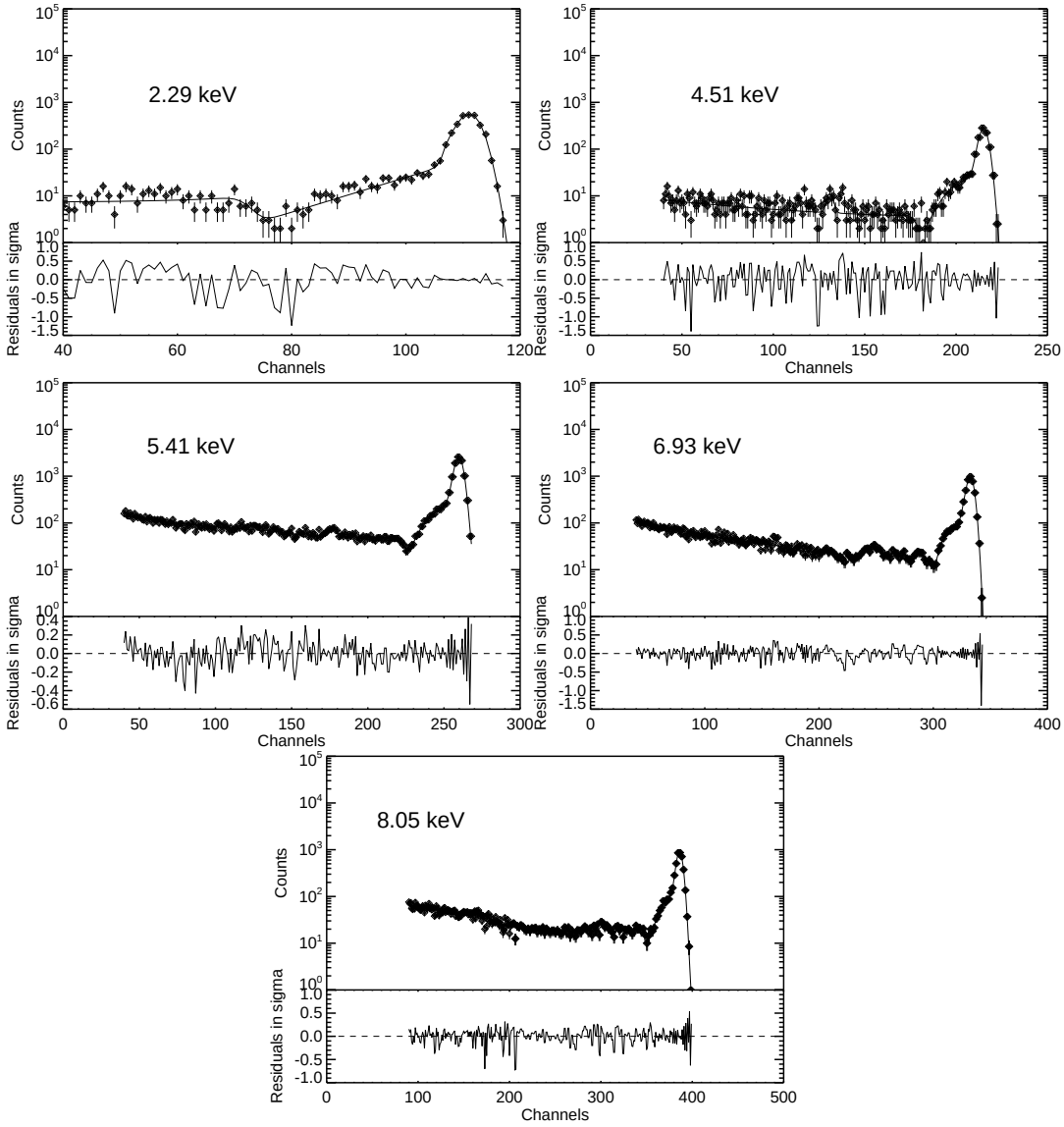

FIGURE 3.17: SCD spectral fits

As shown in Figure 3.21, the SCD gain is linear throughout the energy range of interest. The 24 SCDs have a range of gains from 4.8 eV/channel to 6.9 eV/channel. From a measurement of the FWHM as a function of energy, we derive the Fano factor as 0.11 $\pm$ 0.02 and noise as 6.1 $\pm$ 1.6 electrons.

To understand the dependency of the SRF on detector temperature, measurements with the Cu anode (energy 8.05 keV) were done every 2.5°C. Figure 3.22 shows that the fraction of off-peak events is fairly insensitive to temperature variations. However, the FWHM and gain do vary with temperature and hence the response has to be generated for the required operating temperature.

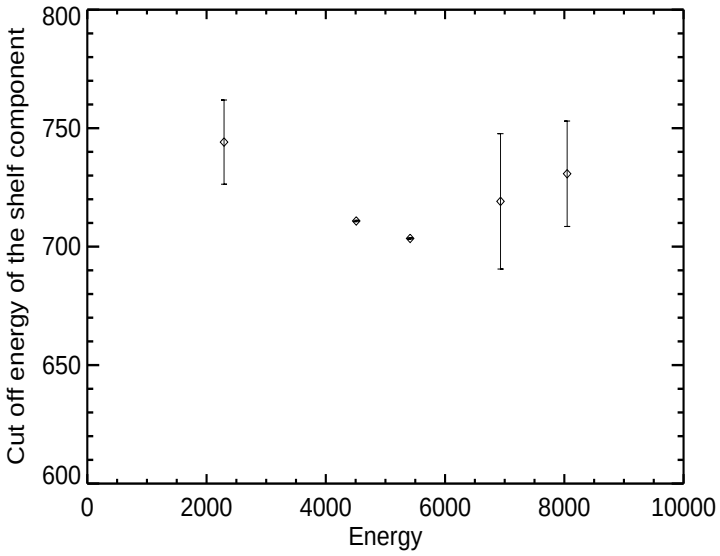

FIGURE 3.18: Distribution of cutoff energies of the low-shelf component

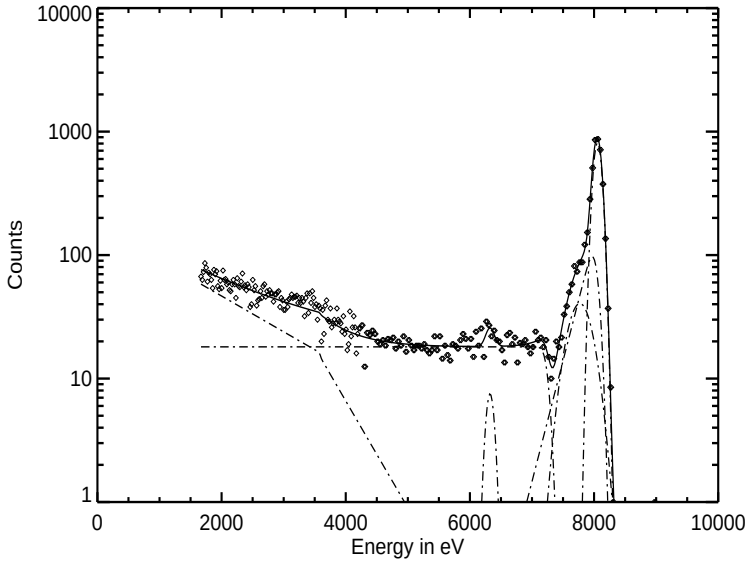

FIGURE 3.19: The components of the SRF at energy = 8 keV. The solid line shows the sum of the components (dotted lines)

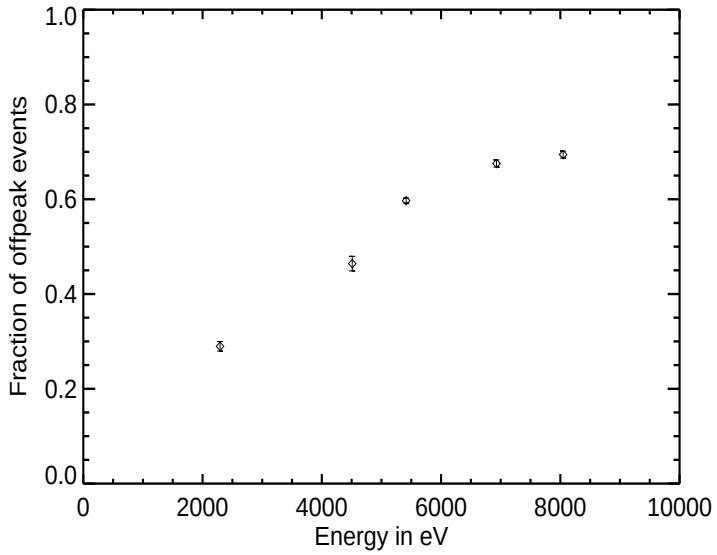

FIGURE 3.20: Off peak component strength as a function of energy

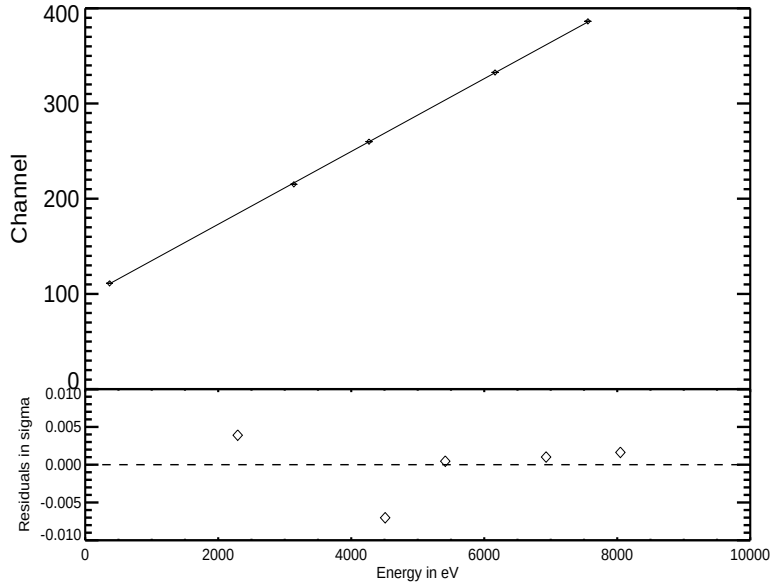

FIGURE 3.21: Linearity in energy-channel conversion

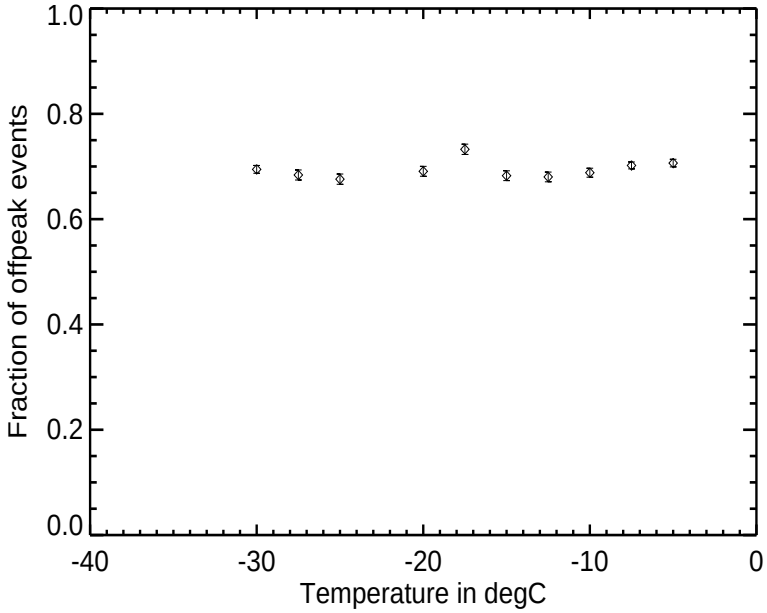

FIGURE 3.22: Temperature dependence of off-peak events. Data does not indicate any clear dependence

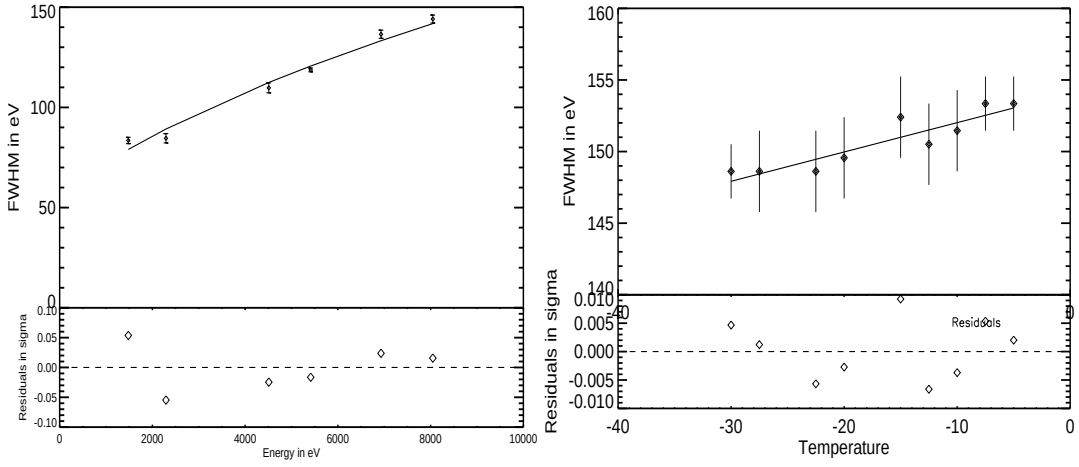

FIGURE 3.23: (Left) SCD FWHM as a function of energy: (F=0.11 ±0.02, r= 6.5±1.6). (Right) Temperature dependence of FWHM (at 8 keV). Measured gradient = 4.88 ± 0.64 eV/°C

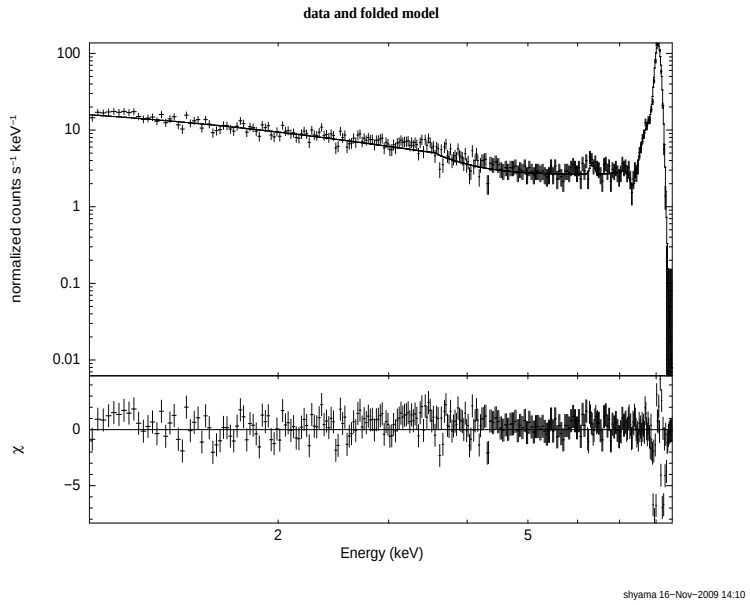

FIGURE 3.24: Spectral fit to the mono-energetic crystal spectrum at 8.05 keV with the Cu anode

3.5.2 SCD detection efficiency

Using the beam configurations described in sub section 3.2.2, measurements were made with the beam centered on each SCD to determine the detector efficiency from 1-10 keV. These comprised a wide beam measurement using both a Cu-anode and Mg-anode and a narrow beam measurement using the Al-anode. To avoid pile up, the Cu wide beam spectrum was taken with a 200 μm Al filter and hence this spectrum is useful only in the 5-10 keV range. The Mg-Cu anode enabled measurements from 0.9-10 keV range.

A response matrix was generated using the derived SRF and a calculated detection efficiency ($\epsilon_{calculated}$). The calculated detection efficiency is based on the absorption in the different layers of the device and assuming a depletion depth of 42 μm [Gow, 2009]. The crystal spectra were first fitted using this response matrix for validation (Figure 3.24). Then the spectra required to derive efficiency were fitted using this response matrix.

The continuum spectra were modeled as a thick-target bremsstrahlung given by the simple form of Kramer's formula (assuming that effects of self absorption in the target and backscattering of the incident electrons are not significant)

$$N(E) = I \times Z \times \frac{(V - E)}{E} \tag{3.17}$$

where, I is the current in A, Z is the atomic number of the anode material, V the voltage in V and E energy in keV.

Flux (Flux$_{SCD}$) in narrow energy bands (0.1 keV) were obtained from the best fit model to the spectrum in the SCD. The same spectrum was also measured using the reference detector. The x-ray flux in 0.1 keV bands (Flux$_{Si-PIN}$) were derived for the Si-PIN as well from spectral fits with the same model. Spectral fits to the SCD continuum beam using the thick-target bremsstrahlung model is shown in Figure 3.25.

The detection efficiency of the SCD (ϵ_{SCD} (E)) was calculated from the Cu and Mg-Cu anode continuum spectra and the Al-spot measurement as follows and is plotted in Figure 3.26.

$$\epsilon_{SCD}(E) = \frac{Flux_{Si-PIN}}{Flux_{SCD}} \times \epsilon_{calculated} \tag{3.18}$$

The derived detection efficiency (dotted curve in Figure 3.26) values are $\sim$ 68% of the calculated curve. The x-ray events on-board are filtered based on two thresholds. Out of every 3 pixels in the read out chain, an event is selected only if the central pixel is above threshold 1 and the pixels on either sides are below threshold 2 (Figure 3.27). The event is discarded if either of the adjacent pixels are above threshold 2. This event selection criteria was implemented in order to minimise the incidence of split events in the spectra but results in a reduced detection efficiency as many x-ray events are discarded.

3.6 On-board calibration using radioactive sources

To allow the SCD to be routinely calibrated during the mission, C1XS carried 24 Fe-55 radioactive isotopes attached to the inside of aluminum door which, when closed, allowed each source to illuminate a single SCD. The door also served as a protection for the SCDs as the spacecraft passed through Earth's radiation belts *en route* to the Moon.

The Fe-55 sources also had a thin titanium foil in front of them thus providing calibration lines at four energies - 4.5 keV (Ti-K$_\alpha$), 4.9 keV (Ti-K$_\beta$), 5.9 keV (Mn-K$_\alpha$) and 6.4 keV (Mn-K$_\beta$). The FWHM of the devices increased from 153 eV before launch to 163 eV at 5.9 keV at -8 °C in lunar orbit. A degradation in energy resolution due to radiation damage in the Earth's radiation belts (even when the door is closed) is expected as shown by proton irradiation tests on ground [Smith et al, 2009]. The response matrix was regenerated with the revised energy resolution. Figure 3.28 shows the on-board

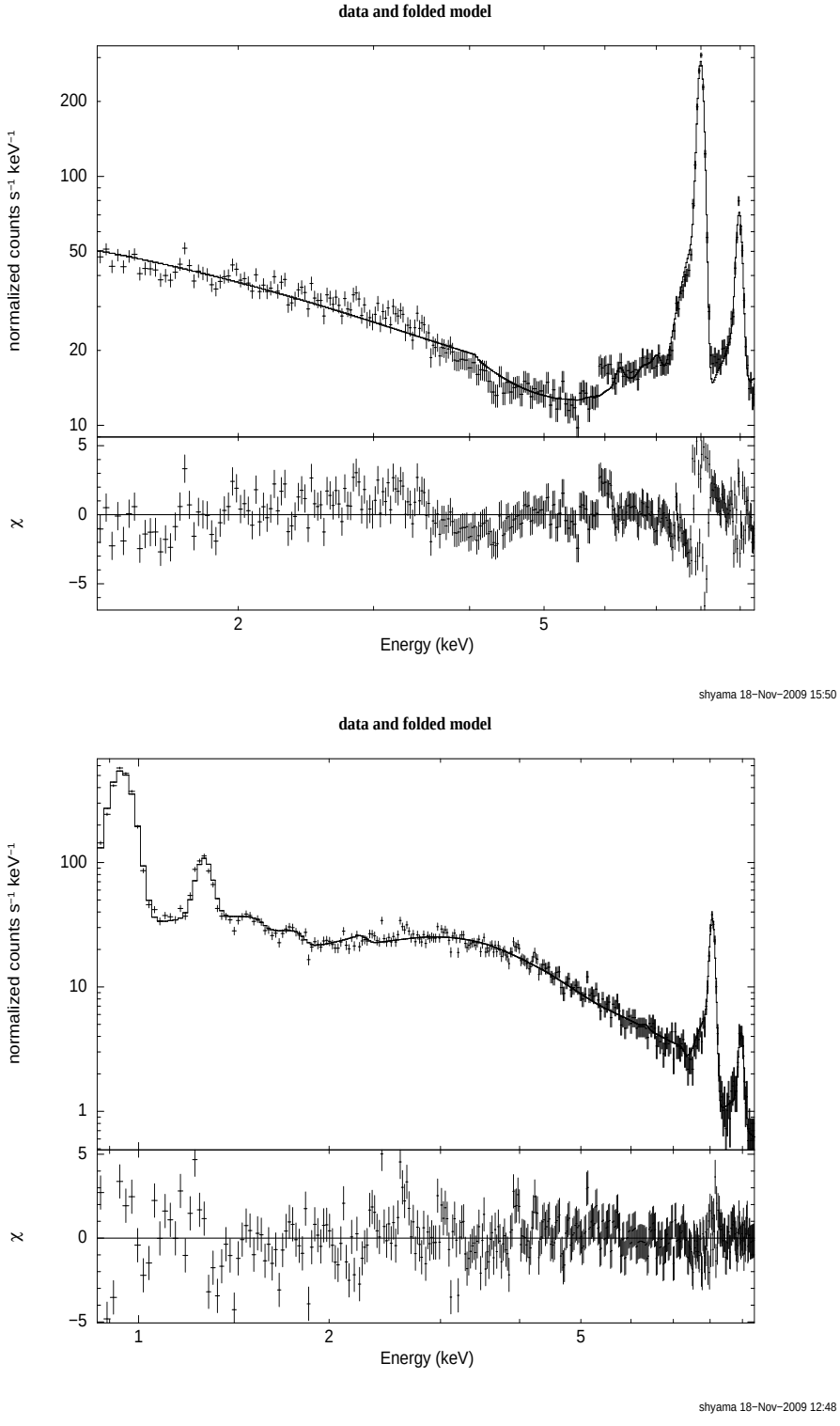

FIGURE 3.25: Spectral fit to the wide beam continuum spectra (Cu on top and Mg-Cu at the bottom) from which SCD detection efficiency was determined

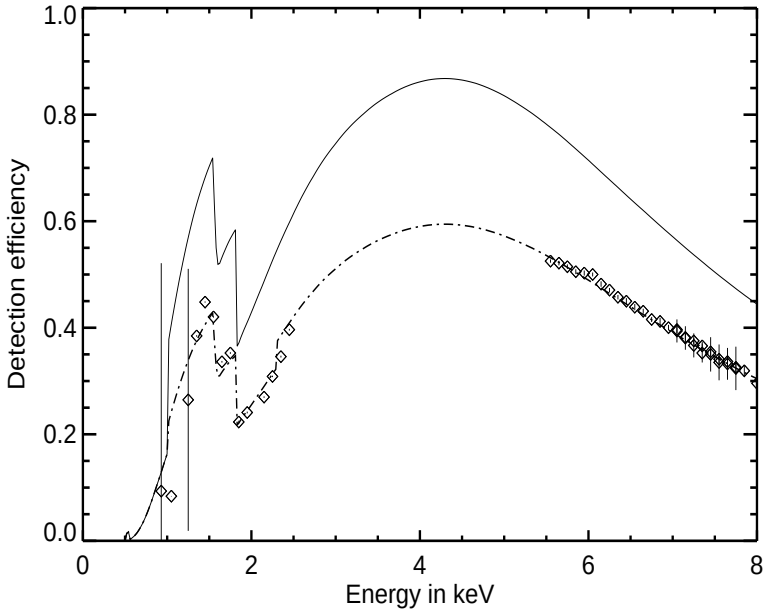

FIGURE 3.26: Detector efficiency. Calculated curve (solid line). The points are the detection efficiencies obtained in comparison to the reference detector. The dashed line represents the nominal efficiency for lunar data analysis. The reduction in efficiency is believed to arise from event selection criteria implemented in the hardware.

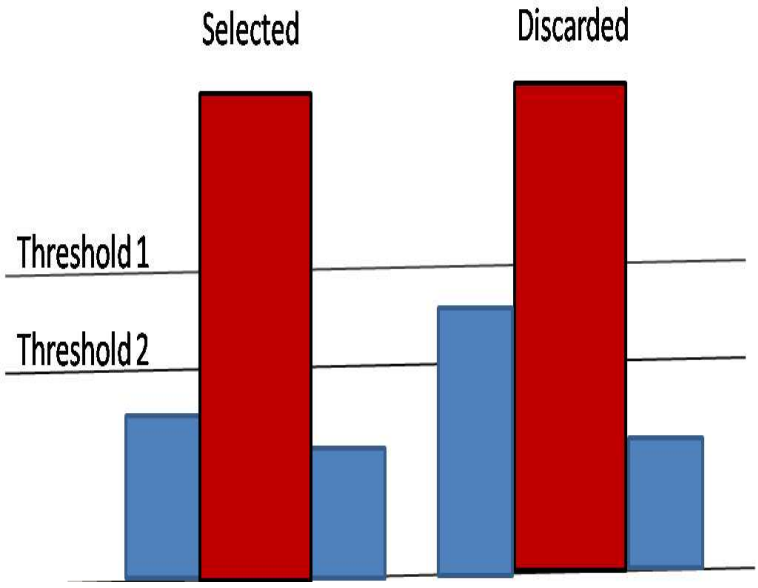

FIGURE 3.27: Event selection criteria implemented in C1XS (Type 10)

Fe-55 spectrum fitted with a Gaussian for the lines and a power law function for the continuum using the regenerated response matrix. Even though the door was closed there is a continuum background in the detector not observed on ground possibly arising from the enhanced particle interactions in the vicinity of C1XS.

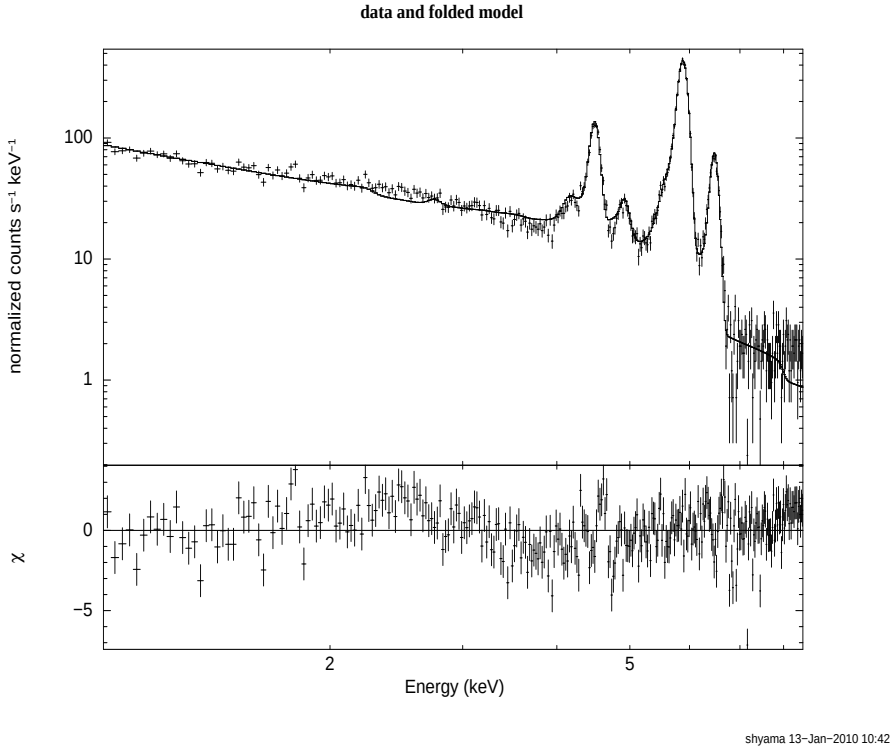

FIGURE 3.28: Spectral fit to the on-board calibration spectrum from Fe-55 radioactive isotopes

3.7 Uncertainties and error propagation

To estimate the uncertainty on the response derived here, we assume the following. The beam is close to being parallel, stable in time and spatially uniform. The active area of the detectors are from the specifications provided by the manufacturer. The errors from the reference detector calibration and spectral fits at each stage in the derivation have been propagated. This results in a weighted average uncertainty of 1.7% on the detection efficiency values. As the SCDs have to be added together for lunar data analysis, we studied the spread in the detection efficiencies of the SCDs which would be another source of uncertainity (Figure 3.29). Accounting for the spread, the unsertainity on

detection efficiency becomes another 4.3%. Thus, the absolute detection efficiency of C1XS detectors is derived with a nominal uncertainty of less than 5%.

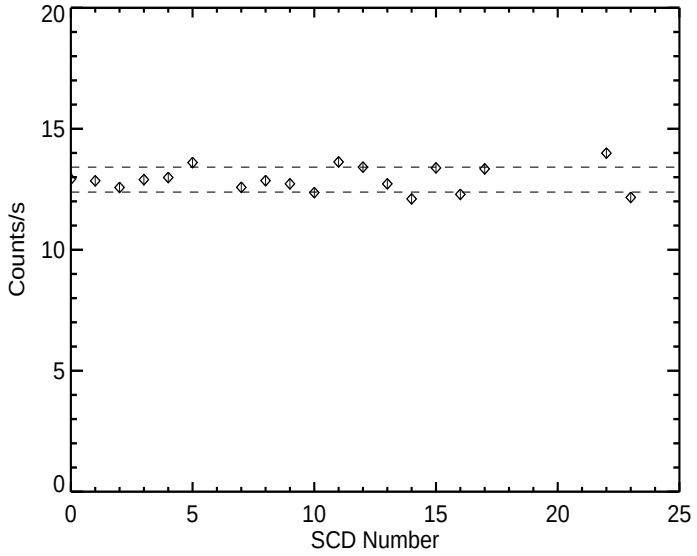

FIGURE 3.29: Relative changes in SCD count rates for the same incident beam as an indicator of the difference in relative efficiency. The dotted lines are drawn at 1σ value (4.3% away from the weighted average).

3.8 Summary

From a very extensive ground calibration program, we have determined the spectral redistribution function of the SCDs as a function of energy and temperature. The fraction of off peak events goes up to a maximum of 70% at 8 keV, the major contribution coming from split events. The detection efficiency of the C1XS detectors was measured with respect to a reference detector calibrated at PTB/BESSY II. A spectral fit to the on-board calibration spectrum from the Fe-55 radioactive isotopes shows the validity of the response matrix derived from ground calibration data, for inorbit analysis. We estimate the overall uncertainty in the calibration to be within 5%. Thus the x-ray line flux measured using C1XS will have a similar uncertainity.

Chapter 4

X-ray fluorescence from the lunar surface

C1XS was in operation in the lunar orbit for 9 months (28 Nov 2008 to 29 Aug 2009). There were more than 32 solar flares during which x-ray fluorescence from the lunar surface could be detected in the instrument. For low intensity flares (A-B class), fluorescence from Mg, Al and Si could be measured while a C3 class flare enabled measurement of Mg, Al, Si, Ca, Ti and Fe from a region in the southern nearside highlands at the spatial resolution for which the instrument was designed for. In this chapter, we provide the detailed description of the methodology followed for C1XS data analysis, the in orbit background variations and specifically derive x-ray line flux from the spectral analysis of measurements during the C3 class flare. The x-ray line flux determined is further converted to elemental abundance which forms the basis for geochemical studies.

4.1 C1XS observations and data analysis

C1XS nominally operated (Figure 4.1) only during the sunlit portion of the lunar orbit. Under good solar illumination conditions (noon-midnight (NM) phase of the annual heliocentric track of Chandrayaan-1) in the 100 km altitude orbit, data were collected for $\sim$ 15 minutes every orbit (half the sunlit portion of the orbit; the remaining lost due to non-optimal detector temperature). This increased to $\sim$ 25 minutes during the dawn-dusk phase. The 14.3° opening angle (FWHM) of C1XS defined a 25 km ground pixel during phase 1 and 50 km pixel during phase 2, on the lunar surface. Since x-ray

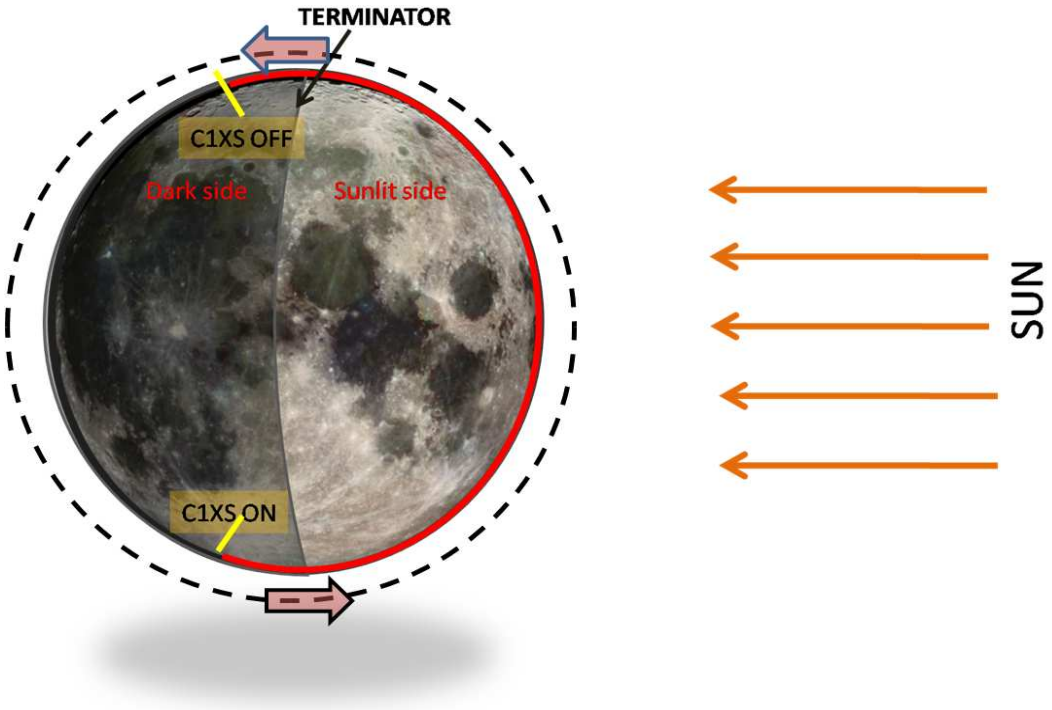

FIGURE 4.1: C1XS was operated only during the sunlit portion of the Moon to limit power dissipation at the detector. The dividing line between the dark and sunlit side is the terminator. The dotted line is a possible configuration of the Chandrayaan-1 orbit around NM geometry

events are time-tagged in C1XS, in order to generate a spectrum, the integration time corresponding to the FWHM ground pixel (25 or 50 km) should be calculated. The velocity of the ground pixel with respect to the motion of the spacecraft (called ground trace velocity) can be calculated from the time period (T) of the spacecraft and perimeter of the Moon (p_{Moon}), as follows. The time period of the satellite can be calculated from Kepler's 3rd law given by:

$$T = 2\pi\sqrt{\frac{GM}{a^3}} \tag{4.1}$$

where 'G' is the gravitational constant, 'M' is the mass of the Moon and 'a', the semi major axis of the orbit (semi major axis of the Moon + altitude of the orbit). The ground trace velocity (v_g) can be calculated as follows:

$$v_g = \frac{p_{Moon}}{T} \tag{4.2}$$

yielding a value of 1.56 km/s, from which the time required to cover 25 km is 16 s and 32 s for the 50 km ground pixel during the second phase of the mission. Corresponding integration times are used to generate spectra during phase 1 and 2 of the mission from the C1XS time tagged events.

Time-tagged events are binned into 4096 ADC channels to generate spectra. We first fit the zero peak with a Gaussian for each SCD and derive the central channel number. The spectra are then shifted along the channels so that the zero peak is in the zeroth channel. The relationship between channel and energy is linear as shown in (Figure 3.21). Therefore the channels can be converted to energy space by multiplying (Energy = Gain $\times$ channel) the channel numbers with the gain (eV/channel). Since gain is temperature dependent, the appropriate value has to be determined for the average temperature for every 16/32 s spectra. From the ground calibration measurements, we have tabulated the temperature dependence of gain (Figure 4.2) for each SCD (the dependence being similar). The on-board temperature of the SCDs were measured using temperature sensors located at the two ends of the array. We assume the temperature of the eight SCDs in the middle as an average of the measurements at either end. The temperature data are available every 60 s, so we interpolate the temperature values for every 16/32 s. The gain corresponding to this temperature is taken from the tabulated values. After gain correction, we re-bin the spectrum from each SCD to a common energy scale and add the spectra together. The added spectrum in 4096 channels is further re-binned to 1024 channels since we are dealing with low event rates. The above described data reduction steps are summarized in Figure 4.3.

The summed spectra (all 24 SCDs) are added in time to enhance statistics, if required. This would result in a coarser spatial resolution on the lunar surface, but was necessary as many of the observations were during A and B class solar flares. Using the SRF and effective area derived on ground, a response matrix is generated for the summed spectrum. The spectrum is analyzed using XSPEC with a suitable background model and response matrix and x-ray line flux in the observed fluorescent lines are determined.

In order to derive the absolute x-ray line flux in the observed XRF spectra from the lunar surface, the background in the C1XS detectors and its variability needs to be understood. We discuss the C1XS background observed in the lunar orbit in the next section.

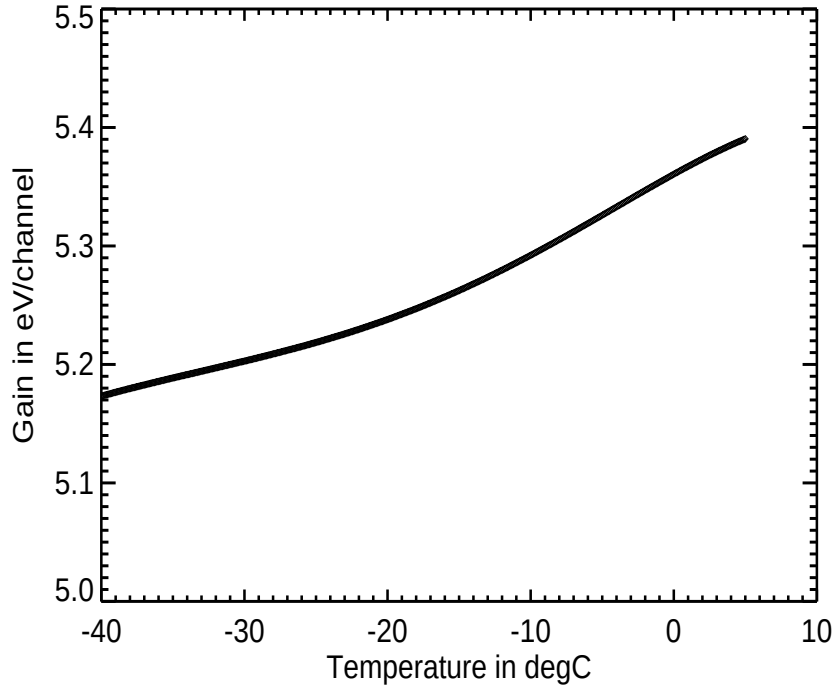

FIGURE 4.2: Temperature dependence (interpolated from discrete measurements) of SCD gain derived from ground calibration data.

4.2 X-ray background in the lunar orbit

The background in an x-ray detector arises from an internal instrumental background and possibly external environmental background. The instrumental background is due to inherent dark current and electronic noise in the system. This is dependent on temperature and also increases with time in orbit (cumulative radiation damage). This component has been measured during the ground calibration and found to be negligible for temperatures less than -5°C. The correlated double sampler efficiently filters out the noise component as has been described in chapter 2. The increase in dark current due to cumulative radiation damage occurs on time scales of months to years and hence is not significant for this work.

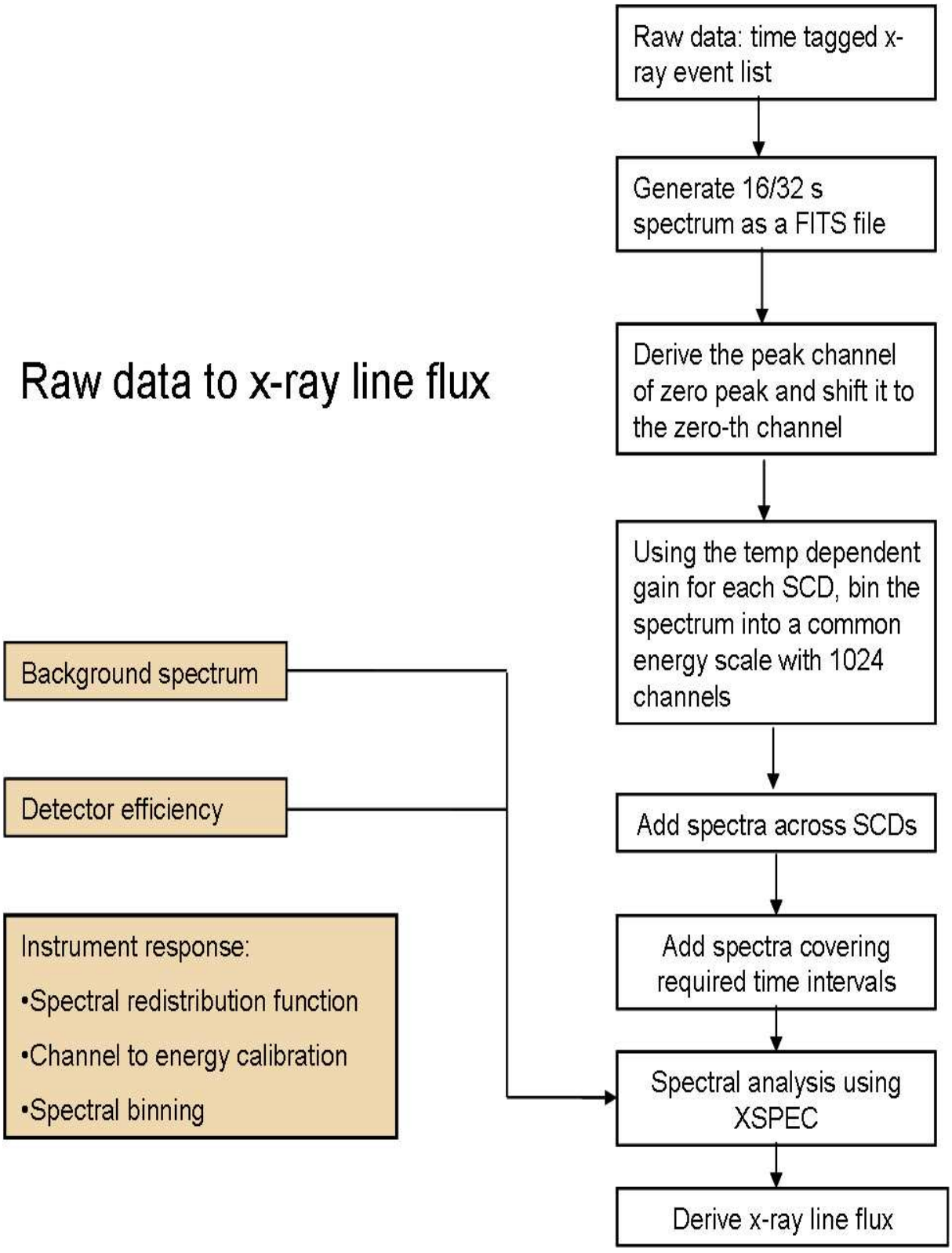

FIGURE 4.3: Steps involved in C1XS data reduction (Time tagged events to summed x-ray spectrum).

4.2.1 Typical background

A featureless continuum background spectrum was measured by C1XS detectors in the lunar orbit. The average detector background count rate ($\sim$ 3 counts/s per SCD) remains constant within 0.2% within an orbit as well as between orbits. This also implies that there are no temperature dependent variations in the detector background (-15°C to -6°C). We compared the spectra obtained from the dark side with that obtained from the sunlit side. Spectra from the sunlit side and dark side are plotted together in the top panel of Figure 4.4 and the difference in count rate in the two spectra plotted in the bottom panel. There is a $\sim$ 2.5% increase in sunlit side count rate in the 2 to 4 keV (bottom panel of Figure 4.4) energy band with respect to the dark side spectrum, indicating the small contribution from scattered solar x-rays. Hence we conclude that the major component of the observed lunar environmental background arises due to the interaction of high energy particles in the orbit with the detector and surrounding material. In the lunar orbit there is a continuous flux of protons and electrons with an energy range spreading from eV to GeV. Lower energy particles directly interact with the detector depositing energy and thus mimicking an x-ray event [Hall, 2008]. Higher energy particles interact with the material surrounding the detector and generate secondary particles which then deposit their energy in the detector.

4.2.2 Detector background during geotail crossings

Electric currents in the Earth's core generate a large scale magnetic field which can be approximated by a dipole within a distance of several Earth radii. The interactions between this field, solar wind (plasma consisting of fully ionized H/He, protons and electrons) and the interplanetary magnetic field results in the formation of distinct regions as shown in Figure 4.5. In the anti-solar direction, the Earth's magnetic field is stretched out into an elongated tail to distances of several hundred Earth radii. It consists of oppositely directed field lines separated by a neutral sheet of plasma with a null magnetic field. Around this, is the plasma sheet which is a source of electrons of average energy 1 keV (increasing to several keV occasionally) [Schneider, 1967]. Moon, during its 29.6 day journey around the Earth, passes through the geotail in 4-5 days around the full Moon. The existence of plasma sheet particles at lunar distances was first established by Explorer 35 [Prakash, 1975]. The observed increase in electron flux (3-50 keV) during its 11 traversals through the geotail is attributed to encounters with the plasma sheet. Phenomena like surface charging observed by Surveyor and Lunar

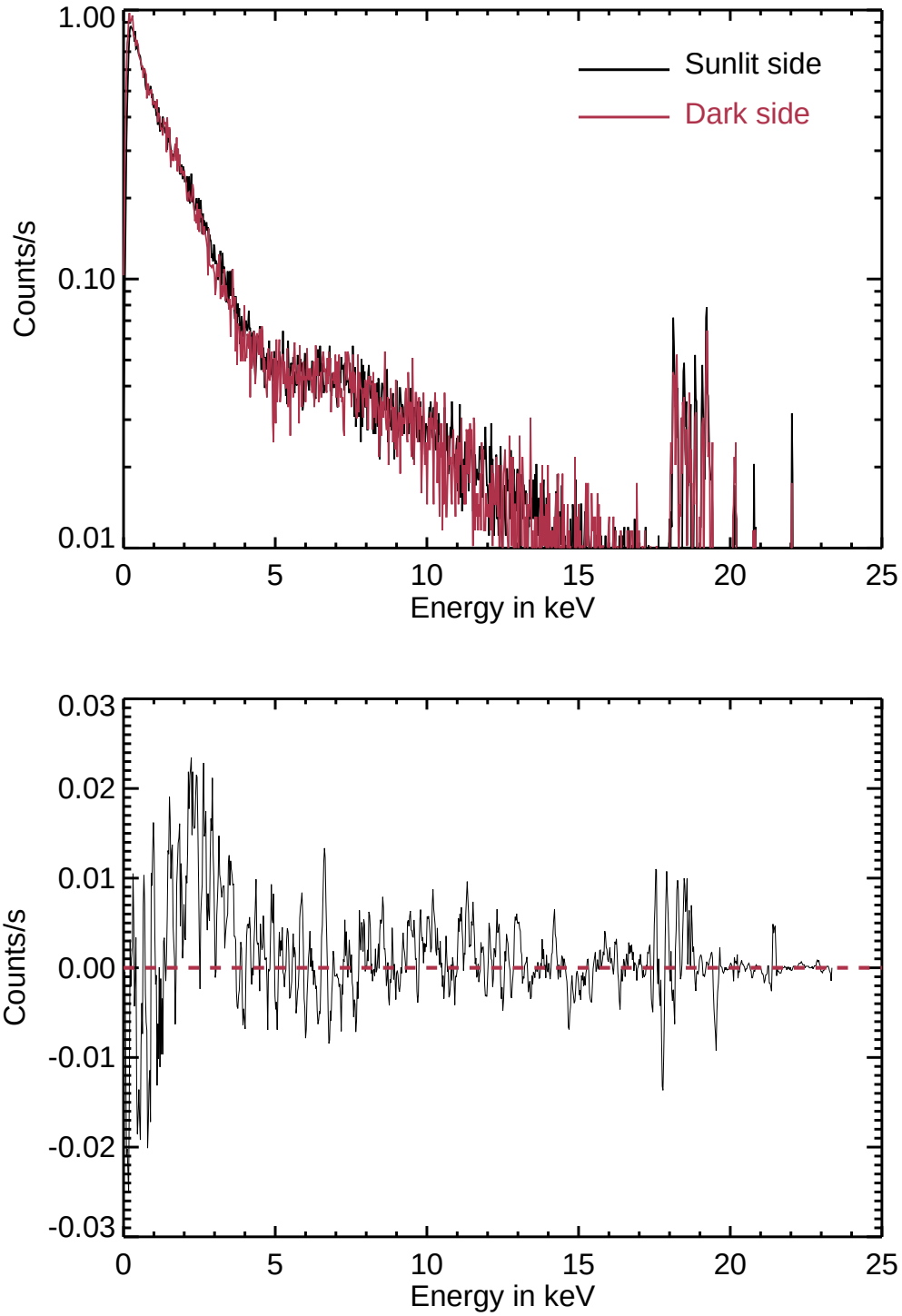

FIGURE 4.4: Typical background in the C1XS-SCDs in the lunar orbit at ∼ -12°C (the coloured spectrum is from the dark side). The bottom panel shows the difference in count rate between sunlit and dark side where there is an enhancement in count rate in the 2-4 keV band

Prospector also suggest encounters with this sheet. The exposure to the plasma sheet is variable and the likelihood of such encounters and possible implications to lunar surface science is discussed in [Haphood, 2007].

C1XS observed a significant increase in the detector background and spectral hardening during some of the magnetotail crossings. A strong Al line whose strength varies over timescales of minutes has also been observed (Figure 4.6) close to terminator crossings of the spacecraft. The change in the spectral shape of the detector background indicates the entry of the spacecraft into a region of different particle population (in energy) and higher flux.

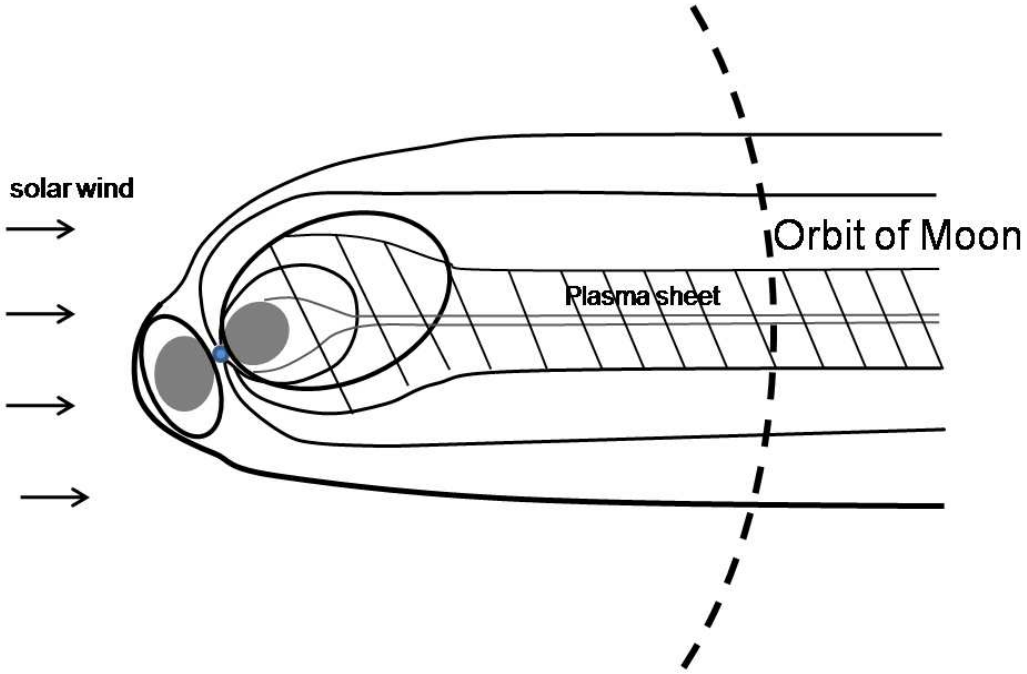

FIGURE 4.5: Structure of the geotail: The solar wind compresses the magnetic field lines facing the Sun, while in the anti-solar direction, the magnetotail extends to several hundred Earth radii.

The Al-K_α line at 1.48 keV appears in the spectra with its intensity varying in timescales of minutes. The line is observed in both sunlit and dark side spectra. To address if low energy electrons can produce this from the thin Al foil in front of the SCDs, we carried out a quick GEANT4 [Agostinelli, 2003] simulation wherein, we irradiated a spectrum (power law of index - 2.0) of electrons in the 1-25 keV energy range (where the section for PIXE is maximum) on a 0.2 μm Al sheet (Figure 4.10) in vacuum. Only $\sim$ 0.01% of the incident electrons generated Al-K_α photons. The typical count rate in the charged particle monitor (RADOM) on Chandrayaan-1 is $\sim$2 counts/s/cm^2 and in the

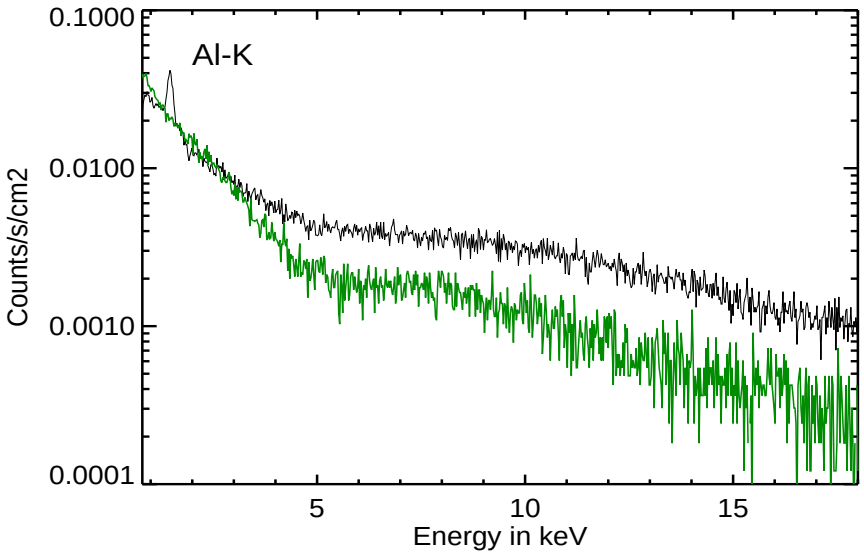

FIGURE 4.6: PIXE induced Al-K$_\alpha$ line during a geotail pass. The green line is the hardened spectrum during the geotail pass overplotted on the typical background.

geotail the count rate increases only by ∼20%. The typical flux from the characterestic Al-K$_\alpha$ photons seen in C1XS detectors is ∼0.4 photons/s/cm^2 which requires a higher particle flux than seen in the 1 to 256 MeV band of RADOM. A measurement of low energy electron flux thus would be required to establish a correlation between Al-K$_\alpha$ and particle flux.

The fact that not all geotail crossings result in a harder continuum spectrum suggest the possible correlation with plasma sheet encounters. Figure 4.7 shows the position of the plasma sheet according to Tsyganenko model [Tsyganenko, 1998] during one of the geotail crossings where the spectrum hardens. A finite possibility that the harder continuum arises due to actual x-ray events from magnetic re-connections in the plasma sheet, also exist. Further work is required to reveal the nature of the processes that lead to the higher background and a hardened spectrum in C1XS during geotail crossings.

For the purpose of this thesis, from the above observations, we conclude that an average background spectrum can be used for spectral analysis during flares, except for observations inside the geotail. For observations inside the geotail, the pre-flare spectra should be analyzed to estimate the possible contribution from PIXE events (particularly to the lunar Al-K$_\alpha$ line).

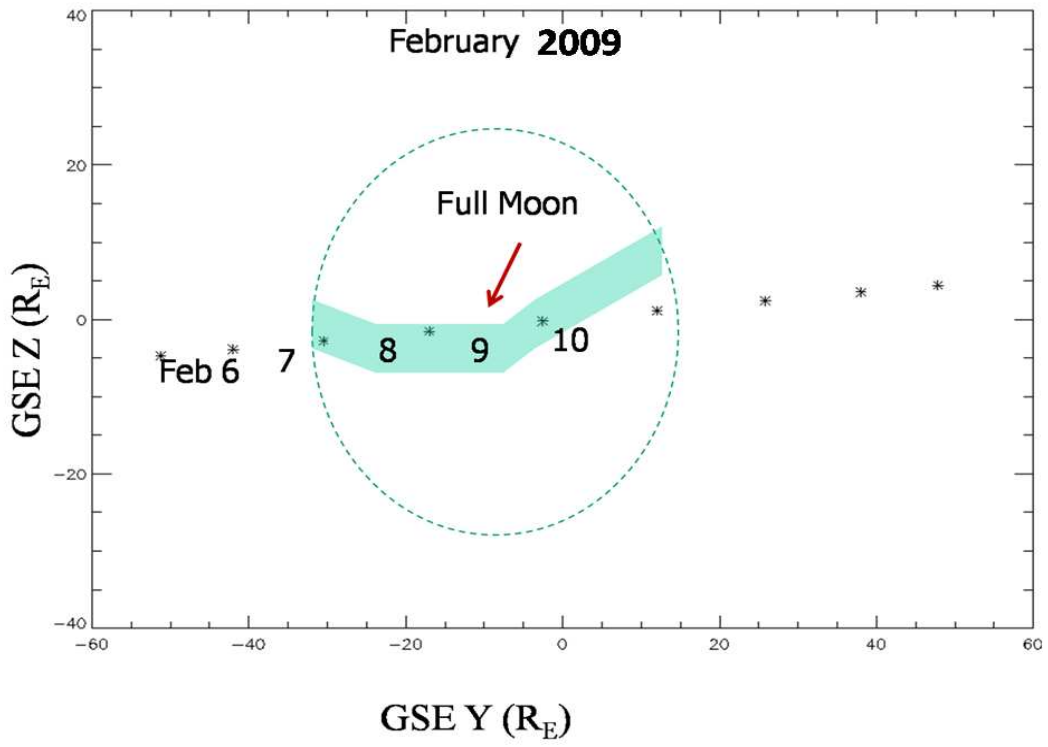

FIGURE 4.7: Plasma sheet encounter during a geotail crossing: The shaded region is the position of the plasma sheet for the full Moon period in Feb 2009 calculated from the Tsyganenko model in Geo-centric Solar Ecliptic (GSE) co-ordinates. X axis points from Earth to Sun, Z axis points towards the ecliptic north pole and Y is in the ecliptic plane.

4.3 X-ray fluorescence from the lunar surface

The x-ray fluorescence spectrum from the lunar surface consists of lines generated as a result of the interaction of solar x-rays with atoms on the lunar surface. Scattered solar x-rays result in a continuum on which the XRF lines are superposed. In this section, we analyze x-ray fluorescence spectra from the lunar surface measured during a C3 class solar flare primarily to describe the methodology of analysis. The weight % from six major elements: Mg, Al, Si, Ca, Ti and Fe are derived and we present these first results from C1XS.

4.3.1 Analysis of the C3 flare XRF spectra

C1XS measured the lunar x-ray fluorescence spectra during a C3 class flare that occurred on 5th July 2009. Figure 4.8 shows the simultaneous increase in counts in a C1XS-SCD and XSM. XRF from Mg, Al and Si could be observed from 07:04:44 UT. Spectra integrated over 32 s corresponding to a ground pixel of 50 km x 50 km could be obtained from 07:10:10 UT to 07:15:00 UT with clearly resolved XRF lines from Mg, Al, Si, Ca and Fe.

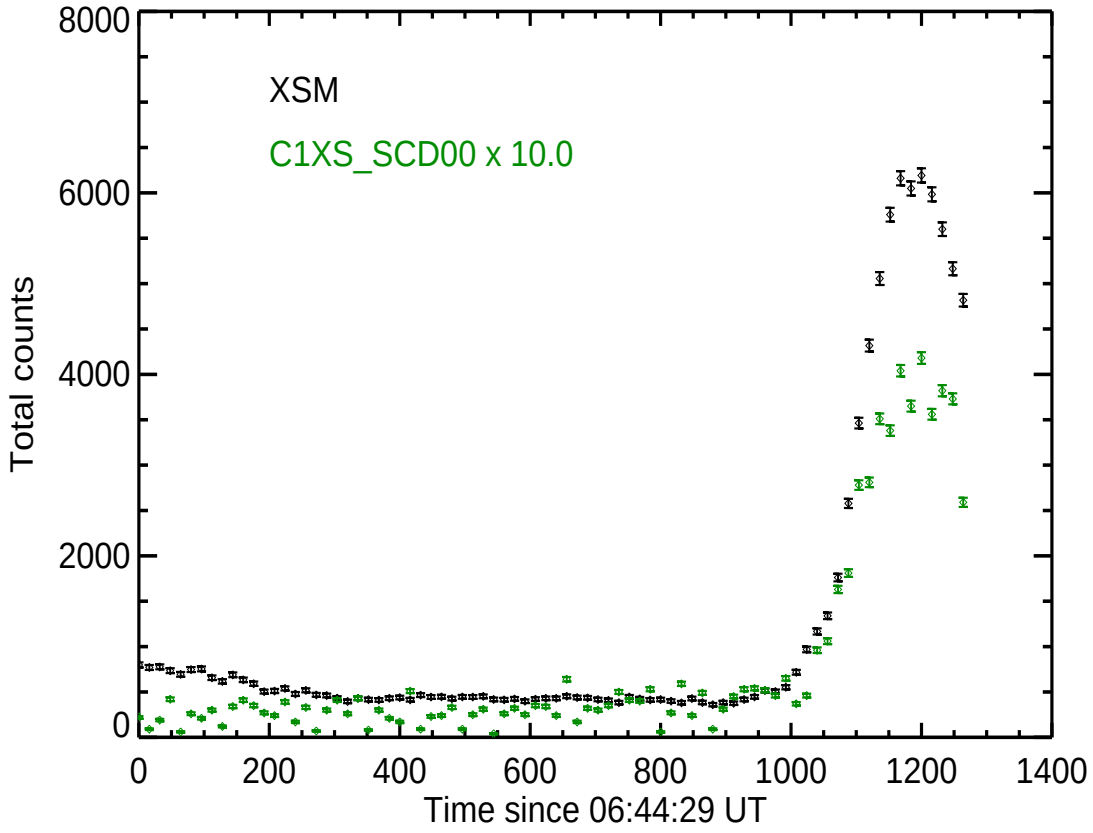

FIGURE 4.8: Simultaneous increase in count rate in XSM and one of the C1XS SCDs during the flare

Since these observations were during a geotail passage (7 July 2009 was full Moon), we studied the pre-flare spectra to understand the detector background. The spectra were sampled at 80 s starting from 06:44:29 UT when C1XS observations began. The PIXE induced Al line from the filter is present in the spectra till 06:51:27 UT though there is no hardening of the spectral continuum. The spectra were fitted with a power law and

a Gaussian and the variation in the Al line flux as well as the power law index is shown in Figure 4.9.

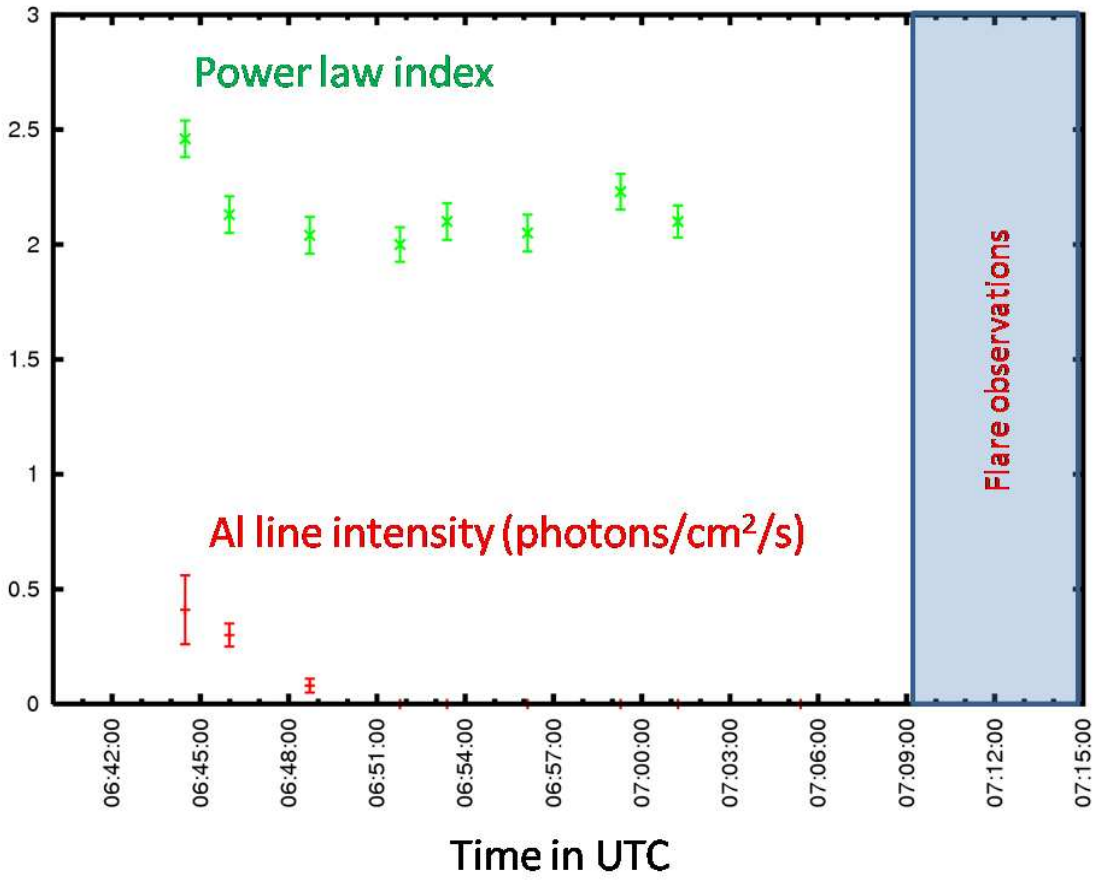

FIGURE 4.9: The variation in PIXE induced Al-K$_\alpha$ line intensity and the power law index of the background spectrum. The Al-K$_\alpha$ disappears after 06:48:30 UT

We have used a background spectrum away from the particle contaminated spectra for analysis of the flare spectra. The background subtracted flare spectra were then fitted with a model consisting of a Gaussian function for each of the observed lines and a power law for the continuum. The continuum presumably has contributions from the scattered solar x-rays. Fits to the XRF spectra are shown in Figure 3.10 and the x-ray line flux derived listed in Table 4.1.

Figure 4.11 shows the variation in x-ray line flux ratio ($x - flux_{ratio}$) from the four strongest lines in the spectrum as a function of time.

$$x - flux_{ratio} = \frac{F_i}{\sum F_i} \tag{4.3}$$

TABLE 4.1: Derived x-ray line flux in photons/cm^2/s

UTC	Mg	Al	Si	Ca-K$_\alpha$	Ca-K$_\beta$	Ti	Fe
07:05:24	0.18±0.07	0.14±0.04	0.37±0.07	0	0	0	0
07:08:04	0.10±0.06	0.04±0.03	0.58±0.11	0	0	0	0
07:09:32	0.18±0.07	0.14±0.06	0.42±0.07	0	0	0	0
07:10:26	0.38±0.18	0.75±0.19	1.05±0.17	0	0	0	0
07:10:58	0.57±0.29	1.27±0.21	2.29±0.20	0.42±0.2	0	0	0.09±0.02
07:11:30	1.30 ±0.30	3.60±0.43	3.30±0.30	0.1±0.04	0	0	0
07:12:02	3.30±0.20	9.30±0.34	6.90±0.34	0.1±0.05	0	0	0
07:12:34	6.19±0.30	18.30±0.43	14.40±0.43	2.12±0.2	0.39±0.13	0	0
07:13:06	9.57±0.04	28.40±0.43	23.13±0.45	3.06±0.1	0.31±0.043	0.01±0.02	0.28±0.04
07:13:39	14.03±0.80	32.10±0.70	28.05±0.59	3.35±0.12	0.53±0.072	0.09±0.03	0.44±0.05
07:14:11	16.31±0.89	28.65±0.94	33.09±0.71	3.01±0.11	0.35±0.052	0.08±0.02	0.15± 0.03
07:14:43	17.30±0.74	28.90±0.60	31.10±0.6	2.65±0.13	0.34±0.08	0	0.18 ±0.03
07:15:16	11.81±0.69	28.46±0.69	27.18±0.55	1.83±0.09	0.23±0.05	0	0.23±0.04

Here the total flux F_i includes constant contribution from 44% oxygen, where we calculate F_i as follows

$$\frac{F_O}{\sum F_i + F_O} = 0.44 \tag{4.4}$$

Knowing the total flux in other observed elements, the expected flux from oxygen, F_O can be calculated. To first order, a flux ratio eliminates the dependence of x-ray line flux on variation in solar intensity. However, in this work the x-ray line flux values are converted to elemental wt% as described in the following sections, in order to finally discuss local lunar chemistry.

Weak lines of Cl-K$_\alpha$, K-K$_\alpha$, Ti-K$_\alpha$, Cr-K$_\alpha$ and Mn-K$_\alpha$ are also observed during the brightest part of the flare. These are in general expected to be minor elements whose weight % is lesser than 1 in lunar samples (Ti-K$_\alpha$ is also a minor element in highlands). The strength of these seem to vary even during constant solar flux levels suggesting compositional changes across the pixels. Here, we do not attempt to quantify it since the detection is of less than 2σ level (by comparing the number of counts in the line to the number of counts in the background spectrum in the same energy band). The quantification of these elements require further analysis (not undertaken in this thesis).

4.4 Conversion of x-ray line flux to elemental abundance

The number of x-ray fluorescence photons produced from a sample, for a given incident spectrum of x-ray photons, can be calculated analytically. Originally done by Sherman [Sherman, 1955] and further modified by Shirawai and Fujino [Shirawai and Fujino,

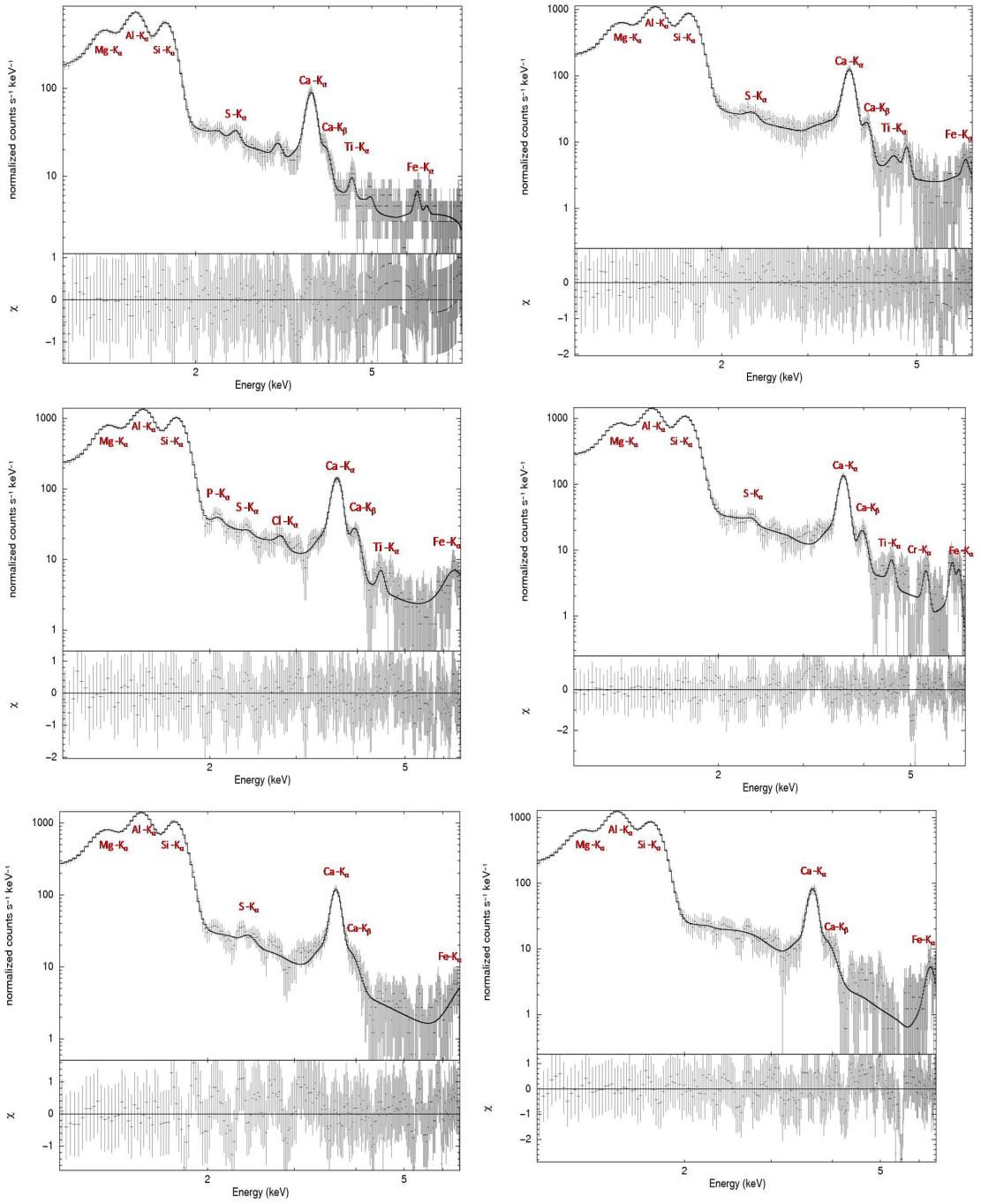

FIGURE 4.10: Spectral fits to the flare spectra

1966], the number of primary x-ray fluorescent photons I_i (for an infinitely thick sample) from an element i is given by [Jenkins et al, 1995].

$$I_i = \frac{1}{4\pi sin\psi_1} \int_{E_0}^{E_{max}} \frac{Q_{if}(E_0) I_0(E_0) dE_0}{\mu(E_0) cosec\psi_1 + \mu(E_i) cosec\psi_2} \tag{4.5}$$

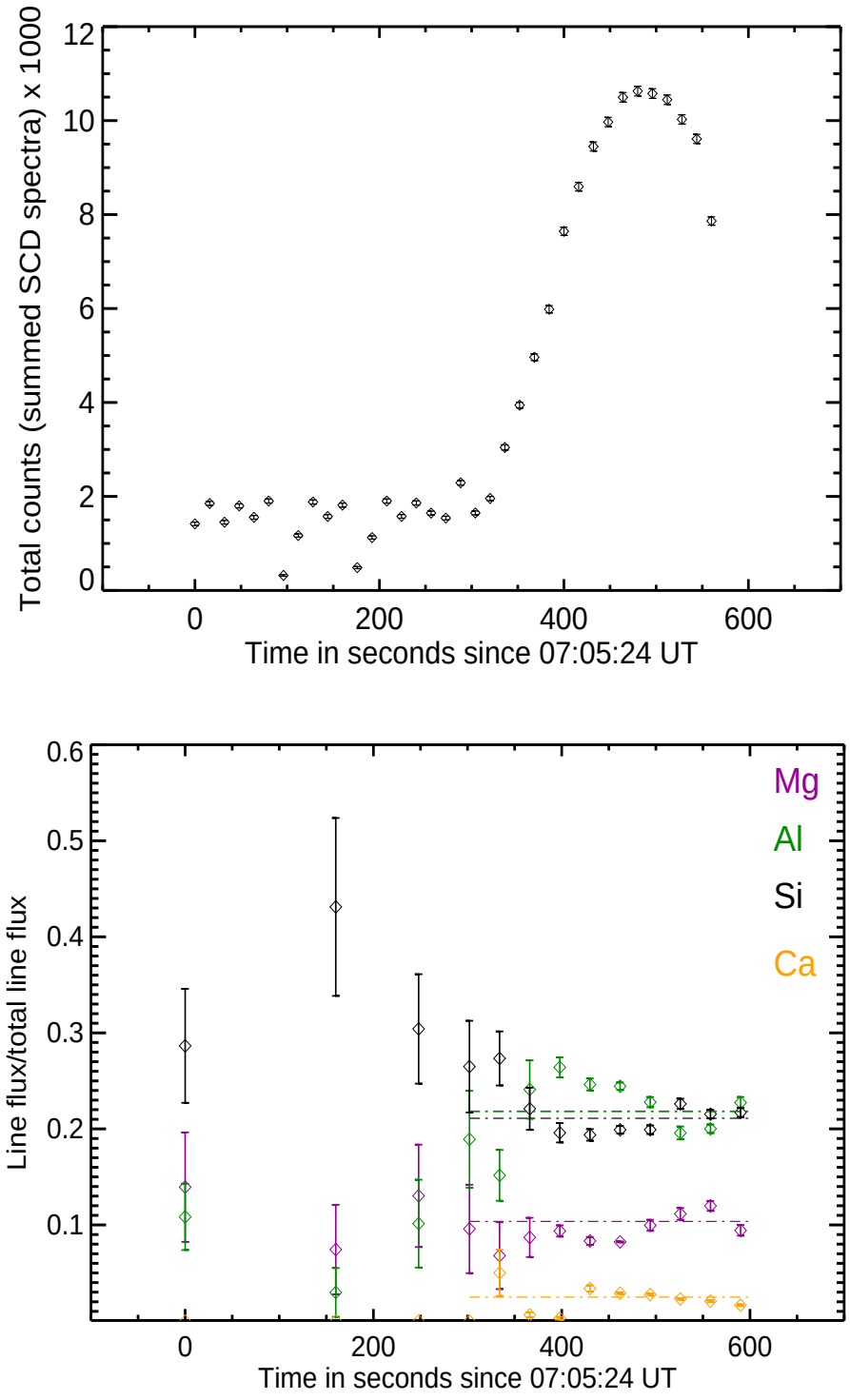

FIGURE 4.11: Variation in x-ray line flux across lunar ground pixels (bottom panel). The horizontal lines are the average flux derived from the summed spectrum for the time period indicated. Line flux with large error bars are during the pre-flare times. The total counts in the summed SCD spectra for the same time period is plotted in the top panel.

where $I_0(E_0)$ is the incident spectrum, ψ_1 is the angle of incidence, ψ_2 is the angle of emergence (Figure 4.12), $\mu(E_0)$ is the total mass attenuation co-efficient (in cm^2/g) for the energy E_0 and $\mu(E_i)$ for the energy E_i of the fluoresced element. Q_{if} is a measure of the fluorescent probability for element i and can be calculated as follows.

$$Q_{if} = W_i \tau_i(E_0) \omega_{Ki} \frac{r_K - 1}{r_K} \omega_{Ki} f \tag{4.6}$$

In the above equation, W_i is the weight fraction of the i^{th} element, τ_i is the total mass absorption co-efficient for the element i, ω_{Ki} is the K shell fluorescent yield of the i^{th} element, r_K ($= \frac{\tau_+(\phi_K)}{\tau_-(\phi_K)}$) is the K edge jump ratio. ϕ_K is the binding energy of an electron in the K shell. In a matrix of elements, the primary x-ray fluorescent photons can further interact with the atoms of other elements and produce secondary fluorescence (provided their energy is above the binding energy for electrons for the companion element) and even tertiary fluorescence. Shirawai and Fujino calculated the number of secondary and tertiary fluorescent photons generated in a matrix, in addition to the primary. The incident x-rays interact with the sample via Rayleigh (coherent) and Compton (incoherent) scattering as well.

4.4.1 Compton scattering

The inelastic scattering where a photon interacts with a free electron at rest and transfers a part of its energy to the electron (electron recoils), is called Compton scattering. The scattered photon has an energy (E_s) less than that of the incident photon (E_i), given by

$$E_s = \frac{E_i}{1 + \gamma(1 - cos\theta)} \tag{4.7}$$

where θ is the angle between the incident and the scattered photon. The intensity of the scattered photons can be calculated as:

$$I_s = I_i \times \frac{d\sigma_{KN}}{d\Omega} \tag{4.8}$$

where $\frac{d\sigma_{KN}}{d\Omega}$ is the differential scattering cross section (called Klein-Nishina collision cross section) in cm^2/electron-steradian. In a matrix of elements the scattering from each element (weighted by its concentration) is summed to get the total contribution from scattering.

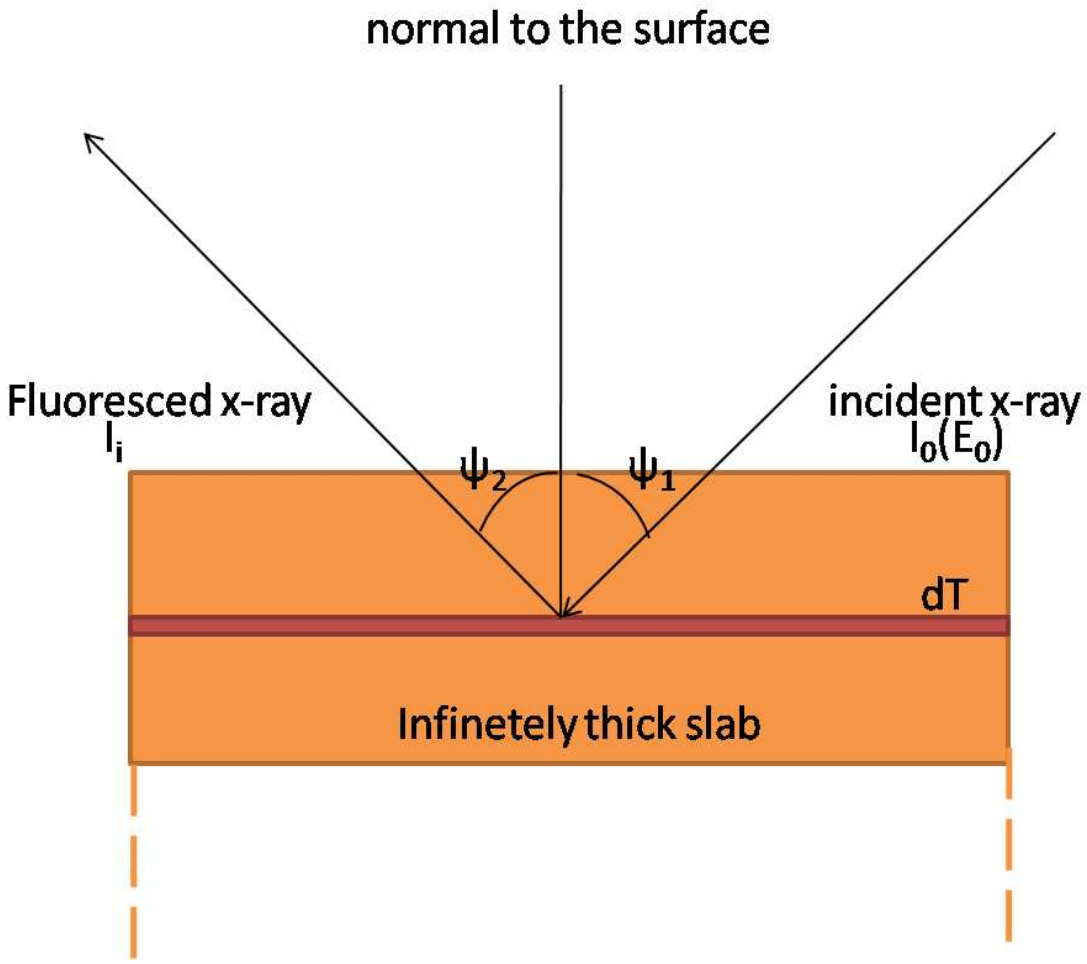

FIGURE 4.12: X-ray fluorescence geometry; the incident x-ray beam interacts in the small volume dT

4.4.2 Rayleigh scattering

Rayleigh scattering is the process in which the incident photons are scattered by the bound atomic electrons (this is called Thompson scattering when electrons are free) without any change in their energies. The differential Rayleigh scattering cross section $\frac{d\sigma_R}{d\sigma_\Omega}$ is given by

$$\frac{d\sigma_R}{d\sigma_\Omega} = \frac{1}{2}{r_0}^2(1 + cos^2\theta)F(x, Z)^2 \tag{4.9}$$

where ${r_0}^2$ is the classical electron radius and $F(x, Z)$ is the atomic form factor and is a function of (E_i), atomic number (Z) and θ.

4.4.3 Factors affecting XRF intensity

The set of all elements in a sample is called a **'matrix'**. The XRF line flux (I_i) from a particular element 'i' is proportional to the number of atoms of the element present in the matrix and thus to the weight % W_i (the percentage by weight of a particular element with respect to all other elements in the sample). But I_i does not vary linearly with W_i for the following reasons.

- I_i is dependent on the incident spectrum which excites the sample.
- Matrix effects: If the number of XRF photons from an element i (N_i) have energies greater than the binding energy of K-shell electron of element j, then x-rays from element j are excited. Thus a fraction of the photons (N_j) of element i is used to generate XRF photons from j. Element j is thus 'enhanced' and simultaneously intensity of i is reduced. Further, XRF photons from i and j could get absorbed by the higher atomic number elements in the sample resulting in a further reduction in N_i. Thus N_i are sensitive to the 'matrix' of elements in the sample.
- Particle size: The lunar regolith being sensed remotely through x-rays contains a distribution of particle sizes ranging from cm-sized rocks to ultrafine (2 μm) particles. In regions where the mean particle size is larger than the penetration depth of x-rays (which is the case of lunar regolith), particle size affects the x-ray fluorescent line intensity. Laboratory experiments have shown that the x-ray fluorescent line intensity for a given element decreases with increasing particle size (Kuwada, Okada and Mizutani 1997).
- Geometry of observation: X-ray fluorescence intensity is sensitive to the angle of incidence (θ) of solar x-rays with respect to the lunar surface and to the phase angle (ϕ).

Clearly, the observed line strength (I_{obs}) of an element is not a direct measure of the true abundance. However, one can define a relationship between I_{obs}(i) and a corrected line intensity I_o(i) (which can be directly related to the true abundance of element i) as

$$I_{obs}(i) = f(S(E), i)[I_o(i) * M(S(E), E) * P(E, \theta, \phi, i)] \tag{4.10}$$

where f (S(E),i) represents a function of the incident solar spectrum S(E) for element i . P (E,θ,ϕ,i) includes cumulative effects of mean particle size and *' represents convolution.

4.4.4 Sensitivity of lunar XRF to the incident solar spectrum

X-rays from the quiet Sun arise from the hot coronal plasma. Compared to the 5500°K temperature of the photosphere (where the emission peaks in visible), the solar corona is at a million degree K. The mechanisms by which solar corona is heated to such a high temperature is still an open question in solar physics. The x-ray emission from the Sun is highly variable along the solar cycle ($\sim$ 11 year cycle). A sudden increase in solar x-ray intensity, of the order of 10-10^5 times the quiescent, lasting minutes to hours is called a solar flare. The number of solar flares increase with increase in solar activity. The frequency of more intense solar flares also increase near solar maximum. Solar flares occur at spatially small regions in the corona and evolve as the flare intensity increases. For a detector like XSM, though we measure the x-ray spectrum from the whole solar disk, it would be dominated by x-rays from the flaring region.

Depending on the intensity of the solar flare, they are classified as A, B, C, M or X where an X class flare is 10^5 times stronger than an A class flare (logarithmic scale). There are further subdivisions within each class ranging from A1 to A9 (for example A2 flare is twice intense as A1). This classification is based on flux measured in the 3 - 12 keV band by the Geostationary Operational Environmental Satellites (GOES) which have been continuously monitoring solar x-ray flux from 1975 to date.

The quiescent solar x-ray spectrum can be modeled as emission from a hot single temperature, optically thin plasma with coronal elemental abundances similar to photospheric. During flares, it is observed that there are multi thermal components (ie, regions of different temperatures) and often a non-thermal component which extends to several hundred keV. Emission from a hot isothermal optically thin plasma as in the case of Sun, has been modeled by several researchers in the past. The emission consists of a bremsstrahlung continuum on which several line emissions are superposed. The line emissions arise from ions excited by collisions with electrons (wherein the excited ion decay spontaneously) whereas the bremsstrahlung arises from the interaction of free electrons with the Coulomb field of the nucleus (free-free transition between two continuum states, as free-bound transition or a two photon process). Over a wide temperature range from 0.01 to 10 MK, the x-ray spectrum has several emission lines from the partially ionized heavier trace elements. Doppler broadening of the spectral lines are also observed. The intensity of emissions lines are dependent on the coronal elemental abundances as well as the electron temperature (the distribution of electrons is assumed to be Maxwellian).

We carried out a preliminary study of the change in XRF line intensities from a sample of lunar composition when irradiated by different solar spectra, using simulations. GEANT4 (Geometry and Tracking) is a Monte Carlo-based C++ simulation toolkit developed by CERN towards studying high energy particle and photon interactions in different media with an ability to examine energy loss processes and related parameters for any given experimental set up. This toolkit is used to write a simulation code that defines the lunar geometry, various terrain compositions, incident solar spectra representing different phases of flares and receiving geometry of C1XS. Geometry of the detector arrangement and photon propagation directions are verified through visualization tools.

A slab of volume 50 km x 50 km x 10 m is constructed with a composition specific to a lunar region. The full ground pixel of C1XS is 50 km x 50 km from a 100 km altitude. The solar spectrum is assumed to be incident perpendicular to the slab. Low energy processes are invoked under GEANT4 physics. The significant physical processes in the energy range of interest are photoelectric effect (which leads to fluorescence) and scattering. The scattered photons from the slab constitute the continuum in the lunar soft x-ray emission spectrum. The geometry is shown in Figure 4.13.

For a realistic simulation of solar spectra, we have used data from the Reuven Ramaty High Energy Solar Spectroscopic Imager (RHESSI), launched on 5th Feb 2002 to study solar flares at energies between 3 keV and 17 MeV. Spectral analysis was done for a range of solar activity, from quiet sun to X2 class flares. Figure 4.14 shows the simulated lunar XRF spectra from a slab of mare basalt composition for C1 and M2 class flares. Figure 4.15 shows the variation in x-ray line strength with integrated solar flux. Our results confirm in general, the sensitivity of the x-ray fluorescent line strength to the incident solar spectrum. During the evolution of the C1 flare ($\sim$ 10 times increase in flux from start of the flare to the peak), the relative fluorescent line strengths do not vary significantly. This implies that at nominal C1 flares, if adequate signal strength is not available from a typical ground pixel, addition of adjacent ground pixels maybe carried out to derive a higher signal-to-noise ratio without significant impact from the evolution of the incident solar spectrum. However, during a M2 flare, the solar flux increases more than 100 times and the line strengths vary in proportion to the solar flux (1-20 keV) (Figure 4.15). This arises largely due to the increasing contribution of the non-thermal component to the total solar flux. Interestingly, for the same solar flux level, the line strength of a given element is significantly larger for M2 than for C1. This is because of differences in the solar spectrum- specifically changes in the non-thermal component. Our solar spectral analysis showed that during M2, the spectral index of

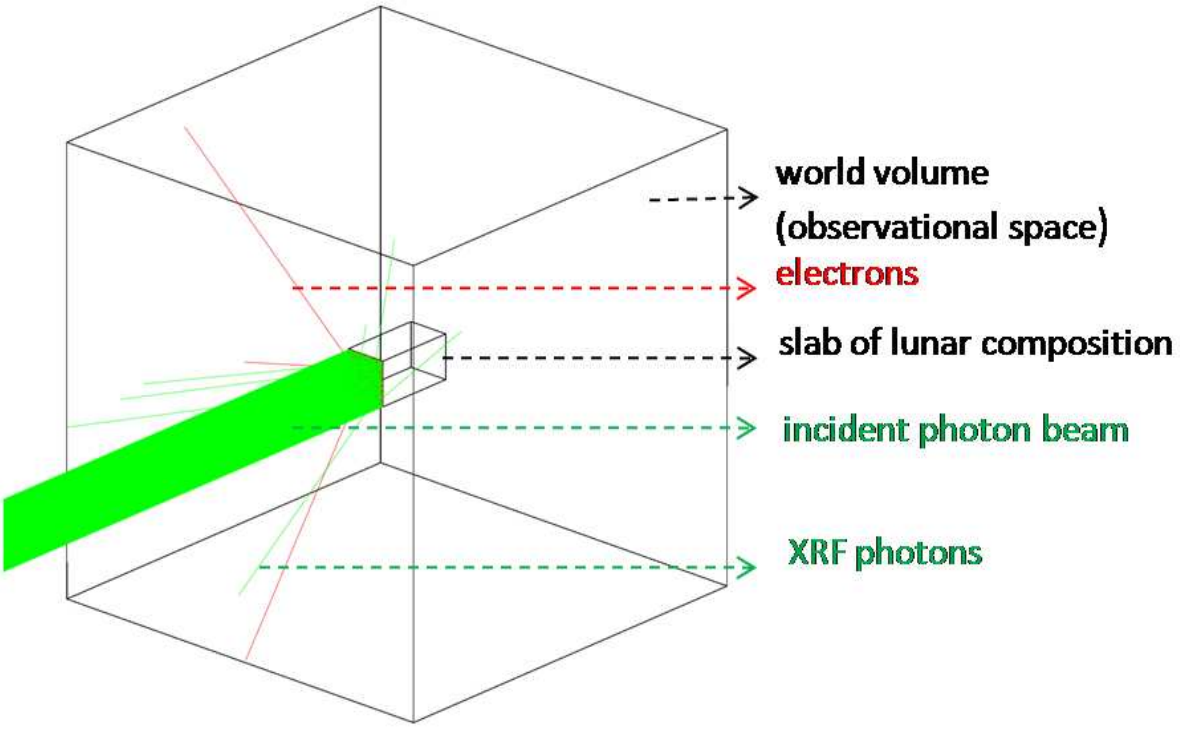

FIGURE 4.13: Geometry used in GEANT4 for XRF simulation

the non-thermal component ranged from 3 to 2, in contrast to the C1 flare, where the power law index remained at ∼5.

XRF line flux from low Z elements Mg, Al and Si are largely dependent upon the thermal component in the solar spectrum while Ca, Ti and Fe are affected by the harder non-thermal component. The simulated points corresponding to the highest integrated flux represent a softer spectrum and yields lower flux values for high Z elements (Figure 4.15).

The necessity to address incident solar spectral sensitivity to observed x-ray line flux was highlighted by many in the past. In earlier experiments, relatively modest energy resolution detectors such as proportional counters or flux from GOES were used to derive elemental abundance. But higher resolution x-ray detectors like XSM can provide more accurate solar spectral models to correct for the corresponding XRF line flux variation.

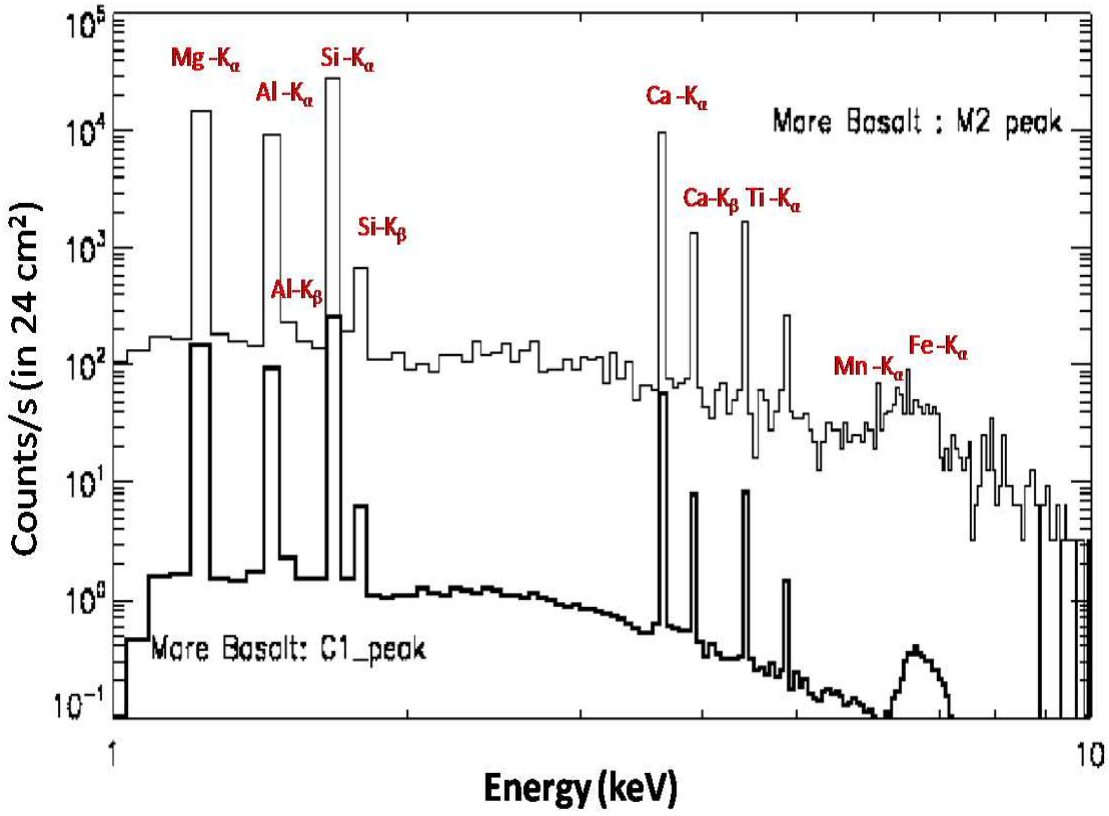

FIGURE 4.14: Simulated lunar XRF spectrum during two levels of solar activity

4.5 Methods for conversion of XRF line intensity to elemental abundance

4.5.1 Laboratory methods

The concept of 'standard samples' is used in laboratories to derive the wt% of the element under study (called the analyte) in an unknown sample. Standard samples of known compositions covering a range of weight percentages of the analyte, is used to determine the XRF line intensity from the analyte. Ideally, a plot of wt% of the analyte against XRF line intensity from the standard specimens would be a straight line starting at zero and this is called a 'calibration curve'. If the XRF line intensity of the analyte in the unknown sample is measured, its wt% can be derived from the calibration curve. Matrix effects result in non-linear calibration curves. Particle size effects are removed by specimen preparation. Controlled x-ray beams at pre-defined incident angles are used in laboratories to excite the sample and hence such effects are also not unknowns.

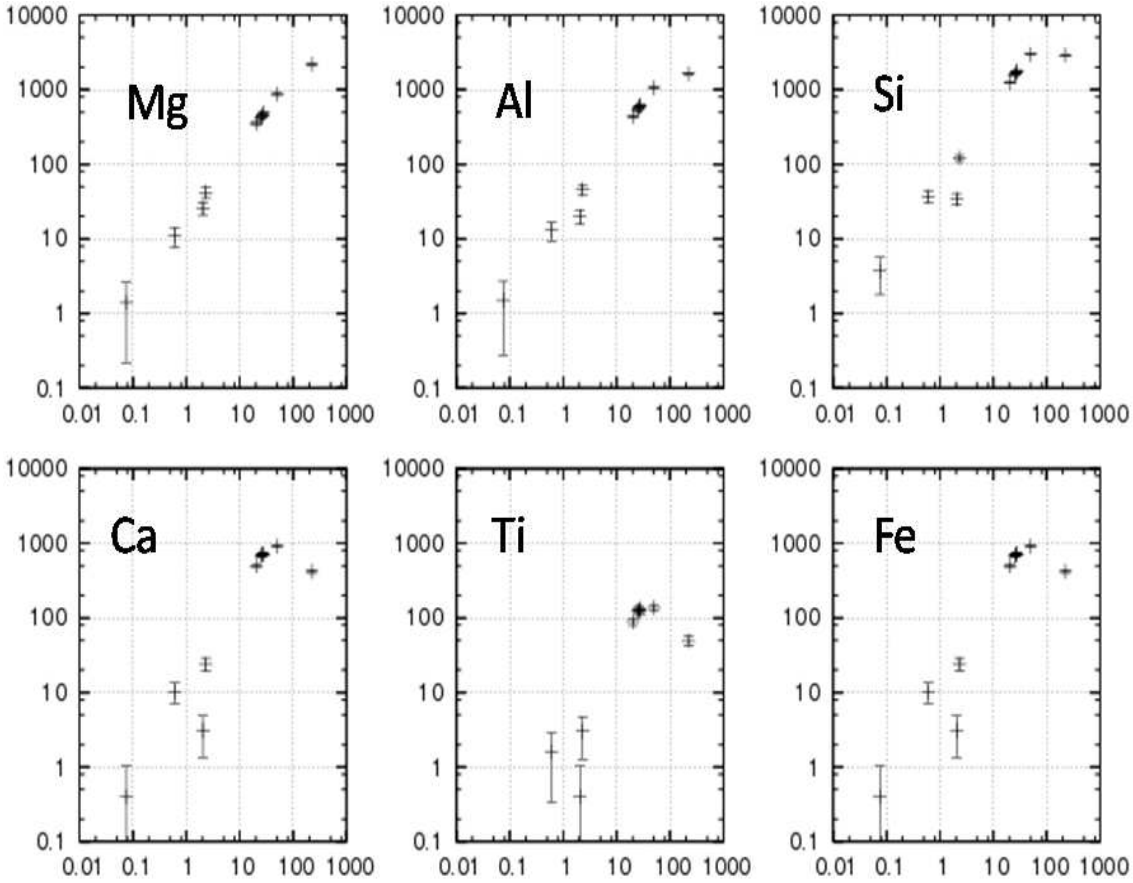

FIGURE 4.15: Variation in XRF line flux from the six major elements solar flux (integrated from 1-20 keV). Deviations from linearity indicate that XRF line flux does not just linearly increase with increase in incident solar flux.

Figure 4.16 shows a calibration curve using the XRF line intensities derived from the GEANT4 simulation with a set of lunar sample compositions. Deviations from non-linearity seen here are dues to matrix effects.

Matrix effects are tackled either by eliminating (diluting the sample) or measuring (using internal standards) the effect or by calculating the effect mathematically. There are two main categories of mathematical methods:

- **Fundamental parameter (FP) method:** The XRF intensity is calculated using the fundamental parameters of absorption co-efficients as described in section 4.4. XRF line intensity from standard samples are calculated by FP method and calibration curves are generated. A special case of this method is to use a pure sample (ie 100% of the element) as the standard.

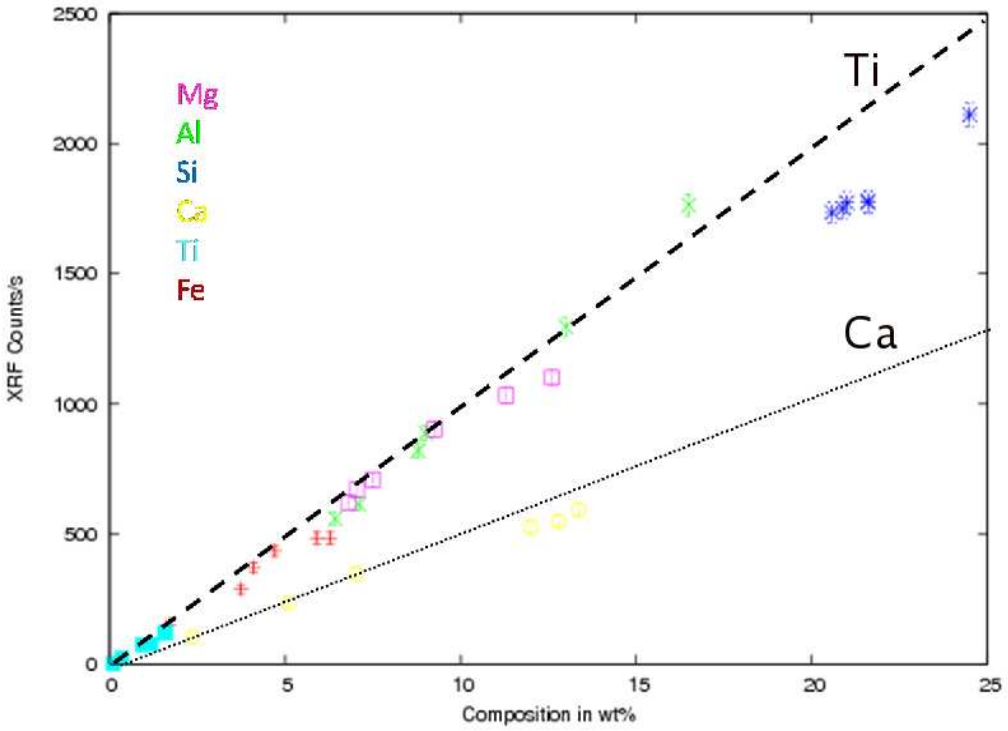

FIGURE 4.16: Matrix effects in lunar samples (deviations from linearity are indicative of matrix effects). The straight lines drawn represent a schematic calibration curve for two of the elements Ca and Ti.

- **Method of influence co-efficients:** In this method, the matrix effects are calculated analytically or empirically and corrected for.

4.5.2 Remote sensing XRF experiments

For remote sensing measurements where there is no control over the geometry of observation, the incident spectrum or particle size in the sampled region, fundamental parameter algorithms are employed to convert XRF line intensity to elemental wt%.

The Apollo 15 and 16 XRS experiments used solar x-ray flux from the Solrad 10 satellite and constructed a two temperature model (based on the assumption of a stable corona and an active spot) based on Tucker and Koren [ref]. Theoretical x-ray line intensities were calculated using a fundamental parameter method for a set of known lunar compositions (from the samples brought by astronauts- called as 'ground truths'). These were then compared with the observed and the best match determined. A correction factor which is a function of the solar flux hardness ratio (a measure of the spectral variation)

is derived, which relates the observed and calculated line ratios. The Apollo experiments using this method has mapped about 10% of the equatorial near side of the Moon.

More recent XRF experiments on NEAR ([Nittler, 2001], [Lim, 2009]) and Hayabusa ([Okada, 2006]) have also followed a similar strategy wherein two band solar flux from GOES is used to model the solar spectrum with more advanced solar emission models like CHIANTI ([Dere, 1997]).

The basic difficulty in all the earlier experiments has been the non-availability of a simultaneous solar spectrum with energy resolution good enough to accurately model the emission lines in the solar spectrum. Particle size and geometrical effects are partially eliminated by comparing ratios of line intensities to derive the best fit composition.

4.5.3 C1XS approach

In the present work, fundamental parameter algorithm using the the x-ray fluorescence equation as given by Shirawai and Fujino (1962) has been implemented as an IDL code x2abundance (Athiray et al in preparation). The difference with earlier approaches is that we first calculate analytically, the expected x-ray line flux for a matrix of elemental concentrations covering a reasonably wide range (including Rayleigh scattering). The calculated x-ray line flux is then compared with the observed using a chisquare minimization algorithm. The best set of weight percentages are chosen as the one with the minimum chisquare. Unlike other approaches where consistency with known elemental weight % are addressed, this approach derives the best combination of weight % that matches the observed x-ray line flux and known solar spectrum incident on the lunar surface. This means that we do not start with any presumed lunar compositions but arrive at the best values of weight % based on the observed x-ray line flux. A larger parameter space (in steps of 0.5 wt%) is searched in order to eliminate other local minima and to establish a smooth convergence. Further details of the XRF code (x2abundance) and its validation against laboratory samples are given in Athiray et al in preperation.

4.6 Elemental abundance from the C3 flare analysis

4.6.1 XSM spectral analysis

The XSM spectra were fitted with a single temperature (vtherm_abund in OSPEX which is a model based on CHIANTI [Dere, 1997]), varying the coronal abundance to obtain a best fit for the intensity of emission lines in the spectrum. XSM resolves the lines in the solar spectrum fairly well and hence has the capability to determine changes in coronal abundance during the flare. A single temperature model seems to be sufficient to model the 1-10 keV solar spectra for this flare and hence we did not take into account the harder component that is present in many solar flares. Table 4.2 gives the spectral parameters (emission measure EM and plasma temperature T) derived for the XSM spectra for the brighter part of the flare. Figure 4.17 shows the spectral fits and Figure 4.18 the evolution of the temperature and emission measure.

TABLE 4.2: Solar spectral fit parameters (Lalita.S and S. Subramaniam, priv. commn).

Time (UTC)	**EM ($\times$ 10^{49} per cm^3)**	**T (keV)**
07:13:05	0.17±0.005	1.15±0.02
07:13:37	0.22±0.002	1.12±0.006
07:14:09	0.20±0.002	1.10±0.006
07:14:41	0.18±0.005	1.01±0.01
07:15:16	0.15±0.002	0.95±0.005

4.6.2 C1XS elemental weight percentage

The solar spectral model (from the best fit to the solar spectra) was used as input to the XRF code in order to calculate the lunar XRF intensities from five major elements Mg, Al, Si, Ca and Fe for a stretch of 250 km x 50 km at 50 km spatial resolution. The elemental abundance (weight%) obtained from the five brightest lunar ground pixels for this intense part of the flare is given in Table 4.3. Figure 4.19 shows the variation in elemental wt% across these five ground pixels along with the variation in XRF flux ratio. Qualitatively, the wt% variation follows the trend in variation of flux ratio.

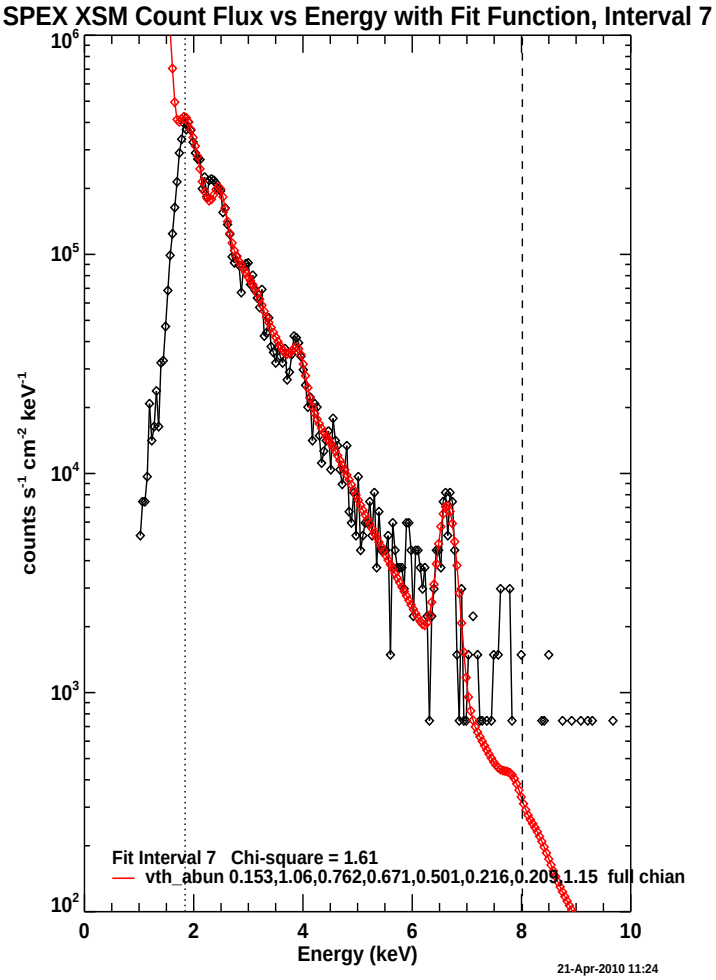

FIGURE 4.17: Fit to one of the XSM solar spectra, Lines from ionised S, Ca and Fe can be seen above the continuum.

TABLE 4.3: Derived elemental wt %

Time (UTC)	Mg	Al	Si	Ca	Fe
07:13:06	5±1.5	19 ±1	20±1	7±1.5	4.0±0.5
07:13:39	5±1.5	17 ±1.5	19±0.5	7±1	6.0±1.5
07:14:11	6±0.5	15.5±1	23.5±0.5	7.5±0.5	2.5±1.5
07:14:43	6±0.5	15.5±0.5	22±1	7±0.5	5.0±1.5
07:15:16	4±0.5	16 ±0.5	21±1.5	6±0.5	7.0±1.5

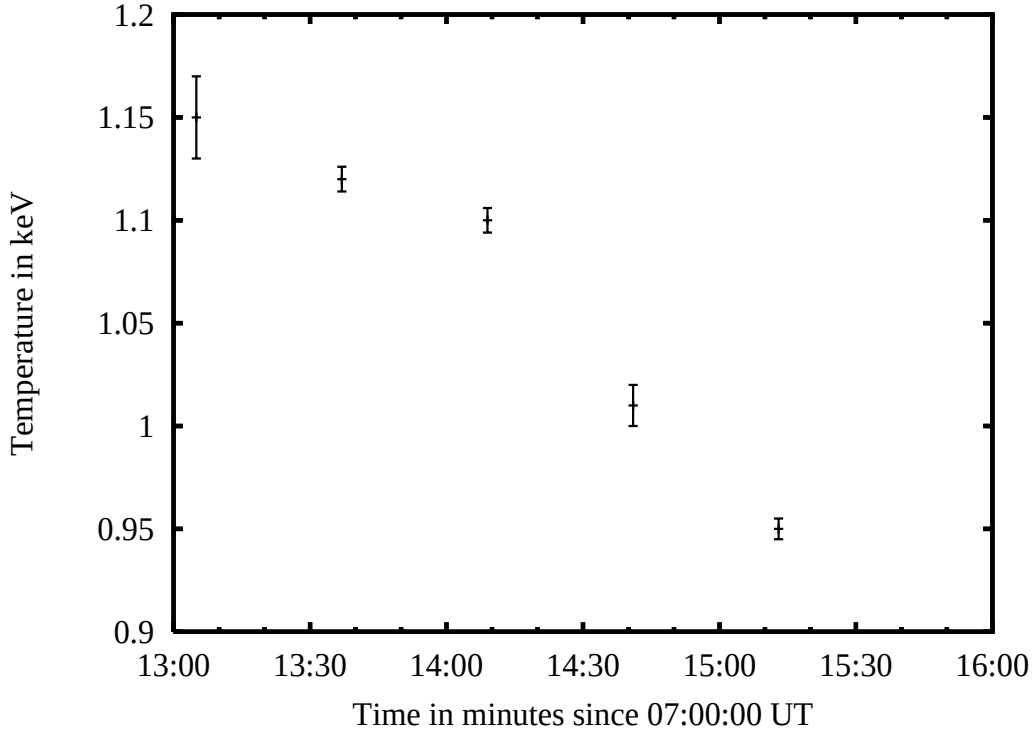

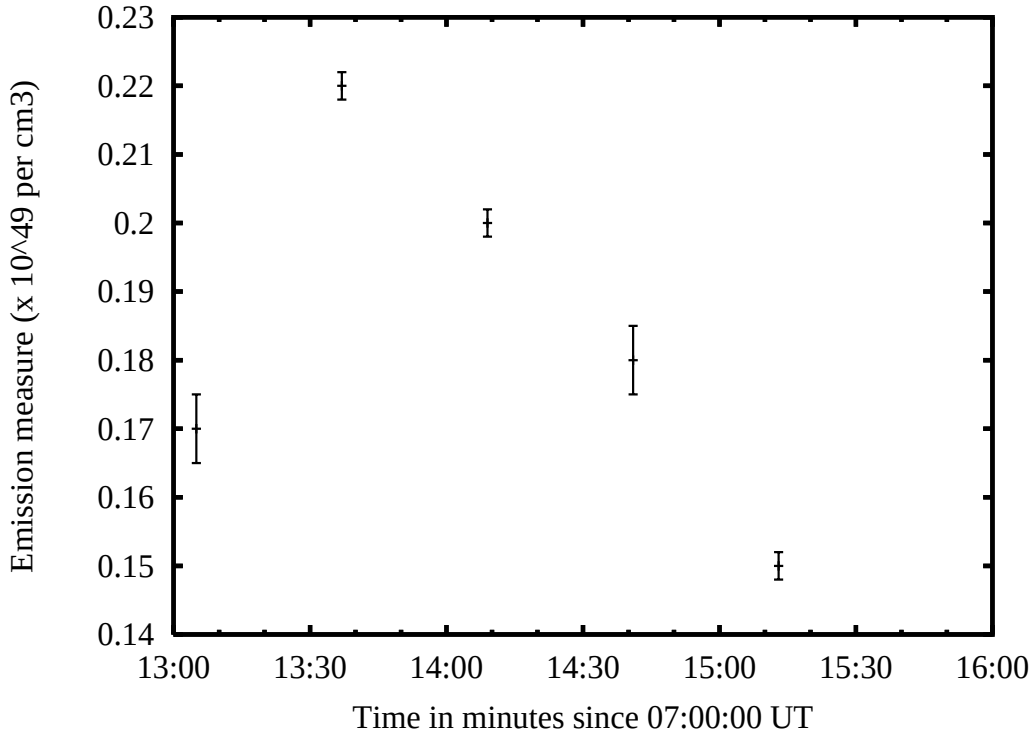

FIGURE 4.18: Solar spectral evolution corresponding to the five pixels analyzed

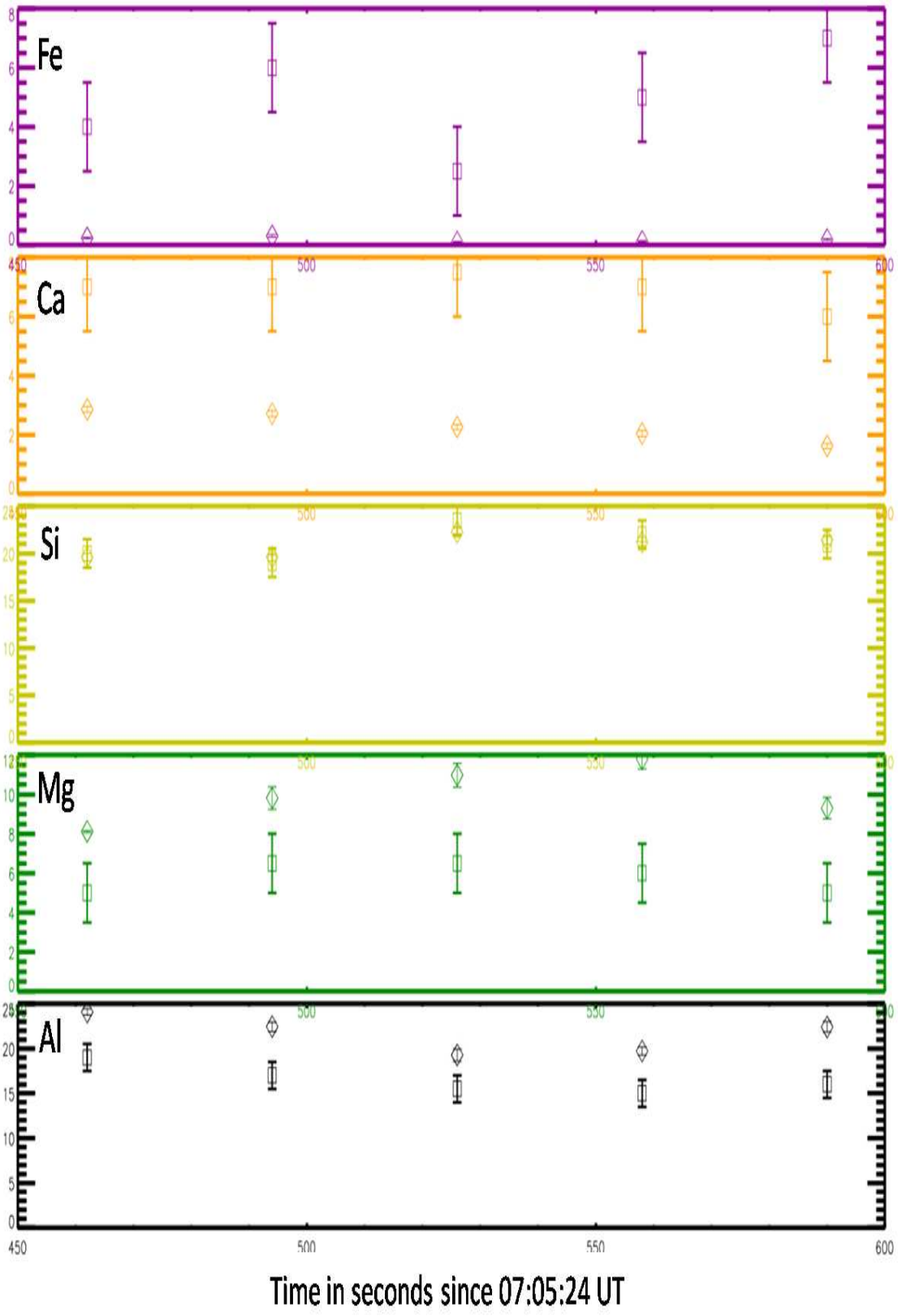

FIGURE 4.19: Variation in elemental wt% follows variation in flux ratio

4.7 Summary

In this chapter, we have described the methodology for the analysis of C1XS XRF data. The variation in background spectra under nominal conditions and during geotail passes was studied. It is found that during geotail passes, the background in C1XS increases significantly and the particles induce characteristic x-ray emission from the Al filter. We have analyzed lunar x-ray spectra measured by C1XS during a C3 flare while C1XS was in the geotail. The pre-flare spectra were studied to estimate contamination by the PIXE induced Al line and it is found that there is no measurable PIXE effect during the time of the flare.

X-ray line flux from the observed fluorescence of the major elements is determined through spectral analysis. The solar spectra obtained simultaneously with XSM is also modeled. The elemental abundance from the five major elements Mg, Al, Si, Ca and Fe for five 50 km x 50 km ground pixels has been derived from this analysis. C1XS has for the first time provided a direct estimate of elemental abundance from Ca through remote sensing. The chemistry of the sampled region and its geological context are discussed in the next chapter.

Chapter 5

Summary

We have for the first time simultaneously measured lunar x-ray fluorescence from the major elements Mg, Al, Si, Ca and Fe and estimated their abundance. The region mapped, lies between $\sim$ 32°S and 26°S latitude at $\sim$ 8.5 °W longitude in the highlands. There are no returned samples from this region of the Moon. The closest in composition are samples from the Apollo 16 landing site (9 °S and 15.5°E) which is considered to closely represent highlands. There are earlier measurements of this region with the Lunar Prospector (LP) gamma ray spectrometer at scales of 150 km, but except for iron, are indirect. Other major elements have been mapped indirectly based on known correlations from ground truths. In this chapter, we compare C1XS derived compositions to these data and bring out the possible reasons for the observed differences. We report on the unique composition that C1XS measures, which could be indicative of a lithology rarer in the lunar samples.

5.1 Lunar chemistry from C1XS: results from the C3 flare

The lunar crust is thought of have formed as a result of crystallization from a magma ocean during the early phase of lunar evolution. Though covered with a thick regolith of $\sim$ 5-10 m, the highlands are representative of the composition of the underlying crust. They cover more than 80% of the lunar surface and is dominated by the silicate mineral plagioclase feldspar ((Ca,Na,K) $Al_2Si_2O_8$). Plagioclase feldspar can have compositions anywhere inbetween the end members $CaAl_2Si_2O_8$ (anorthite) and $NaAlSi_3O_8$ (albite).

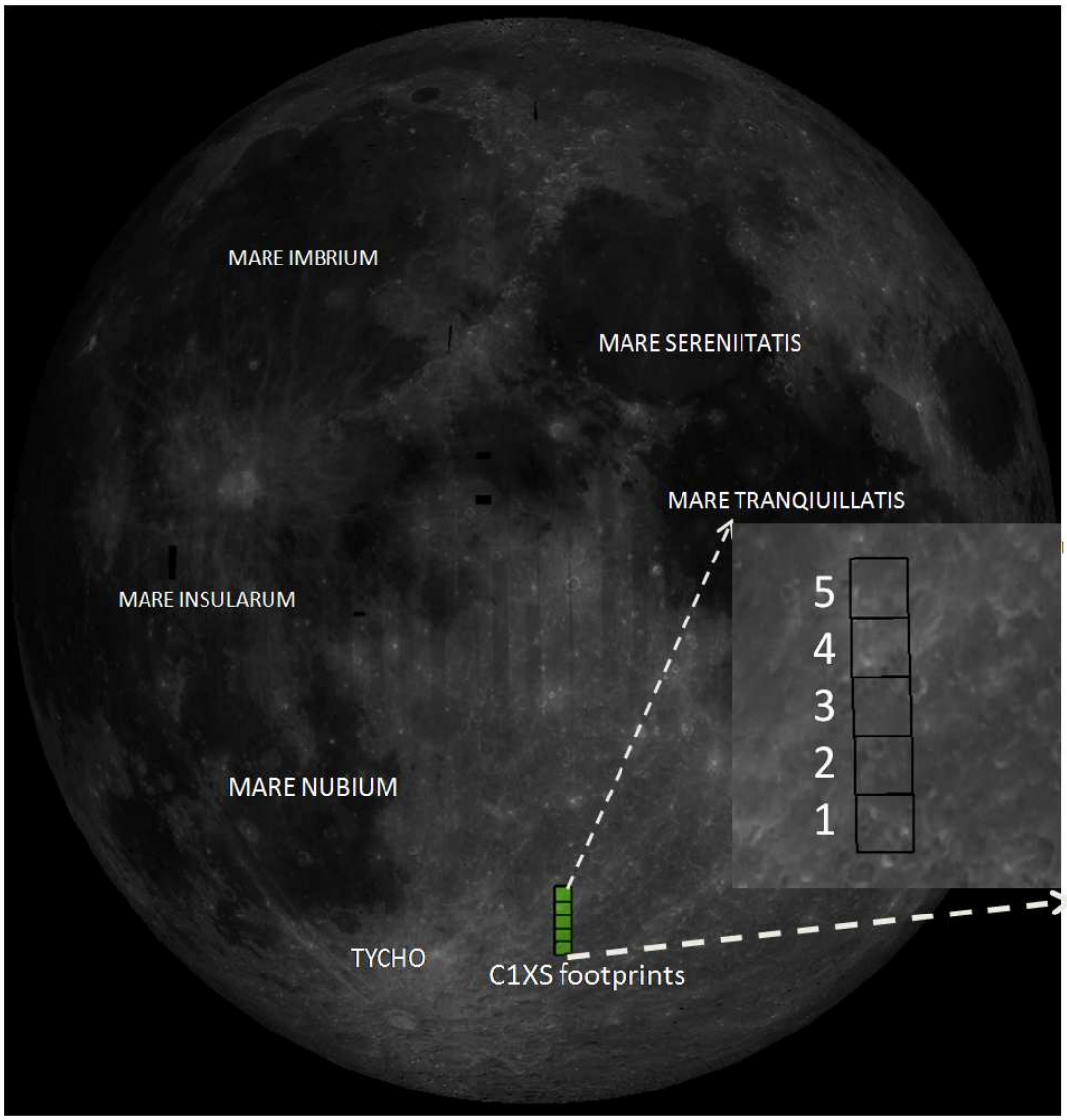

FIGURE 5.1: Geology of the region sampled during the 5 July 2009 C3 flare. C1XS footprints are marked in green (zoomed view in the inset)

Lunar samples show that most lunar plagioclase feldspars occur at intermediate compositions between anorthite and albite where the albite content is always much lesser than anorthite when compared to terrestrial feldpars.

There exist certain correlations between the major elements in the lunar rocks arising from the comparatively narrow range of minerals found there (less than a 100 variety of minerals as compared to more than 4000 on Earth). Al almost exclusively occurs in the mineral plagioclase whereas Mg and Fe in the mafic minerals pyroxene and olivine. Ca occurs both in plagioclase and clinopyroxene and Ti in ilmenite.

The region sampled during the C3 flare (5 July 2009) lies on the southern nearside highlands of the Moon ($\sim$ 32°S and 26°S at $\sim$ 8.5°W). C1XS FOV footprints during this time are plotted on the Clementine albedo map (750 nm) in Figure 5.1. The last two pixels (pixels 4 and 5 in Figure 5.1) cover the bright rays from the crater Tycho, one of the youngest (0.1 giga years) craters on the lunar surface. The ejecta has a higher albedo when compared to the surroundings suggesting compositional differences from the surrounding material. Global elemental maps from Lunar Prospector gamma ray data at scales of 150 km [Prettyman et al, 2006], show little compositional heterogeneity in this area. Very recently, thermal emission maps from the Diviner radiometer on LRO show that Tycho ejecta has a very distinct thermal reflectance with respect to the surrounding materials [Greenhagen, 2010].

Figure 5.2, Figure 5.3 and Figure 5.4 show the variation in abundance for Mg, Al, Si, Ca and Fe across the five pixels. Mg and Ca remains fairly uniform while Fe shows the largest variation (4- 8 %). The ejecta in Tycho's rays has a Mg# of 40.

C1XS elemental weight percentages provide a unique new data set for this geological region from where we do not have any lunar samples. The only other compositional information of the area is from the LP gamma ray data in which apart from Fe abundance all other elemental abundances are derived based on correlations that have been found to exist in lunar samples. On the other hand, C1XS data provide a direct estimation of the major element geochemistry.

Published literature on chemistry of lunar samples are almost always expressed as oxide wt percentages. Hence we have converted the derived elemental wt% to oxide wt% for comparison. The abundance in terms of oxide% (weight % in oxide) is given by

$$oxide\% = element\% \times \frac{mol.wt}{atomic.wt \times N_a} \tag{5.1}$$

where $element$% is the abundance in elemental wt%, mol.wt is molecular weight (calculated as the sum of the atomic weights weighted by the number of constituent atoms (N_a)). The oxide wt% derived from C1XS measurements are plotted along with compositions from 70 lunar samples (http://www.lpi.usra.edu/lunar/samples/) and Lunar Prospector gamma ray data (150 km ground pixels).

There are some general trends seen in lunar samples as shown in Figure 5.5. As Al increases (ie increase in plagioclase), Fe decreases because of the decrease in mafic minerals. Mg in the mare regions do not correlate with Al whereas a negative correlation

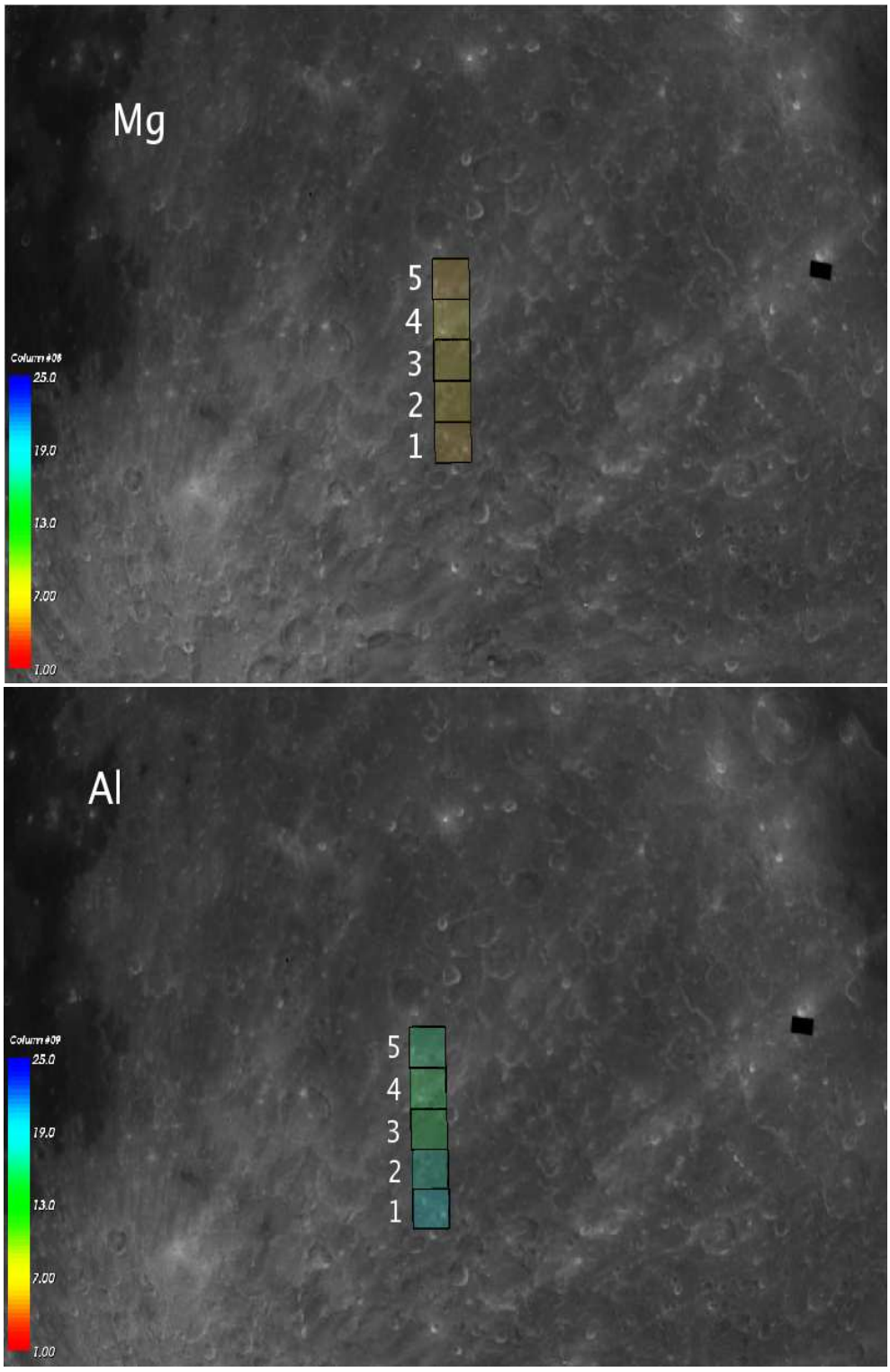

FIGURE 5.2: C1XS elemental maps (Mg,Al) overlayed on Clementine albedo map (750 nm)

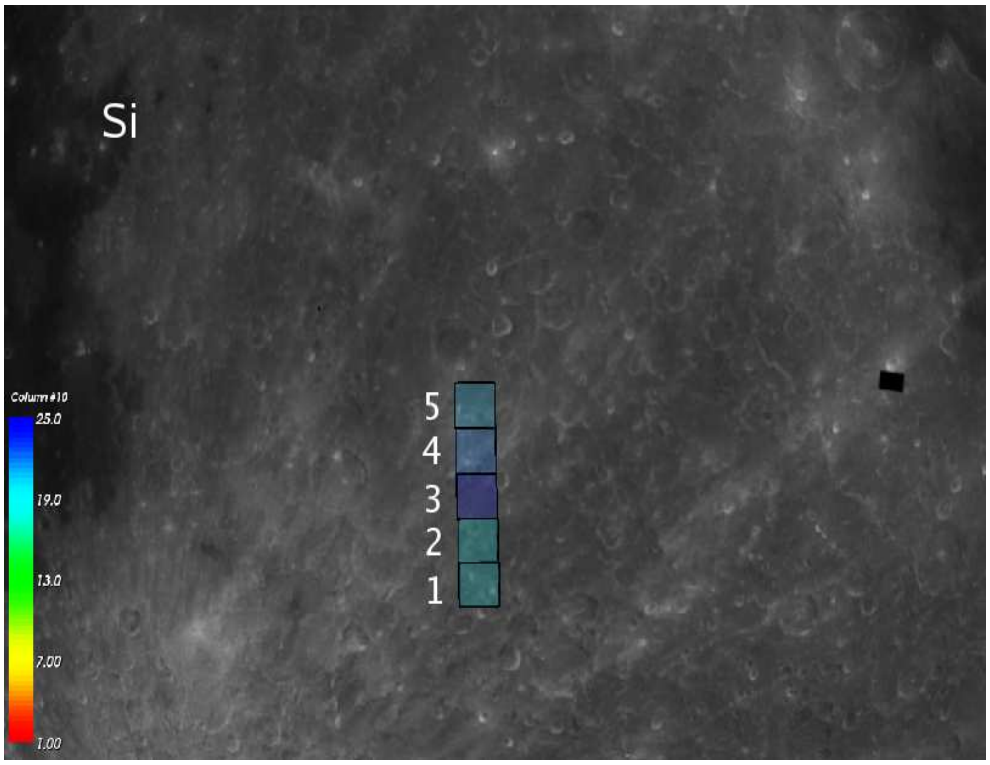

FIGURE 5.3: C1XS elemental map (Si) overlayed on Clementine albedo map (750 nm)

exists for the highlands. Ca similarly show a stronger positive correlation with Al in highlands.

The high Al abundance derived from C1XS data, indicates the composition of a highland terrain. Mg# in the five pixels are in the range 45 to 70 typical of ferroan anorthosites. But the compositions derived here (Figure 5.5) are distinctly different from the existing data on lunar compositions. Mg and Fe are higher than that typically found in high Al samples indicating a higher contribution from mafic minerals. The major deviation seem to be in the Al-Ca correlation (lower left plot in Figure 5.5) which exists because both elements occur in the mineral plagioclase. C1XS derived compositions have a higher Al/Ca ratio than in the available lunar highland samples (Apollo 16 samples and feldspathic meteorites).

We list out below the possible scenarios which can explain the observed C1XS composition as being deviant from that of known lunar highland samples. We begin by addressing potential limitations in the analysis.

- **Analysis**

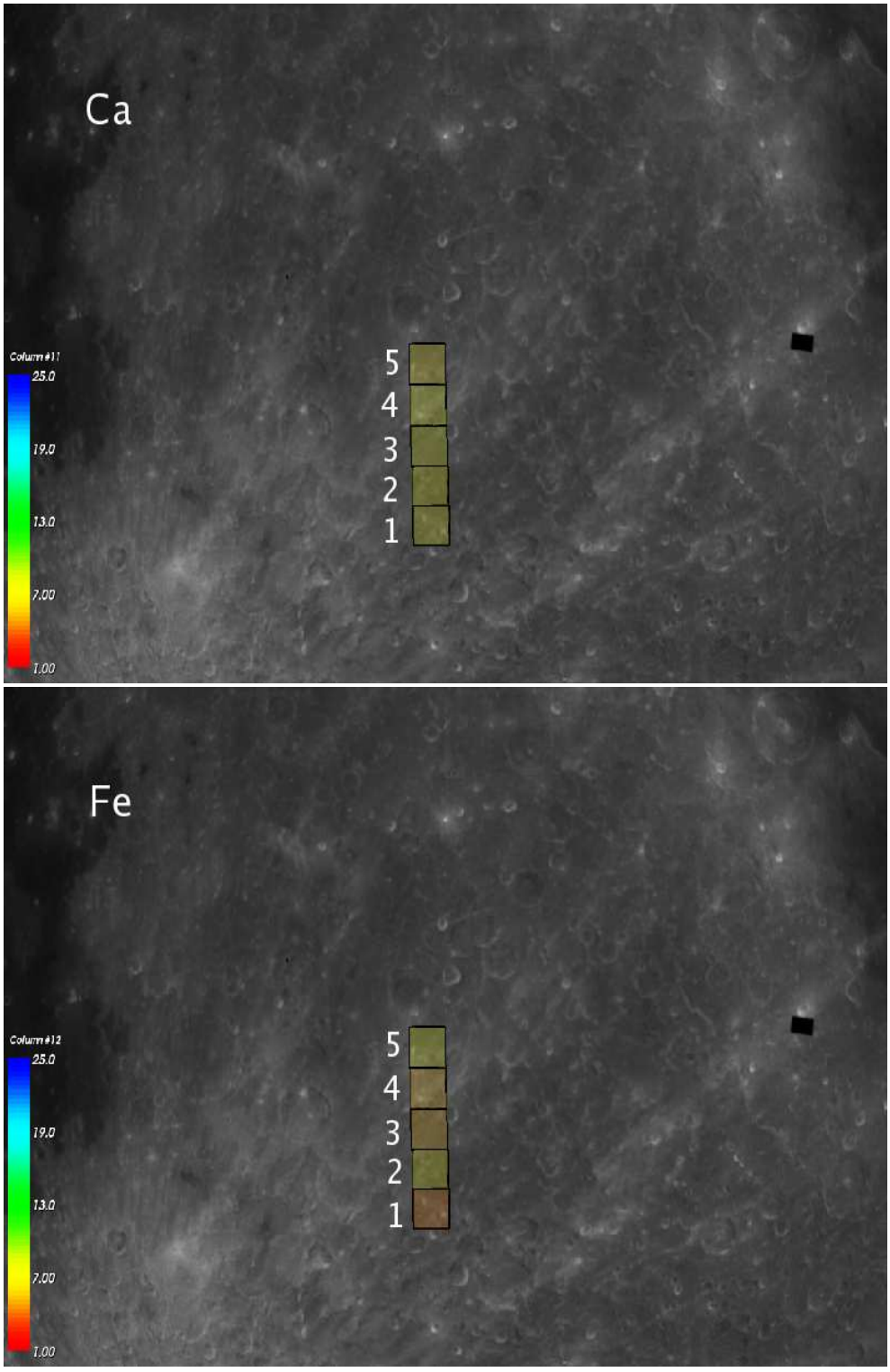

FIGURE 5.4: C1XS elemental maps (Ca, Fe) overlayed on Clementine albedo map (750 nm)

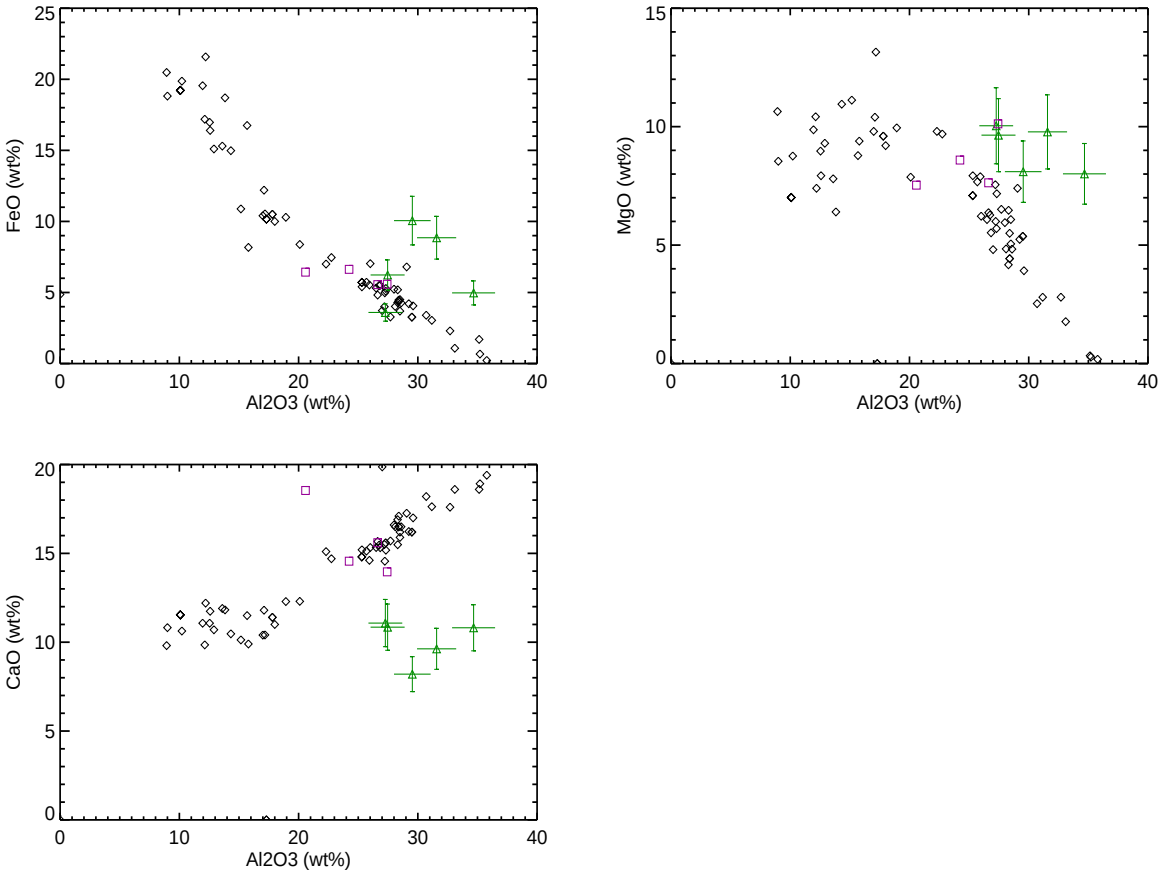

FIGURE 5.5: Compositions derived from C1XS plotted along with lunar samples (70 returned samples from the Apollo and Luna missions and lunar meteorites)

– **Limitations in the spectral re-distribution function and deviation in the detection efficiency:**

The spectral re-distribution function (SRF) of the SCDs has been sparsely sampled. To derive the full instrument response across the full energy range, it was interpolated for the 2.3 to 8 keV energy range. Three independent data sources were used to validate the SRF. The shape of the 2-10 keV continuum in ground calibration data, the four x-ray lines from the on-board Fe-55 sources and the observation of the cosmic x-ray background (CXB) emission (when the spacecraft was turned to observe Earth during solar eclipse) could be fitted well with the standard SRF models, showing that the interpolation has not produced any artifacts in the data.

Observation of the CXB emission and reproduction of the well measured spectrum provides another approach to validate the analysis set up (Appendix A).

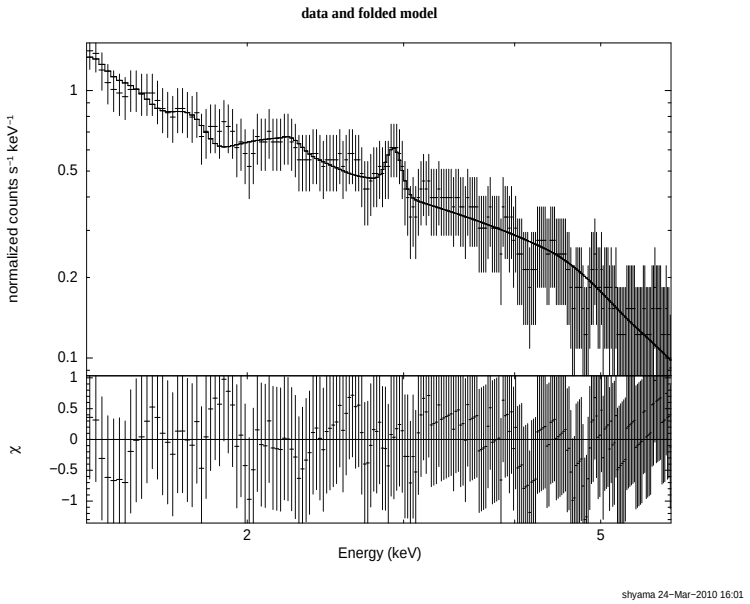

FIGURE 5.6: Cosmic x-ray background spectrum measured in C1XS fitted with a standard CXB model [Kushino, 2002] (hot diffuse gas emission and power law + Gaussian line at 2.9 keV arising from the fluorescence from Earth's atmosphere)

Difficulties with gain estimation for the CXB spectra, prevent us from adding the SCDs together for this observation. Therefore we used a single SCD spectrum added over time for the whole observation interval. This did not provide adequate statistics to further constrain uncertainties in the detection efficiency determined on ground. However, these measurements provided the necessary confidence that there are no detector artifacts which would enhance the measured Al line flux from the lunar surface. Even if the detection efficiency has small uncertainties, since the overall continuum fit is satisfactory, this deviation would only be in terms of scaling the detection efficiency up or down and hence should not affect flux ratios.

In the 1-2.3 keV range, the SCD response is assumed to be a Gaussian with the associated photopeak efficiency. The split events (expected to be small at low energies as the charge cloud radius is smaller and closer to the buried channel) that may exist at these energies have been modeled as part of the continuum in the spectral analysis and hence should not affect x-ray line flux determination.

– **Contribution from Particle Induced X-ray Emission (PIXE) from the Al filter on C1XS:**

Here we address if the observed Al line emission has significant contribution from background processes like PIXE. PIXE from the 4000 $\mathring{A}$ thick filter on C1XS (used to block optical light) has been observed during terminator crossings of geotail passes where particle flux are expected to be higher. We have shown in chapter 4 that PIXE produced Al line for this observation period is 20 minutes before the flare observations and hence would not affect the Al x-ray line flux from the Moon. However the whole day being a period of enhanced solar activity, it is possible that the charged particle environment is very dynamic during this observation period. Although there is no evidence for an enhanced particle flux from the radiation monitor data on Chandrayaan-1 (whose energy range is above 800 keV), we cannot conclude that such an enhancement has not occurred. However, the induced x-ray line flux from the Al filter in the pre-flare times is only 1.3% of the Al x-ray line flux from the Moon. A PIXE contribution of more than 15% (nearly 10 times stronger) to the Al line from the Moon would be required to lower the Al abundance to match typical highland composition.

- **Contribution from XRF from the Al filter:**
  Al photons can be induced by XRF from the filter, as the lunar XRF photons interact with it. However XRF line from the Al filter has not been observed in any of the RESIK calibration runs and hence should be at a negligible level.
- **Uncertainities in the conversion of x-ray line flux to elemental wt percentage:**
  We follow a standard approach based on the fundamental parameter algorithm to derive the elemental wt% and the code has been validated with laboratory samples with known compositions. Although, the effects of non homogenous mixtures and particle sizes on derived compositions have to been investigated here, earlier work suggest that the contribution from such effects while dealing with XRF line ratios cannot account for the large deviation in composition derived here.

So in conclusion, no convincing evidence exist to suggest the anomalous composition has arisen from improper analysis or limitations in the data processing.

- **The compositional differences are inherent to the Moon**
  - **Unusual compositions:**
    it is generally believed that lunar highlands are mainly composed of plagioclase feldspar with lower amounts of the mafic minerals. Plagioclase in lunar

samples have been found to have an anorthite content (defined as $\frac{Ca}{Ca+Na+K}$) as high as An_{98} with the average highlands estimated to be An_{95}. Lower anorthite content (as low as An_{70}) plagioclase grains (and hence higher albite) have been found in lunar samples but is much rarer. Remote sensing measurements through which global lunar mineralogy has been studied, cannot identify the anorthite content unless the plagioclase is of the purest form (greater than An_{98}). Pure crystalline anorthosite (PAN) rocks distributed globally have been revealed by the Kaguya multi band imager [Ohtake et al, 2009] recently but surprisingly has never been identified in lunar samples. These PAN rocks have been identified from a weak absorption feature at 1.3 μm arising from trace amounts of Fe^{2+} incorporated into the mineral structure. This feature disappears if the material is shocked (by impacts). The band center position changes depending on the An content allowing its quantification [Cheek, 2009]. The majority of plagioclase on the Moon otherwise is identified by a featureless IR spectrum which does not reveal the An content.

Recent observations by the Diviner radiometer on LRO which has three IR channels near 8 μm to measure the Christiansen feature (CF), has revealed regions where the band center shifts beyond their estimated range for the plagioclase, suggestive of the possible existence of higher amounts of albite (or sodic plagioclase) [Greenhagen, 2010]. Relevant to this context is also the fact that the lunar atmosphere is visible in sodium and potassium from Earth (neutral atoms sputtered from the surface) while only upper limits could be obtained for other much more abundant species [Potter and Morgan, 1988b]. The source of the neutral sodium atoms and rate of replenishment to the atmosphere is under debate but still this could be indicative of a higher sodium content in the lunar surface than we know today.

We suggest the possibility that C1XS could be revealing much larger regions of low An than previously thought of. This would explain the largest of the discrepancies that is shown in the Al and Ca correlation. Higher albite content would mean that Ca is being replaced by Na resulting in higher Al/Ca ratios than in lunar samples. The fact that PAN rocks identified remotely has never been found in lunar samples also opens up the possibility of yet to be discovered compositions.

– **Compositional layering of the regolith:**

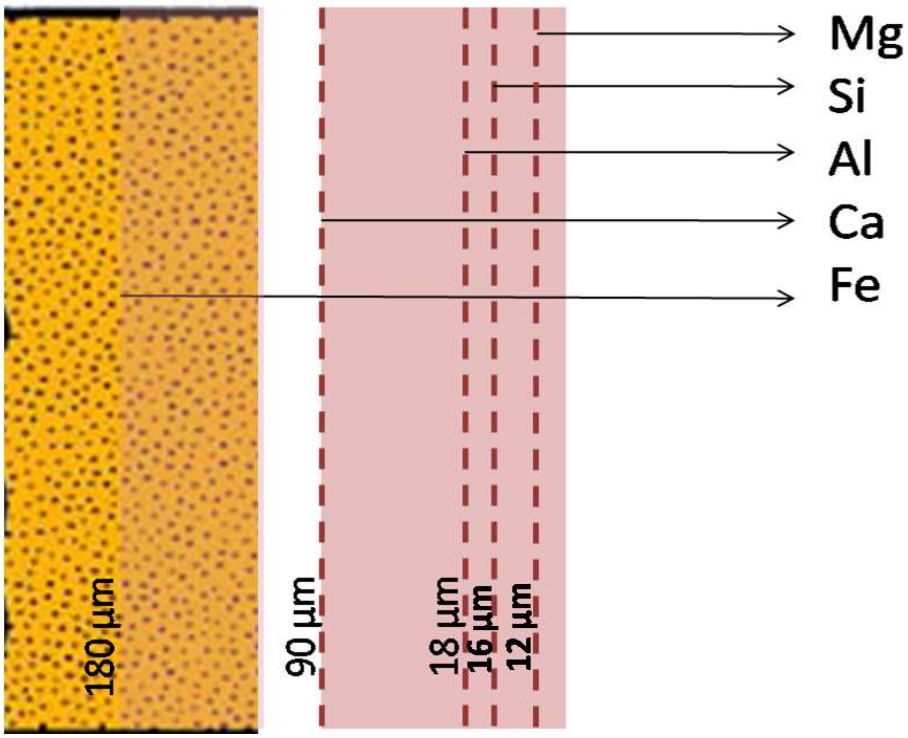

FIGURE 5.7: Depth from which the major elements are sampled (calculated for plagioclase).

The technique of x-ray remote sensing samples the very upper layer of the lunar regolith. The depth sampled depends upon the XRF photon energy (and hence the element), composition and density of the material. Assuming a density of 1.8 g/cm^3 and pure plagioclase feldspar, Figure 5.7 illustrates the different sampling depths from which the major elements in 1-10 keV are being sampled from. Al is being sampled from a region lesser than 20 μm whereas Ca is sampled up to a depth of 90 μm. If the plagioclase grains are restricted to the upper 20 μm and the Ca we measure is from more mafic materials deeper within, Ca could be lower with respect to Al. Another possibility is that the lower layer is more sodic than the upper 20 μm and hence results in the derived lower calcium.

– The less than 20 μm fraction of the lunar regolith has been found to have a composition richer in plagioclase, particularly Al and Na [Marvin, 1983], [Korotev, 1976], [Korotev, 1981]. If the bulk of the upper layer consists of this fine fraction, x-ray remote sensing would find a composition different from bulk composition of lunar samples. The lunar samples returned have always been collected as scoops and rock pieces. Even the core tubes intended

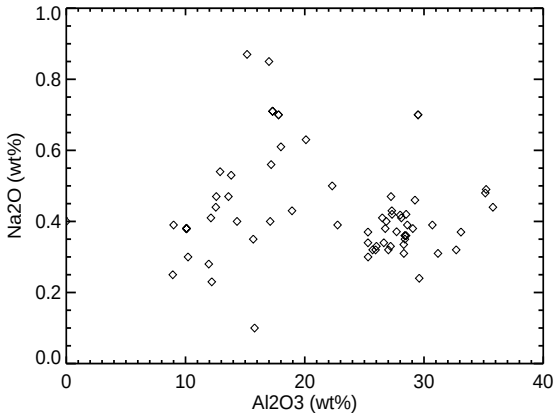

FIGURE 5.8: Lack of correlation between Al_2O_3 and Na_2O suggestive of a different carrier for Na

to study stratification in the regolith have been compressed while the core tubes were hammered in and retrieved. Thus we do not know the possible layering in the upper tens of micron of the regolith. Processes like levitation known to occur during geotail passes would kick up the fine particles from the regolith which could settle down as a veneer and thus have a composition different from the bulk. The sputtering of sodium atoms preferentially from the lunar surface [Stern, 1999] could also be because of this layering.

– **A different carrier for sodium:**
If sodium replaces calcium in plagioclase feldspar there would exist a correlation between Al and Na and anti-correlation between Ca and Na. However, no such correlations (Figure 5.8) have been observed in lunar samples suggesting an altogether different carrier (other than plagioclase) of sodium in the lunar regolith.

The above discussion lends strong support to the conclusion that the observed 'non-standard' Al/Ca ratio is not an 'experimental/analysis artifact ' and can be explained in many ways based on lunar surface composition and/or top layer stratigraphy.

5.2 A lunar XRF experiment for the future

C1XS has provided a new unique data set for major elemental geochemistry of the lunar surface. In addition, several of the minor elements have also been detected suggesting

TABLE 5.1: CLASS! specifications %

Parameter	CLASS!	C1XS	Remarks
Ground pixel	12 km x 12 km	25 km x 25 km	At the spacecraft altitude of 100 km
Field of view	14°x14 °	28°x28°	At the spacecraft altitude of 100 km
Detector	SCD (CCD-236)	SCD (CCD-54)	e2V technologies Ltd
Geometric area	4 cm^2	1 cm^2	Single unit with a single output signal
No:of units	24	24	
Total geometric area	96 cm^2	24 cm^2	
Energy range	0.8-10 keV	1-10 keV	0.8 keV for Na line detection
Minimum detectable flux	0.007	0.015	5 σ sensitivity for Si for 16 s integration

the potential to derive minor elemental abundances as well with an XRF experiment. However the low solar activity and limited sensitivity of C1XS has allowed only $\sim$ 4% coverage of the lunar surface. Given the uniqueness of an XRF experiment and complimentary nature to mineralogy, global chemical mapping of the Moon still remains an essential data set.

We propose an XRF experiment for the future in order to derive global major elemental chemistry of the lunar surface with an instrument with higher sensitivity. The experiment named CLASS! consists of 24 large area swept charge devices (CCD-236) recently developed by e2V technologies ltd, UK. Each of these detectors are of 4 cm^2 area, providing a total geometric area of 96 cm^2, which is four times that of C1XS. This would enable us to sample the lunar surface at a spatial resolution of $\sim$12 km from a 100 km altitude lunar orbit. The larger area also provides greater sensitivity enabling measurements even during quiet sun conditions thus enabling global coverage (ensures less dependency on an unpredictable active Sun). Table 5.1 lists the changes in CLASS! from C1XS.

The science objectives broadly remain the same as for C1XS, with the additional requirement to measure sodium abundance. Sodium line is not visible in gamma ray energies and thus can be measured only through x-ray remote sensing. Many of the ambiguities we described in the earlier section can be resolved if the sensitivity at 1 keV is adequate to measure XRF from Na. There are several lessons learned from C1XS of which we would improve upon the following areas:

- **Sensitivity of the instrument:**
  Sensitivity is a measure of the signal to noise ratio ($\frac{signal}{signal+noise}$). The minimum detectable flux F_{min} in terms of photons/cm^2/s given a background flux can be calculated as follows (converting the signal counts to photon flux as $\frac{photons}{\epsilon AT}$). If S is the detection level in terms of σ, ϵ(E) is the detection efficiency at energy E, B(E) is the background flux in photons/cm^2/s in the energy band δE, A is the geometric area of the detector and T is the exposure time.

$$F_{min} = \frac{S}{\epsilon}\sqrt{\frac{\epsilon B(E)}{AT\delta E}} \tag{5.2}$$

  At the energy of the silicon line, F_{min} for 5σ detection in C1XS, from the above equation can be calculated to be 0.008 photons/cm^2/s for an exposure time of 32 s. This corresponds to a solar activity at the level of $\sim$ A3 flare. Though this is better than any XRF experiments flown in the past, the solar activity being exceptionally low during C1XS observations, only less than 4% of the Moon has been covered (considering the coverage only during solar flare times where lunar XRF signals are detectable) as shown in Figure 5.9.

- **Calibration:**
  In order to achieve the primary objective of deriving elemental abundance, determination of absolute x-ray line flux is critical. The SRF has to be sampled in the whole range from 1 to 10 keV and absolute detection efficiency derived. The efficiency close to absorption edges need to be sampled finely as the 1 to 2 keV range is absolutely critical in XRF experiments with the three easily detectable elements in this energy range.

  On-board calibration with Fe-55 sources was meant only for energy-channel calibration and a measure of energy resolution. However gain is very sensitive to temperature and the Fe-55 spectra taken with the door closed, provided gain at temperatures lesser than -10°C which could not be used for lunar XRF measurements with the door open. The gain was thus always derived by calibrating with the observed XRF lines from the lunar surface.

  We propose to study the dependence of gain with temperature in more detail for CLASS!. It is also essential to measure the temperature of the SCDs accurately in order to make use of the temperature dependent gain derived on ground. Therefore we propose to have a temperature sensor each for every SCD as against two at each ends of the 4 (rows) x 6 (columns) C1XS-SCD array (one each at the middle

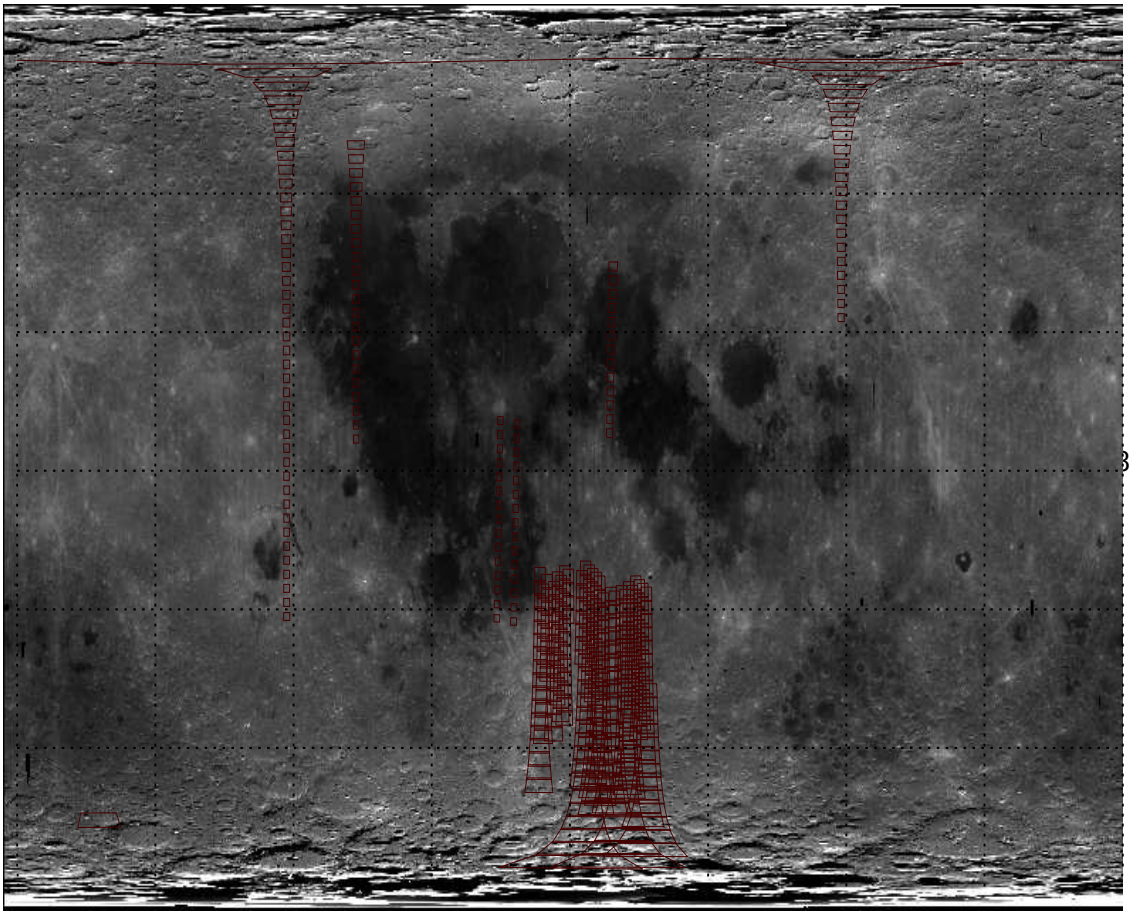

FIGURE 5.9: C1XS footprints during periods of solar activity where there are XRF measurements overlayed on Clementine albedo map (750 nm)

of the columns at either end; there was a temperature difference of $\sim 3^{\circ}$C between the two ends and hence we could not estimate individual SCD temperatures accurately).

- **X-ray line flux to elemental wt%:**
  Effects of particle size and inhomogeneous mixtures are two areas which have not been studied very well in the past and have to be investigated in order to interpret the data better.

- **Low energy threshold for the solar monitor down to 1 keV:**
  The low energy threshold of the solar monitor has to be down to 1 keV to estimate Na abundance as well. Ionised lines of Mg in the solar coronal spectrum near 1 keV has to be modeled accurately for deriving Na abundance. it is also essential to model the scattered solar x-rays which are pre-dominant at the weaker XRF line energy of 1 keV of sodium

5.3 Summary

In this chapter we have presented the compositions derived from C1XS data for a region on the central nearside highlands. The compositions derived are distinct from lunar compositions in the returned samples. We have discussed the various scenarios (indigenous to the Moon as well as in the analysis methods) that would lead to such a composition. We have also describe a future lunar XRF experiment with improved capabilities which would enable measurement of global lunar geochemistry.

In this thesis work we have described the detailed calibration of the XRF experiment C1XS on Chandrayaan-1, analyzed XRF spectra obtained during the brightest solar flare that occurred and presented the first results from C1XS. The work in this thesis brings out the necessity of lunar geochemistry and its feasibility through a well calibrated XRF experiment.

Appendix A

On-board calibration with the Cosmic X-ray Background

Chandrayaan-1 spacecraft was turned away from the Moon for observing the Earth during the total solar eclipse on 22 July 2009. We used this opportunity to measure the Cosmic X-ray Background (CXB) for C1XS calibration.

A.1 Observations and analysis

The spacecraft started the slew at 01.45:14 UT on 22 July 2009. During the two hour observations, C1XS went into the resting mode (see section 2.5) of operation because of increase in detector temperature. Thus C1XS measurements of the CXB span a period of only 25.6 minutes, from 02:48:02 UT to 03:13:44 UT. These spectra were added in time for all SCDs. The resultant spectra were analyzed for each SCD. A set of spectra before the slew began and when the SCDs were approximately at the same temperature as during the time of CXB observations, were added and used as background spectrum (separate for each SCD).

Cosmic X-ray background in the 1-10 keV band has been studied by several X-ray observatories in the past [Marshall et al, 1980], [Parmar et al, 1999], [Hasinger, 1983], [Moretti et al, 2009], [Gilli et al, 2007]. A large part of the cosmic x-ray background can be resolved into point sources. But since C1XS has a field of view with an opening angle of $\pm$14.3 degrees and no imaging capability, it measures all the sources in the field of view without being able to separate out the point source contribution. Thus the soft

X-ray spectrum observed in C1XS after removing the instrumental background consists of the following components.

$$\text{S(E)} = \text{Cosmic X-ray background } (S_{CXB}) + \text{point sources in the FOV} + \text{contribution from Earth's atmosphere.}$$

To determine any possible corrections to the C1XS detection efficiency derived on-ground, we should be able to model all the three components and then compare the CXB component to a standard model. Since C1XS cannot resolve the point sources, a model including the contribution from all sources in the field of view is required. Published literature on CXB spectrum with high resolution instruments in CHANDRA and XMM (where more than 60% of the CXB is resolved as point sources) were thus not appropriate for C1XS. We adopted the analytical model to the CXB spectrum suggested by Kushino et al [Kushino, 2002] based on ASCA (Advanced Satellite for Cosmology and Astrophysics) survey of the x-ray sky in 91 fields. The 2-10 keV spectrum is modelled as a power law with an index of 1.4±0.008 and the 0.7-2 keV with a model of the emission spectrum from a hot diffuse gas (MEKAL in XSPEC) including emission lines. The plasma temperature of the diffuse gas they determine is 0.39±0.03 keV and normalization 4.09 photons/cm^2/s/steradian.

$$\text{S}_{CXB} = \text{MEKAL model in XSPEC} + 9.66\ \text{E}^{-1.4}$$

where S_{CXB} is in units of photons/cm^2/s/steradian.

The contribution from Earth's disk for this wide FOV (Earth disk is 0.0092% of FOV) is negligible and hence has not been taken into account. However there is a faint line at 2.9 keV in the spectra which arises from x-ray fluorescence from argon in Earth's atmosphere. This has been used as an additional component in the model.

The H1 column density for a 14 degree diameter cone centered at the pointing (Galactic co-ordinates: 201.98° and 25.27°) during this observation was estimated from the web based tool (http://heasarc.gsfc.nasa.gov/). The NH value estimated is 6.4 x 10^{20} atoms/cm^3. The spectral fits thus used a model convolved with the XSPEC model wabs (gives the photoelectric absorption in a column of H atoms). All parameters except normalization of S_{CXB} were kept fixed for the spectral fit.

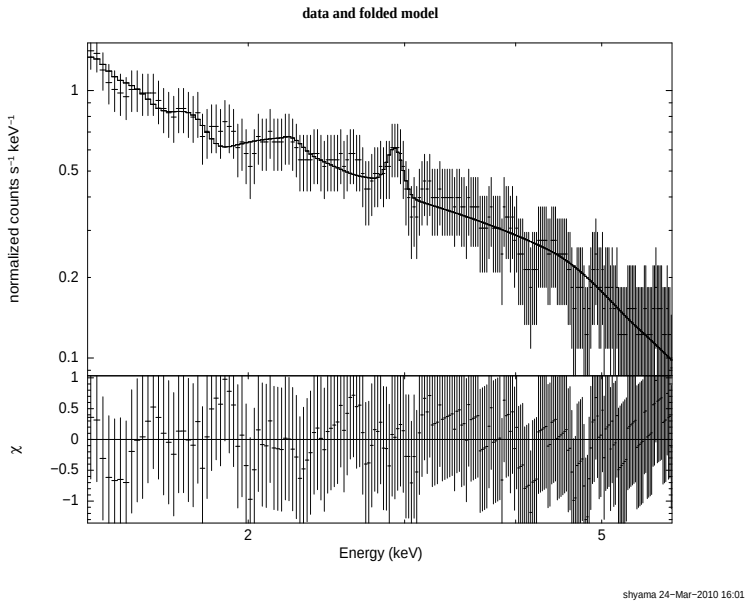

FIGURE A.1: Cosmic x-ray background spectrum measured in C1XS fitted with a standard CXB model [Kushino, 2002] (hot diffuse gas emission and power law + Gaussian line at 2.9 keV arising from the fluorescence from Earth's atmosphere)

C1XS solid angle can be calculated as follows and gives a value of 0.195 sr.

$$\Omega = \int_0^{2\pi} d\phi \int_0^{0.25} sin\theta d\theta \tag{A.1}$$

where θ varies from 0 to 14.3° (0.25 sr) and ϕ varies from 0 to 2π in cylindrical coordinates.

$$\mathrm{S}_{CXB} = (\mathrm{N}_1\ \mathrm{E}^{-1.4} + \text{Gaussian line at 2.9 keV}) \times \text{wabs} + \text{MEKAL}$$

We froze all the parameters except for the normalization of MEKAL and the power law. The background subtracted CXB spectrum has a count rate of only 0.3 counts/s/SCD. We could not add the spectra from all SCDs as the gain correction corresponding to the measured temperature did not work out well as for lunar spectra. We believe this is because the temperature distribution across the instrument would have been different as it turned away from the Moon. Figure A.1 shows the spectrum from one of the SCDs fitted with the above model. The normalization for the power law from the fit is 0.9 ± 0.1 which is close to 0.937 ± 0.007 given in Kushino et al. But because of the large errors derived from our analysis, we are unable to better the efficiency values any further than from ground calibration.

A.2 Conclusions

The CXB spectrum could be fit with a standard model and do not show any features in the residuals from which we conclude that the response matrix generated for C1XS is able to de-convolve the spectrum well. The strength of the CXB spectrum in 1-10 keV as given by the normalization of the model components, closely match the average value derived by Kushino et al from ASCA sky survey.

Bibliography

MJS Belton, JW Head, CM Pieters, R Greely, AS McEwen, G Neukum, KP Klaasen, CD Anger, MH Carr, CR Chapman, Lunar impact basins and crustal heterogenity, *Science* (1992), 255, 570.

S Nozette and the Clementine team, The Clementine Mission to the Moon - Scientific Overview, *Science* (1994), 266, 1835.

AB Binder, Lunar Prospector: Overview, *Science* (1998) 281, 1475.

BH Foing, GD Racca, A Marini, DJ Heather, D Koschny, M Grande, J Huovelin, HU Keller, A Nathues, JL Josset, A Malkki, W Schmidt, G Noci, R Birkl, L Iess, Z Sodnik, P McManamon, SMART-1 mission to the moon: Technology and science goals, *Advances in Space Research* (2001), 31, 2323.

H Mizutani, M Kato, S Sasaki, Y Iijima, K Tanaka, Y Takizawa, SELENE: The Moon-Orbiting Observatory Mission, *35th COSPAR Scientific Assembly* (2004), 35, 1916.

Huixian, Sun, Shuwu, Dai, Jianfeng, Yang, Ji, Wu, Jingshan, Jiang, Scientific objectives and payloads of Chang'E-1 lunar satellite, *Journal of Earth System Science* (2005), 114, 789.

N Bhandari, V Adimurthy, D Banerjee, N Srivastava, D Dhingra, Chandrayaan-1 Lunar Polar Orbiter: Science Goals And Payloads, *International Lunar Conference* (2004), 33.

JW Keller, R Vondrak, J Garvin, G Chin, Lunar Reconnaissance Orbiter: Observations for lunar exploration and science, *AGU* (2009),281, 1475.

UB Marvin, The discovery and initial characterization of Alan Hills 81005; the first lunar meteorite, *Geophysical Research Letters*, (1983), 10, 775.

JA Wood, Moon over Mauna Loa: A Review of Hypotheses of Formation of Earth's Moon, *Origin of the Moon* (1986), 125.

RM Canup, Dynamics of Lunar Formation, *Annu. Rev. Astro. Astrophys.*, (2004), 42, 441.

AB Binder, The Binary Fission Origin of the Moon, *Origin of the Moon* 0(1986), 499.

WK Hartmann and DR Davis, Satellite sized planetesimals and lunar origin , *Icarus* (1975), 24, 705.

AGW Cameron and WR Ward, The Origin of the Moon, *Lunar science* (1976), VII, 120.

SR Taylor, The Origin of the moon: Geochemical considerations, *Origin of the Moon* (1986), 125.

SC Solomon, MN Toksoz, Internal constitution and evolution of the Moon, *Phys. Earth. Planet. Inter* (1973), 7, 15.

GA Synder, LA Taylor, CR Neil, A chemical model for generating the sources of mare basalts: Combined equilibrium and fractional crystallization of the lunar magmasphere, *Geochim Cosmochim Acta* (1992), 56, 3809.

CK Shearer, PC Hess, MA Weiczorek, ME Pritchard, EM Parmentier, Thermal and magmatic evolution of the Moon, *Reviews in Mineralogy and Geochemistry* (2006), 60, 3809.

N Hasebe, N Yamashita, Y Karouji, S Kobayashi, M Hareyama, K Hayatsu, S Nemoto, K Iwabuchi, Y Takeda, H Nagaoka, K Tsukada, O Okudaira, S Sakurai, S Komatsu, E Shibamura, MN Kobayashi, M Ebihara, T Hihara, T Arai, T Sugihara, H Takeda, C dUston, O Gasnault, B Diez, O Forni, S Maurice, RC Reedy and K Kim, Overview of Elemental Distributions on the Moon Observed by SELENE GRS, *Geochim Cosmochim Acta* (2009), 56, 3809.

TH Prettyman, JJ Jagerty, RC Elphic, WC Feldman, DJ Lawrence, GW Mckinney, DT Vaniman, Elemental composition of the lunar surface: Analysis of gamma ray spectroscopy data from Lunar Prospector, *Journal of Geophysical Research* (2006), 111, 41.

MA Wieczorek, BL Joliff, Amir Khan, MR Pritchard, BP. Weiss, JG Williams, LL Hood, K Righter, CR Neal, CK Shearer, LS McCallum, S Tompkins, BR Hawke, C Peterson, JJ Gills, B Bussey, The Constitution and Structure of the Lunar Interior, *Reviews in Mineralogy and Geochemistry* (2006) 60, 221.

Nyquist and Shish, Lunar stratigraphy and sedimentology, *ELSEVIER* ,(1992).

Y Nakamura, Farside deep moonquakes and deep interior of the Moon, *Journal of Geophysical Research* (2005), 3, 2332.

P Lucey, RL Korotev, Understanding the lunar surface and space-Moon interactions, *Reviews in Mineralogy and Geochemistry* (2006), 60, 83.

H Hiesinger and JW Head, New Views of Lunar Geoscience: An introduction and overview, *Reviews in Mineralogy and Geochemistry* (2006), 60, 1.

DS Mckay, G Heiken, A Basu, G Blandford, S Simon, R Reedy, B French, JJ Papike, The lunar regolith, *The Lunar Source book: A User's Guide to the Moon, Cambridge Univ Press* (2006), 285.

BL Joliff, JJ Gills, LA Haskin, RL Korotev and MA Wieczorek, Major lunar crustal terranes: Surface expressions and crust-mantle origins, *Journal of Geophysical Research* (2000), 107, 4197.

JF Lindsay, Lunar stratigraphy and sedimentology, *ELSEVIER* 1976.

I Adler, The Analysis of Extraterrestrial Materials, *Chemical analysis*, (1986), 81.

McEwen and Robinson, Mapping of the Moon by Clementine, *Advances in Space Research* (1997), 81.

L Taylor, *Planetary Petrology and Geochemistry (The Lawrence A. Taylor 60th Birthday Volume)*, 1999.

S Kobayashi, M Kobayashi, M Hareyama, N Hasebe, E Shibamura, N Yamashita, Y Karouji, T Okada, C D'Uston, O Gasnault, O Forni, CR Reedy, KJ Kim, H Takeda, T Arai, T Sugihara, JM Dohm and Kaguya Gamma-Ray Spectrometer Team The Lowest Thorium Region on the Lunar Surface Imaged by Kaguya Gamma-Ray Spectrometer, *41st Lunar and Planetary Science Conference* (2010), abstract 1795.

AS Kiran Kumar and AR Chowdhury, Hyper-Spectral Imager in visible and near-infrared band for lunar compositional mapping, *Journal of Earth System Science* (2005), 114, 721.

Ohtake, Makiko, Matsunaga, Tsuneo, Haruyama, Junichi, Yokota, Yasuhiro, Morota, Tomokatsu, Honda, Chikatoshi, Ogawa, Yoshiko, Torii, Masaya, Miyamoto, Hideaki, Arai, Tomoko, Hirata, Naru, Iwasaki, Akira, Nakamura, Ryosuke, Hiroi, Takahiro, Sugihara, Takamitsu, Takeda, Hiroshi, Otake, Hisashi, Pieters, Carle M, Saiki, Kazuto,

Kitazato, Kohei, Abe, Masanao, Asada, Noriaki, Demura, Hirohide, Yamaguchi, Yasushi, Sasaki, Sho, Kodama, Shinsuke, Terazono, Junya, Shirao, Motomaro, Yamaji, Atsushi, Minami, Shigeyuki, Akiyama, Hiroaki, Josset, Jean-Luc, The global distribution of pure anorthosite on the Moon, *Nature* , (2009), 461, 236.

CM Pieters, JN Goswami, RN Clark, M Annadurai, J Boardman, B Buratti, JP. Combe, MD Dyar, R Green, JW Head, C Hibbitts, M Hicks, P Isaacson, R Klima, G Kramer, S Kumar, E Livo, S Lundeen, E Malaret, T McCord, J Mustard, J Nettles, N Petro, C Runyon, M Staid, J Sunshine, LA Taylor, S Tompkins, P Varanasi, Character and Spatial Distribution of OH/H2O on the Surface of the Moon Seen by M3 on Chandrayaan-1, *Science* (2009), 326,

RN Clark, Detection of Adsorbed Water and Hydroxyl on the Moon, *Science* (2009), 326, 933

Y Maruyama, K Ogawa, T Okada and M Kato, Particle size effects in x-ray fluorescence and its implication to planetary XRF spectroscopy, *38^{th} Lunar and Planetray Science Conference* (2007), abstract 1186.

AL Finkelshtein, N Brjansky, Estimating particle size effects in x-ray fluorescence spectrometry, *NIM B* (2009), 267, 2437.

SL Mandel'shtam, IP Tindo, GS Chermemukhen, LS Sorokin, AB Dimitriev, Lunar X-rays and the Cosmic X-ray Background measured by the Lunar Satellite, *Komisches. Isled* (1968), 119, 933.

SD Rasberry, KFJ Heinrich, Calibration for Interelement Effects in X-Ray Fluorescence, *Analytical chemistry* (1974), 46.

R Jenkins, *Quantitative X-ray Spectrometry*, (2000), 30.

I Adler, JI Trombka, P Lowman, R Schmadebeck, H Blodget, E Eller, L Yin, R Lamothe, G Osswald, Apollo 15 and 16 results of the integrated geochemical experiment, *The Moon* (1973), 7, 487.

TA Maxwell, PL Strain and F El Baz, Mare Crisium: Compositional inferences from low altitude X-ray fluorescence data, *Proc. Lunar. Sci. conf. 8th* (1977), 8, 933.

PE Clarke and BR Hawke, The lunar farside: The nature of the highlands of mare smythii, *Earth, Moon and Planets*, (1991), 53, 93.

M Grande, BJ Kellett, C Howe, CH Perry, B Swinyard , SK Dunkin, J Huovelin, L Alha, LC DUston, S Maurice, O Gasnault, S Couturier-Doux S Barabash, KH Joy, IA Crawford, DJ Lawrence, V Fernandes, I Casanova, M Wieczorek, N Thomas, U Mall, B Foing, D Hughes, H Alleyne, SS Russell, M Grady, R Lundin, D Baker, CD Murray, J Guest, A Christou, TheD-CIXS X-rayspectrometerontheSMART-1missiontothemoonfirst results, *PSS* 0(2007), 55, 494.

BM Swinyard, KH Joy, BJ Kellett, IA Crawford, M Grande, CJ Howe, O Gasnault, VA Fernandes, DJ Lawrence, SS Russell, MA Wieczorek, BH Foing and the SMART-1 team, *PSS* (2009), 57, 744.

T Okada, K Shirai, Y Yamamoto, T Arai, K Ogawa, H Shiraishi, M Iwasaki, T Kawamura, H Morito, M Kato, X-ray fluorescence experiments on the SELENE (KAGUYA) spacecraft, *39th Lunar and Planetary Science Conference* (2008), abstract 1966.

HMM Schmitt, SL Snowden, B Aschenbach, G Hasinger, LPfeffermann, P Predehl and J Trumper, The Soft X-ray image of the Moon, *Nature* 0(1991), 349, 583.

BJ Wargelin, M Markevitch, M Juda, V Kharchenko, R Edgar, A Dalgarno Chandra Observations of the Dark Moon and Geocoronal Solar Wind Charge Transfer *APJ* (2004), 607, 596.

JN Goswami and M Annadurai, Chandrayaan-1, *Current Science* (2009), 96, 486.

SL Lawson and BM Jakosky, Brightness temperatures of the lunar surface: The Clementine long wave IR Global data set, *30 th Lunar and Planetary Science Conference* (1999), abstract 1892.

IA Crawford, KH joy, BJ Kellett, M Grande, N Bhandari, AC Cook, L d'Uston, VA Fernandes, O gasnault, J Goswami, CJ Howe, J Huovelin, D Koschny, DJ Lawrence, BJ maddison, S maurice, CM Pieters, T Okada, DA Rothery, SS Russell, P Sreekumar, B Swinyard, M Wieczorek, M Wilding, The Scientific Rationale for the C1XS X-ray Spectrometer on India's Chandrayaan-1 Mission to the Moon, *Planetary and Space Science* (2009),57, 725.

BG Lowe, AD Holland, IB Hutchinson, DJ Burt, PJ Pool, Swept Charge Devices, *Nuclear Instrumentation and Methods in Physical Research A* (2001), 458, 568

DR Smith, J Gow, AD Holland, Proton irradiation of swept-charge devices for the Chandrayaan-1 X-ray Spectrometer (C1XS), *Nuclear Instrumentation and Methods in Physical Research A* (2007), 583, 270.

CJ Howe, D Drummond, R Edeson, B Maddison, D Parker, R Parker, A Shrivastava, J Spencer, BJ Kellett, M Grande, P Sreekumar, J Huovelin, D Smith, J Gow, S Narendranath, L dUstonc & O Gasnault, Chandrayaan1 X-ray Spectrometer (C1XS) Instrument Design & Technical Details *Planetary and Space Science* (2009), 57, 933.

G Lutz, Semiconductor Radiation Detectors, *Springer* (1999).

JR Janesick, Scientific Charge Coupled Devices, *SPIE* (2000).

J Lang, CM Brown, JE Magraw and J Payne The Laboratory Calibration of the Yohkoh Bragg Crystal Spectrometer *Internal doc RAL-93-035* (1993).

R Thornagel, R Klein and G. Ulm, The electron storage ring bessy ii as a primary source standard from the visible to the x-ray range *Metrologia* (2001), 38, 385.

M Richter, A Gottwald, F Scholze, R Thornagel, G Ulm, Calibration of space instrumentation with synchrotron radiation *Advances in Space Research* (2004), 37, 265.

MW Bautz, GY Prigozhin, MJ Pivovaroff, SE Jones, SE Kissel, GR Ricker, X-ray CCD response functions, front to back *Nuclear Instrumentation and Methods in Physical Research A* (1999), 436, 40.

F Scholze and M Procop, Modelling the response function of energy dispersive X-ray spectrometres with silicon detectors *X-ray spectrometry* (2006), 436,40.

A Sood, R Gardner, A new Monte Carlo assisted approach to detector response functions, *Nuclear Instrumentation and Methods in Physical Research B* (2004), 213, 100.

F Scholze and M Procop, Measurement of detection efficiency and response functions for an Si(Li) x-ray spectrometer in the range 0.1-5 keV, *X-ray spectrometry* (2001), 30, 69.

GW Philips and KW Marlow, Automatic analysis of gamma ray spectra from germainum detectors, *Nuclear Instruments and Methods* (1976), 137, 525.

A Owens, The X-ray energy response of silicon (A), *Nuclear Instrumentation and Methods in Physical Research A* (1996), 382, 503.

IM George, KA Arnaud, B Pence, *OGIP Calibration Memo CAL/GEN/92-002* (1998).

KA Arnaud, *Astronomical Data Analysis Software and Systems, ASP conf series* (1996), 101, 17.

M. Wallner, *Internal doc:C1-C1X-RAL-TN-0010* (2007).

R Thornagel, R Kelin and G Ulm, Detector calibration at the PTB radiometry laboratory at BESSY, *Metrologia* (2001), 38, 385.

M Al-Turany, JD Meyer, K Bethge, PIXE Analysis with the XR-100CR Si-PIN detector, *Nuclear Instrumentation and Methods in Physical Research A* (1999), 155, 137.

J. Gow, Radiation Damage Analysis of the Swept Charge Device for the C1XS Instrument, *PhD Thesis* (2009).

D. Smith, J. Gow, The effect of protons on the performance of swept-charge devices, *Nuclear Instrumentation and Methods in Physical Research A* (2009), 604, 177.

D Hall, A Holland, M Turner, Simulating and reproducing instrument background for x-ray CCD spectrometers in space, *Nuclear Instrumentation and Methods in Physical Research A* (2008), 86, 5682.

O Schneider, Interaction of the Moon with the Earth's Magnetosphere, *Space Science Reviews* (1967), 6, 655S.

A Prakash, Magnetospheric protons and electrons encountered by the Moon in the plasma sheet, *The Moon* (1975), 14, 75.

M Haphood, Modeling long term trends in lunar exposure to the Earth's plasma sheet, *Ann. Geophys* (2007), 25, 2037.

S Agostinelli, J Allison, K Arnako, J Apostolakes, H Aranyo, P Arce, M Asai, D Axen, S Bannerjee, G Basrand, Modelling long term trends in lunar exposure to the Earth's plasma sheet *Spectrochim. Acta* (2003), 506, 250.

NA Tsyganenko, SB Karlsson, S Kokubun, T Yamamoto, AJ Lazarus, KW Ogilvie, CT Russell, JA Slavin, Global configuration of the magnetotail current sheet as derived from Geotail, Wind, IMP 8 and ISEE 1/2 data *Journal of Geophysical Research* (1998), 103, 1827.

J Sherman, The theoretical derivation of x-ray intensities from mixtures, *Spectrochim. Acta* (1955), 7, 283.

Shirawai and Fujino, Theoretical calculation of X-ray fluorescence intensities in Fluorescent spectrochemical analysis, *Japanese Journal of Applied Physics* (1966), 5, 886.

R Jenkins, RW Gould and D Gedcke, Quantitative X-ray Spectrometry, *Marcel Dekker, Inc 2nd edition* (1995).

LR Nittler, RD Starr, L Lim, J Timothy, J Mccoy, Burbine, RC Reedy, J Trombka, P Gorenstein, SW Squyres, WV Boynton, TP Mcclanahan, JS Bhangoo, PE Clarke, ME Murphy and R Kellen, X-ray fluorescence measurements of the surface eelemental composition of asteroid 433 Eros, *Meteoritics & Planetary Science* (2001), 36, 1673.

LF Lim and LR Nittler, Elemental composition of 433 Eros: New calibration of the NEAR Shoemaker XRS data, *Icarus* (2009), 200, 129.

T Okada, K Shirai, Y Yamamoto, T Arai, K Ogawa, K Hosono, M Koto, X-ray fluorescence spectrometry of Asteroid Itokawa by Hayabusa, *Science* (2006), 312, 5778.

KP Dere, E Landi, HE Mason, BC Monsignori Fossi, and PR Young, CHIANTI - an atomic database for emission lines, *Astronomy and Astrophysics Supplement Series* (1997), 129, 149.

BL Joliff, Fragments of Quartz Monozodiorite and Felsite in Apollo 14 Soil particles, *21st Lunar and Planetary Science Conference* (1991), abstract 101.

HOA Meyer, Apollo 16: Core 60004- Preliminray study of $<$ 1 mm fines, *Lunar and Planetary Science Conference* (1974), 5, 907.

SI Demidova, MA Nazarov, CA Lorenz, G Kurat, F Brandstatter and T Ntaflos, Chemical Composition of the Lunar Meteorites and the Lunar Crust, *Petrologiya* (2007), 15, 416.

LC Cheek, CM Pieters, MD Dyar, KA Miliam, Revisiting plagioclase optical properties for lunar exploration, *40th Lunar and Planetary Science Conference*,(2009), abstract 1928.

AB Foreman, RL Korotev, BL Joliff and RA Zeigler, Petrography and geochemistry of Dhofar 733 - An unusually sodic, feldspathic lunar meteorite, *39th Lunar and Planetary Science Conference* (2008), abstract 1853.

MD Norman, Lunar anorthosites as targets for exploration, *LRO Science Targeting Meeting* (2009), 6012.

BT Greenhagen, PG Lucey, TD Glotch, JL Bandfield, Global distribution of lunar silicates from the Diviner lunar radiometer, *41st Lunar and Planetary Science Conference* (2010), abstract 2382.

A Kushino, Y Ishisaki, U Morita, NY Yamasaki, M Ishida, T Ohashi, Y Ueda, Study of the X-ray Background Spectrum and its Large-Scale Fluctuation with ASCA, *Publication of the Astronomical Society of Japan* (2002)

RL Korotev, Geochemistry of grain size fractions from Taurus Littrow valley floor, *Proceedings of Lunar and Planetary Science Conference* (1976), 7, 695.

RL Korotev, Compositional trends in Apollo 16 soils, *Proceedings of Lunar and Planetary Science Conference* (1981), 12, 577.

AE Potter, TH Morgan, Discovery of sodium and potassium vapor in the atmosphere of the Moon, *Science* (1988b), 241, 675.

SA Stern, The lunar atmosphere: history, status, current problems, and context, *Reviews of Geophysics* (1999), 37, 453.

FJ Marshall, GW Clark, SAS 3 Survey of the Soft X-ray Background, *Astrophysical Journal* (1980), 287, 633.

AN Parmar, M Guainazzi, T Oosterbroek, A Orr , F Favata, D. Lumb, A Malizia, The low-energy cosmic X-ray background spectrum observed by the BeppoSAX LECS, *Astronomy and Astrophysics* (1999), 345, 611.

G Hasinger, The X-ray Background, *ASPC* (1983), 51, 439.

R Gilli, A Comastri, G Hasinger, The synthesis of the cosmic X-ray background in the Chandra and XMM-Newton era, *Astronomy and Astrophysics* (2007), 463, 79.

A Moretti, C Pagani, G Cusumano, S Campana, M Perri, A Abbey, M Ajello, AP Beardmore, D Burrows, G Chincarini, O Godet, C Guidorzi, JE Hill, J Kennea, J Nousek, JP Osborne, G Tagliaferri, A new measurement of the cosmic X-ray background, *Astronomy and Astrophysics* (2009), 493, 501.

List of Publications

A.3 Referred publications

1. **S Narendranath**, PS Athiray, P Sreekumar, BJ Kellett, KH Joy, I. Crawford, L. Nittler, O. Gasnault, M Grande, Lalita S, S Subramaniam, M Sudhakar, U Unnikrishnan, Analysis of x-ray fluorescence observations by the Chandrayaan-1 X-ray Spectrometer (C1XS): Results from a lunar highland region, *to be submitted to JGR*.

2. **S Narendranath**, P Sreekumar, BJ Maddison, CJ Howe, BJ Kellett, M Wallner, C Erd, SZ Weider, Calibration of the C1XS instrument on Chandrayaan-1,*NIM A* , 10.1016/j.nima.2010.04.049, article in press.

3. **S. Narendranath** and P. Sreekumar, Lunar X-ray fluorescence: Sensitivity to solar spectrum, *Exploration Geology and Geoinformatics*, Macmillan publishers India Ltd, 2009.

4. IA Crawford, KH joy, BJ Kellett, M Grande, N Bhandari, AC Cook, L d'Uston, VA Fernandes, O gasnault, J Goswami, CJ Howe, J Huovelin, D Koschny, DJ Lawrence, BJ maddison, S maurice, **S Narendranath**, CM Pieters, T Okada, DA Rothery, SS Russell, P Sreekumar, B Swinyard, M Wieczorek, M Wilding, The Scientific Rationale for the C1XS X-ray Spectrometer on India's Chandrayaan-1 Mission to the Moon,*PSS*, 2009, 57, 725.

5. M Grande, BJ Maddison, CJ Howe, BJ Kellett, P Sreekumar, J Huovelin, IA Crawford, L d'Uston, D Smith, M Anand, N Bhandari, A Cook, C Erd, V Fernandes, B Foing, O Gasnault, JN Goswami, A Holland, KH Joy, D Koschny, DJ Lawrence, S maurice, **S Narendranath**, T Okada, CM Pieters, D Rothery, SS Russell, A Shrivastava, BM Swinyard, M Wieczorek, M Wilding, The C1XS X-ray Spectrometer on Chandrayaan-1, *PSS*, 2009, 57, 717.

6. CJ Howe, D Drummond, R Edeson, B Maddison, D Parker, R Parker, A Shrivastava, J Spencer, BJ Kellett, M Grande, P Sreekumar, J Huovelin, D Smith, J Gow, **S Narendranath**, L dUstonc & O Gasnault, Chandrayaan1 Xray Spectrometer (C1XS) Instrument Design & Technical Details, *PSS*, 2009, 57, 648.

7. L Alha, J Huovelin, K Nyga, H Andersson, E Esko, CJ Howe, BJ Kellett, **S Narendranath**, BJ Maddison, IA Crawford, M Grande, P Sreekumar, Ground calibration of the Chandrayaan-1 X-ray Solar Monitor (XSM), *NIM A*, 2009, 23, 648.

8. **Shyama Narendranath. KC**, MC Ramadevi, M Sudhakar, D Bhattacharya, P Sreekumar, S Seetha , SLX 1746-311 in outburst *Advances in Space Research*, 2006, 38, 2788.

9. S Seetha, MC Ramadevi, VC Babu, MR Sharma, NSR Murthy, BN Ashoka,**KC Shyama**, R Kulkarni, G Meena, P Sreekumar, The Scanning Sky Monitor (SSM) on ASTROSAT *Advances in Space Research*, 38, 2995.

A.4 Conference proceedings (only lead author papers are listed)

1. **S Narendranath**, P Sreekumar, BJ Kellett, KH Joy, CJ Howe, IA Crawford, M Grande, L Alha, BJ Maddison, J Huovelin, C Erd, PS Athiray ,SZ Weider and the C1XS team, Lunar chemistry from Chandrayaan-1: C1XS results from southern nearside highlands of the Moon, *41st Lunar and Planetary Science Conference*, 2010, abstract no:1882.

2. **Shyama Narendranath**, Subramaniam Athiray, Uma Unnikrishnan, P. Sreekumar and the C1XS team, Analysis of lunar x-ray data: line flux to elemental abundance from the C1XS experiment on Chandrayaan-1, *Proceedings of the ESA x-ray fluorescence working group*, 2009.

3. **Shyama Narendranath**, P Sreekumar, BJ Kellett, Mattias Wallner, Chris Howe, Brian Maddison, Christian Erd, Manuel Grande, Instrument response of the Chandrayaan-1 X-ray Spectrometer (C1XS), *39^{th} Lunar and Planetary Science Conference*, 2008, abstract no:1136.